

Design of a Graphite Based Thermal Energy Storage for Concentrated Solar Power Applications

Cedric De Luca

A Thesis

in

The Department

of

Building, Civil and Environmental Engineering

Presented in Partial Fulfillment of the Requirements  
for the Degree of Master of Applied Science (Building Engineering) at  
Concordia University,  
Montreal, Quebec, Canada

August 2017

©Cedric De Luca, 2017





## **Abstract**

Design of a Graphite Based Thermal Energy Storage for Residential Concentrated Solar Power  
Applications

This thesis presents the feasibility of a residential scale, low cost, high temperature, graphite based sensible thermal energy storage (TES) device and proposes a design for such a device. The intended use for the proposed design is as a component of a larger concentrated solar power (CSP) generation system. A scaled down model of the prototype was tested for performance and durability. Measurements of thermal properties, discharge power, charging and discharging efficiencies and resistance to degradation by oxidation and vibration were taken to quantify the performance and durability. Oxidation rates were measured at 700 °C with SiC and Al<sub>2</sub>O<sub>3</sub> based protective coatings as well as with inert gas blanketing using argon, CO<sub>2</sub> and evacuation. The graphite was also subjected to vibration at 1000 rpm to evaluate any damage caused by contact with a reciprocating heat engine. To quantify the performance, the relationship between temperature and thermal conductivity was determined as well as the variation of specific heat capacity with temperature. These were measured in the range of 50 °C to 400 °C. Solar irradiance heat flux on the heat storage was simulated on the test samples to determine the temperature variation throughout the charging period of one day. All tests were done on two grades of graphite that vary in density, porosity and microstructure. Results obtained from testing the device indicate an effective lifespan of 31 years before needing to be replaced and yields a charging efficiency of 40.2%. Based on these results, a detailed design is presented. Finally, based on the results, a more detailed design of the device is proposed.

## **Acknowledgements**

I would like to thank all those who have contributed to this work. Thanks to this thesis' supervisors, Dr. Maria Elektorowicz and Dr. Mohammed Zaheeruddin, for their continued support as well as to Mrs. Nadezda Zhukovskaya for her guidance. Thanks to Joe Hrib, Hong Guan and Luc Demers for allowing me to use their facilities and equipment and providing expert advice. Thanks to the MITACS program, NSERC Discovery Grants of my supervisors and to the Faculty of Engineering and Computer Science at Concordia University for financial support. Special thanks to the team at Innovative Solar Power for providing the motivation for this project. Thanks to my family and friends and to my beloved Chloé who have endured this ordeal with me and supported me throughout.

## Table of Contents

List of Figures.....	viii
List of Tables.....	xi
List of Symbols.....	xiii
Chapter 1: Introduction and Research Objectives .....	1
1.1 Problem Statement .....	1
1.2 Research Objectives .....	4
Chapter 2: Literature Review.....	5
2.1 Applications of Thermal Energy Storage.....	5
2.2 Sensible Heat Storage.....	6
2.3 Latent Heat Storage.....	12
2.3.1 Direct Impregnation .....	16
2.3.2 Microencapsulation.....	16
2.4 Thermochemical Heat Storage .....	17
2.4.1 Hydrogen Energy Storage.....	25
2.5 Hybrid Heat Storage.....	25
Chapter 3: Methodology.....	27
3.1 Performance .....	30
3.2 Durability .....	31
Chapter 4: Thermal Properties of Graphite .....	33

4.1	Thermal Conductivity .....	33
4.2	Thermal Diffusivity.....	39
Chapter 5: Oxidation of Graphite .....		43
5.1	Silicon Carbide Based Anti-oxidation Coating.....	43
5.1.1	Unprotected Graphite Oxidation.....	43
5.1.2	Single Coat of SiC Based Coating .....	45
5.1.3	Double Coat of SiC Based Coating .....	47
5.1.4	Heat of Combustion .....	51
5.2	Aluminum Oxide Based Anti-Oxidation Coating.....	55
5.2.1	Double Coat of Al <sub>2</sub> O <sub>3</sub> Based Coating .....	55
5.2.2	Prolonged Heat Exposure .....	58
5.3	Inert Gas Blanketing.....	61
Chapter 6: Charging and Discharging Performance.....		65
6.1	Discharge Power .....	69
6.2	Full Cycle Simulation and Efficiency .....	74
6.2.1	Efficiency .....	74
6.2.2	Full Cycle Simulation .....	79
Chapter 7: Resistance to Vibration .....		86
Chapter 8: Heat Storage Prototype Design.....		92
8.1	Mass of the Graphite Block.....	92

8.2	Insulation .....	94
8.2.1	Relationship Between Pressure and Thermal Conductivity of a Gas .....	94
8.2.2	Infrared Radiation Shielding.....	101
8.3	Receiver Design .....	111
Chapter 9:	Results and Discussion .....	117
9.1	Durability .....	117
9.2	Performance .....	118
Chapter 10:	Conclusion and Recommendations.....	120
10.1	Conclusion.....	120
10.2	Recommendations to Overcome the Limitations.....	121
10.3	Future Research Work.....	122
10.4	Contributions.....	123
References.....		124
Appendix A:	Matlab program for radiation shield simulation.....	132
Appendix B:	Prototype Drawings.....	134

## List of Figures

Figure 1.1: Total global electricity production by energy source (International Energy Agency, 2017).....	2
Figure 1.2: Concentrated Solar Power (CSP) System .....	3
Figure 2.1: Schematic flow diagram of a parabolic trough power plant with 2-tank molten salt storage (Herrmann et al., 2004) .....	9
Figure 2.2: General Concept of thermochemical CaO/Ca(OH) <sub>2</sub> TES (Criado et al., 2014) .....	21
Figure 2.3: Discharging Process Scheme of CaO/Ca(OH) <sub>2</sub> TES (Criado et al., 2014).....	21
Figure 2.4: Charging Process Scheme of CaO/Ca(OH) <sub>2</sub> TES (Criado et al., 2014) .....	22
Figure 3.1: Work Flow Chart.....	28
Figure 3.2: Factors affecting TES quality.....	32
Figure 4.1: Reaching steady state temperatures for measuring thermal conductivity .....	37
Figure 4.2: Thermal conductivity of graphite as a function of temperature .....	37
Figure 4.3: Thermal diffusivity of graphite as a function of temperature .....	41
Figure 4.4: Specific heat capacity of graphite as a function of temperature.....	42
Figure 5.1: Sample 1 oxidation rate of lower grade graphite with no coating at several temperatures .....	44
Figure 5.2: Sample 2 oxidation rate of higher grade graphite with no coating at several temperatures .....	45
Figure 5.3: Oxidation rate with Aremco anti-oxidation coating at 700 <sup>0</sup> C (pre-oxidized, 1 coat) .....	46
Figure 5.4: Oxidation rate with Aremco anti-oxidation coating at 700 <sup>0</sup> C (unoxidized samples, 2 coats).....	47

Figure 5.5: Oxidation rate over prolonged heat exposure with 2 coats of Aremco coating at 700 <sup>0</sup> C.....	50
Figure 5.6: Oxidation rates of graphite with two coats of Aepco aluminum oxide based anti-oxidation coating at 700 <sup>0</sup> C.....	56
Figure 5.7: Comparison of the effectiveness of two coats of Aremco (SiC) to two coats of Aepco (Al <sub>2</sub> O <sub>3</sub> ) anti-oxidation coatings at 700 <sup>0</sup> C.....	57
Figure 5.8: Graphite (high grade) oxidation rate at 700 <sup>0</sup> C with 1 coat of Aepco (Al <sub>2</sub> O <sub>3</sub> ) anti-oxidation coating with heating and cooling cycles.....	59
Figure 5.9: Schematic of inert gas blanketing oxidation test.....	62
Figure 6.1: Multipurpose test rig setup.....	68
Figure 6.2: Discharging power per unit mass of a graphite based sensible TES (high grade graphite).....	72
Figure 6.3: Discharging power per unit mass of a graphite based sensible TES (low grade graphite).....	72
Figure 6.4: Charge and discharge energy and power (high grade).....	76
Figure 6.5: Charge and discharge energy and power (low grade).....	77
Figure 6.6: Temperature of TES during the daytime charging period (high grade graphite).....	83
Figure 7.1: Crystal structure of graphite showing primary bonds (black lines) and weak secondary bonds (red lines).....	86
Figure 7.2: Vibration test rig setup.....	88
Figure 7.3: Vibration test rig setup.....	89
Figure 8.1: Non-equilibrium transport of quantity a (energy or momentum or mass) carried by gas molecules.....	96

Figure 8.2: Radiation shielding in TES casing .....	103
Figure 8.3: Resistive network model of heat transfer through the radiation shielding.....	104
Figure 8.4: Heat loss rate through radiation shielding.....	108
Figure 8.5: Total heat loss and graphite temperature during a 24-hour cooling period.....	108
Figure 8.6: Fraction of heat rate between two large parallel surfaces with multiple layers of radiation shields between them.....	110
Figure 8.7: Mid-plane section view of the heat storage.....	112
Figure 8.8: Solar Radiation Spectrum (Wikimedia Commons, n.d.).....	113
Figure 8.9: Blackbody spectral intensity .....	114

## List of Tables

Table 1.1: Design Constraints.....	4
Table 2.1: Sensible heat storage materials (Kalaiselvam, 2014) .....	8
Table 2.2: Phase Change Materials (IEA-ETSAP and IRENA, 2013).....	13
Table 2.3: Potential thermochemical TES materials (Renewable Energy and Climate Change Program, SAIC Canada, 2013) .....	18
Table 2.4: Promising thermochemical heat storage reactions (Yan et al., 2015) .....	24
Table 5.1: Oxidation rates and lifespan for various conditions .....	48
Table 5.2: Expected oxidation rates for the actual storage block (constant rate) .....	49
Table 5.3: Expected lifespan of actual storage block (constant rate) .....	49
Table 5.4: Expected lifespan of the actual storage block (variable rate) .....	51
Table 5.5: Lifespan and effective lifespan of the actual heat storage block of graphite.....	58
Table 5.6: Effective lifespans of the test sample and of the actual storage block using inert gas blanketing.....	63
Table 6.1: Variable input power provided to TES model to simulate solar flux .....	81
Table 6.2: Graphite based TES capacity.....	85
Table 7.1: Degradation of high grade graphite due to vibration at 1000 rpm .....	89
Table 7.2: Degradation of low grade graphite due to vibration at 1000 rpm.....	90

## List of Symbols

$\bar{C}$ : average molecular velocity (m/s)

$\dot{Q}$ : heat rate (W)

$\dot{g}$ : heat generation in material (W/m<sup>3</sup>)

$\dot{m}$ : mass flow rate (kg/s)

$a$ : arbitrary quantity

$A$ : area (m<sup>2</sup>), absorbed radiation intensity (W/m<sup>2</sup>)

$A_c$ : contact area between heat storage and engine heat exchanger (m<sup>2</sup>)

$A_i$ : contact area between HTF and engine heat exchanger (m<sup>2</sup>)

$b$ : lattice parameter (m)

$B$ : spring constant (N/m)

$Bi$ : Biot number

$C$ : heat capacity (J/K)

$c$ : specific heat capacity (J/kgK), speed of light (m/s)

$d$ : sample thickness (m), molecular diameter (m)

$E$ : Young's modulus (Pa)

$E_b$ : blackbody radiation intensity (W/m<sup>2</sup>)

$f$ : porosity

$F$ : view factor

$G$ : incident radiation power (W/m<sup>2</sup>)

$h$ : convective heat transfer coefficient (W/m<sup>2</sup>K), Planck's constant (m<sup>2</sup>kg/s)

HTF: Heat transfer fluid

$J$ : radiosity (W/m<sup>2</sup>)

$K$ : Boltzmann constant (m<sup>2</sup>kg/s<sup>2</sup>K)

$k$ : thermal conductivity (W/mK)

$k_0$ : reference thermal conductivity of non-porous pure crystal (W/mK)

$k_e$ : thermal conductivity of engine heat exchanger material (W/mK)

$k_g$ : thermal conductivity of heat storage material (W/mK)

$Kn$ : Knudsen number

$L$ : length (m)

$L_c$ : characteristic length of system (m)

$m$ : mass (kg)

$n$ : number density of molecules (molecules/m<sup>3</sup>)

$N$ : number of molecules

$N_c$ : number of vacant atomic sites in lattice

$N_p$ : number of atoms in a perfect crystal

$Nu$ : Nusselt number

$P$ : pressure (Pa)

PCM: Phase change material

$Pr$ : Prandtl number

$q$ : heat flux (W/m<sup>2</sup>)

$Q_c$ : charge energy (J)

$Q_d$ : discharge energy (J)

$Q_{sol}$ : solar radiation energy (J)

$R$ : electrical resistance ( $\Omega$ ), radiation resistance (m<sup>-2</sup>), reflected radiation intensity (W/m<sup>2</sup>)

$r$ : radius (m)

$Re$ : Reynolds number

$S$ : rate of molecules crossing boundary (molecules/second)

$T$ : temperature (<sup>0</sup>C) or (K), transmitted radiation intensity (W/m<sup>2</sup>)

$t$ : time (s)

TES: Thermal energy storage

$u$ : specific internal energy (J/kg)

$v$ : velocity (m/s)

$V$ : voltage (v), volume (m<sup>3</sup>)

$x$ : length (m)

$\Delta h^0$ : specific enthalpy (kJ/mol)

$IT$ : dimensionless number for thermal performance model

$\alpha$ : thermal diffusivity (m<sup>2</sup>/s)

$\beta$ : constant of proportionality between  $S$  and  $n\bar{C}$  (m<sup>2</sup>)

$\varepsilon$ : emissivity

$\eta$ : overall efficiency

$\eta_c$ : charge efficiency

$\eta_d$ : discharge efficiency

$\lambda$ : mean free path (m), wavelength (m)

$\mu$ : dynamic viscosity (Ns/m<sup>2</sup>)

$\rho$ : density (kg/m<sup>3</sup>)

$\sigma$ : Stefan-Boltzmann constant (W/m<sup>2</sup>K<sup>4</sup>)

$\omega_n$ : natural frequency (rad/s)

$\xi$ : number of degrees of freedom of molecule

$\Lambda$ : flux per unit area of quantity

## **Chapter 1: Introduction and Research Objectives**

### **1.1 Problem Statement**

According to the World Energy Outlook, 16% of the global population lives in areas where electric power grids are unavailable (World Energy Outlook, 2016). Africa, with the lowest electrification rate, has 55% of its population living without electricity. Typically, these unelectrified regions are in poor countries located in mid-latitudes where solar irradiance is high. Whatever the reason for the lack of an electric grid, homes located in such regions stand to benefit from a low-cost device that can generate electricity locally from a renewable source such as solar. With a small-scale device such as this, electricity could be generated in the most remote locations.

Small scale concentrated solar power systems such as parabolic trough and dish engine systems are already available in many forms and nearly all of them convert solar radiation directly to an engine, wherein lies the problem with these systems; they only generate electricity when the sun is shining leaving those dependent on them without electricity at night. Batteries can store the charge for later use but these batteries come at a high cost, both financially and environmentally. Thus, an inexpensive, environmentally friendly means of storing energy is an essential aspect for regions with no electric grid.

In addition to allowing unelectrified regions produce electricity locally, advances in the field of energy storage will encourage the global adoption of renewable sources of energy. The total global electricity production from combustible fuels increased by 0.8% while production from

renewable sources, excluding hydro, increased by 0.5% as shown in figure 1.1 (International Energy Agency, 2017). Ideally, production from renewable sources should be greater but combustible fuels are still the dominant source. The reasons for this tendency are numerous but one of the strongest arguments for dependence on combustible fuels is their reliability. They can be consumed at any rate required by the instantaneous demand for electricity while renewable sources are intermittent in their availability. However, if energy storage technologies are developed, combustible fuels will lose their advantage over renewables. With the capacity to store renewable energy, it becomes available to meet the demand. Energy storage technologies are therefore an essential avenue of research if the dependence on combustible fuels is to be significantly reduced.

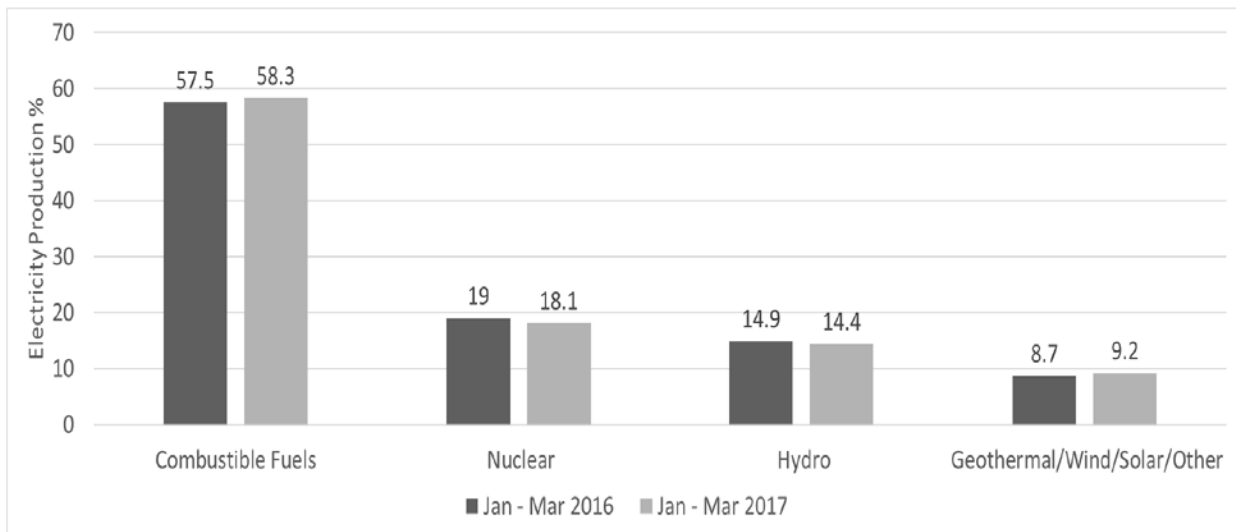


**Figure 1.1: Total global electricity production by energy source (International Energy Agency, 2017)**

The intent of this research is to develop and test an inexpensive, high temperature heat storage for use in conjunction with a solar concentrator for electricity generation on a small scale. The

heat storage material must also be abundant with minimal impact on the environment. The functioning of the system is as follows. Incident solar radiation is reflected to a focal point by an array of spherical mirrors resulting in a very high heat flux at the focal point. The heat storage, located at the focal point absorbs this heat and stores it until it is transferred by conduction as input energy to a Stirling engine. This engine drives a generator which produces electricity. Figure 1.2 summarizes the components of the system and the energy conversions. The solar radiation is thus ultimately converted to electrical power.

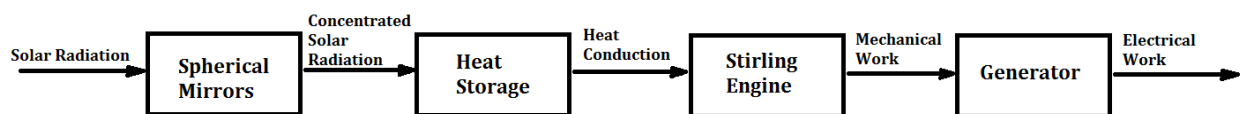


**Figure 1.2: Concentrated Solar Power (CSP) System**

The focus of this research is the heat storage component and its input and output energy. The heat is stored as sensible heat in a block of graphite. Graphite was chosen for its high thermal conductivity, high heat capacity and low cost. The storage is simply an insulated block of graphite with a receptacle for the engine's heat exchanger. While the sun is shining, the graphite absorbs the concentrated radiation and its temperature increases. Then, when the sun has set, the engine's heat exchanger removes heat from the graphite and lowers its temperature. The engine stalls if the temperature of the storage is below 300 °C and optical simulations suggest that the maximum attainable temperature is 700 °C. Therefore, the operating temperature range for the storage is from 300 °C to 700 °C.

## 1.2 Research Objectives

The goal is to develop and test a heat storage that can effectively absorb solar radiation at high temperatures and that can discharge the heat to the engine in a controlled manner. The scale of the whole system is such that it can store 25 kWh of heat per day. The overall quality of the heat storage depends on two main characteristics; its performance and its durability in adverse conditions.

Prior to designing and testing the heat storage, some preliminary objectives for the performance and durability parameters should be set to be used as a guide for design choices. Table 1.1 are the objectives that are deemed reasonable such that this type of solar power system could potentially compete with photovoltaic systems.

**Table 1.1: Design Constraints**

Parameter	Objective
Temperature range	300 <sup>0</sup> C – 700 <sup>0</sup> C
Heat Capacity for given temperature range	25kWh
Charging Efficiency	90%
Charging-Discharging Efficiency over 18 hours	95%
Discharge heat rate	control
Oxidation resistance	10 year effective lifespan
Seal (Temperature/Pressure Resistance)	no leak
Vibration Resistance	<0.013mm/year of wear, no cracking
Cost	<500\$ CAD

A more detailed definition of these parameters and the mechanism that influences them can be found in subsequent chapters.

## **Chapter 2: Literature Review**

### **2.1 Applications of Thermal Energy Storage**

The intent of this work is to summarize the present collective knowledge of heat storage technologies, in order to identify unexplored avenues of research and to avoid duplication of research efforts. Having read the reports, journals, articles and books of other researchers on a similar topic, the direction in which further research should be focused becomes clear. The questions that remain unanswered are to be addressed.

Heat storage, also known as thermal energy storage (TES), is a broad subject with an abundance of literature on the topic but there are many applications for heat storage and each application has its own set of obstacles. Different heat storage technologies seem to belong to one of two main applications that differ in their objective (Kalaiselvam, 2014). One of these applications is using the stored heat for space or process heating. In other words, the heat itself is the desired effect. Anastasovski proposes the use of integrated TES in industrial processes to recover waste heat produced by the process (Anastasovski, 2017). The stored heat is then used later when it is required for another process that requires heat input. Another example of TES for purposes of heating is the use of phase change materials (PCM) in wallboards (Scalat, 1996). In this case, heat is stored and released during the phase change of a building material. This acts to stabilize the temperature fluctuation within a building and reduce heating load bottlenecks.

The other application is to use heat to generate electricity through some form of heat engine. In this sense, the heat is not the ultimate goal but is used as a means to achieve it. The latter of these two applications will be the focus of this work. More specifically, heat storage for electricity

generation to be used in conjunction with concentrated solar power (CSP) as the primary energy source will be investigated. However, since some of the methods used for space heating may be useful for electricity generation, the former will also be considered.

In addition to the two main applications of heat storage, the current technologies fit into one of three different storage methods; sensible heat, latent heat and thermochemical heat (Kalaiselvam, 2014). Each of these methods have their advantages and disadvantages. Therefore they, and devices that use them, will be thoroughly evaluated in order to select one that is suitable for a specific function and context. The following sections will define the methods and evaluate the technologies that make use of them.

## **2.2 Sensible Heat Storage**

Sensible heat is defined as thermal energy whose transfer to or from a substance results in a change of temperature. It can also be defined as the portion of the internal energy of a system associated with the kinetic energies of the molecules (Cengel & Boles, 2004). Since kinetic energy of molecules and atoms is related to temperature, it can be concluded that sensible heat is associated to a change of temperature (Schroeder, 2000). For example, if a certain quantity of a certain material experiences an increase in temperature, then it has absorbed a certain amount of heat. Consequently, the average kinetic energy of the molecules that make up the material is increased. For this type of storage, the most important property of the storage material is the specific heat capacity,  $c$ , which is defined as the amount of energy required to raise a unit mass by a unit temperature and is not a constant. It varies with temperature. Gases have two different heat capacities  $c_p$  and  $c_v$  denoting the heat capacity at constant pressure and at constant volume, respectively. Water, having a very high specific heat capacity of 4.18 kJ/kg/K at room

temperature is an excellent choice for space heating because it is abundant and cheap. Large underground water tanks are heated during the summer when the solar irradiance is high. The heat is then released during the winter for space heating when solar irradiance is low (IEA-ETSAP and IRENA, 2013). Using water for sensible heat storage has its limits. At atmospheric pressure, water will vaporize at 100 °C. Therefore, unless the water is stored at extremely high pressures, the temperature of the water cannot exceed 100 °C. This temperature limit is acceptable for space heating but if the goal is to produce electricity by means of a heat engine, higher temperatures are favorable. One of the implications of the second law of thermodynamics is that thermal efficiency increases with increasing difference of temperature between the heat source and sink, regardless of the type of heat engine used to convert heat to work (Cengel & Boles, 2004). Thus, sensible heat from water is far from ideal for electricity generation. Tiskatine et al. propose the use of natural rock as a high temperature heat storage for air based CSP plants. They concluded that granodiorite, dolerite, hornfels, gabbro and quartzitic sandstone are suitable minerals for this purpose (Tiskatine et al., 2017). Table 2.1 shows some different materials that have been considered for sensible heat storage.

**Table 2.1: Sensible heat storage materials (Kalaiselvam, 2014)**

<b>Material</b>	<b>Type</b>	<b>Temperature Range (°C)</b>	<b>Density (kg/m<sup>3</sup>)</b>	<b>Specific Heat Capacity (kJ/kgK)</b>	<b>Thermal Conductivity (W/mK)</b>
Thermalite Board	Solid	-	753	0.837	0.19
Fiberboard	Solid	-	300	1	0.06
Siporex Board	Solid	-	550	1.004	0.12
Polyurethane Board	Solid	-	30	0.837	0.03
Light Plaster	Solid	-	600	1	0.16
Dense Plaster	Solid	-	1300	1	0.5
Aluminum	Solid	up to 160	2707	0.896	204
Aluminum Oxide	Solid	up to 160	3900	0.84	30
Aluminum Sulfate	Solid	up to 160	2710	0.75	-
Cast Iron	Solid	up to 160	7900	0.837	29.3
Pure Iron	Solid	up to 160	7897	0.452	73
Calcium Chloride	Solid	up to 160	2510	0.67	-
Copper	Solid	up to 160	8954	0.383	385
Granite	Solid	up to 160	2640	0.82	1.7
Sandstone	Solid	up to 160	2200	0.71	1.83

Again, these materials have been considered only for space heating and not for running a heat engine. In order to achieve higher efficiency from the heat engine, a storage material that can withstand higher temperatures is required. *Science Applications International Canada* has proposed the use of ceramics, concrete, molten salts and synthetic oils as sensible heat storage materials for temperatures around 400 °C (Renewable Energy and Climate Change Program, SAIC Canada, 2013). Although the temperature is suitable for running a heat engine, the thermal conductivity of these materials is not high enough for the heat to be delivered to the engine at a high enough rate.

Most large scale CSP plants have a TES that makes use of molten salt as the storage material. Nine of these large CSP plants, developed by Luz International Limited, exist in the California Mojave desert and have a combined generating capacity of 354MW (Herrmann et al., 2004). The molten salt, being a liquid also acts as a heat transfer fluid. These plants operate with three different fluids; the HTF that circulates through the solar concentrator which is most commonly a synthetic oil, the molten salt as the storage material, and water as the working fluid of a Rankine power cycle. The oil is heated by solar radiation in the solar field, then circulates through a heat exchanger to heat either the cold salt storage tank or the water, depending on the time of day. The cold salt is heated from 300 °C to 385 °C and sent to the hot salt storage tank (Herrmann et al., 2004). With the increase in temperature and no phase change, this type of storage is inherently a sensible heat storage. When solar radiation is insufficient, the hot salt storage discharges while exchanging heat to the water, thereby turning it to superheated steam. This superheated, high pressure steam drives the turbine. A schematic of the CSP plants is shown in figure 2.1.

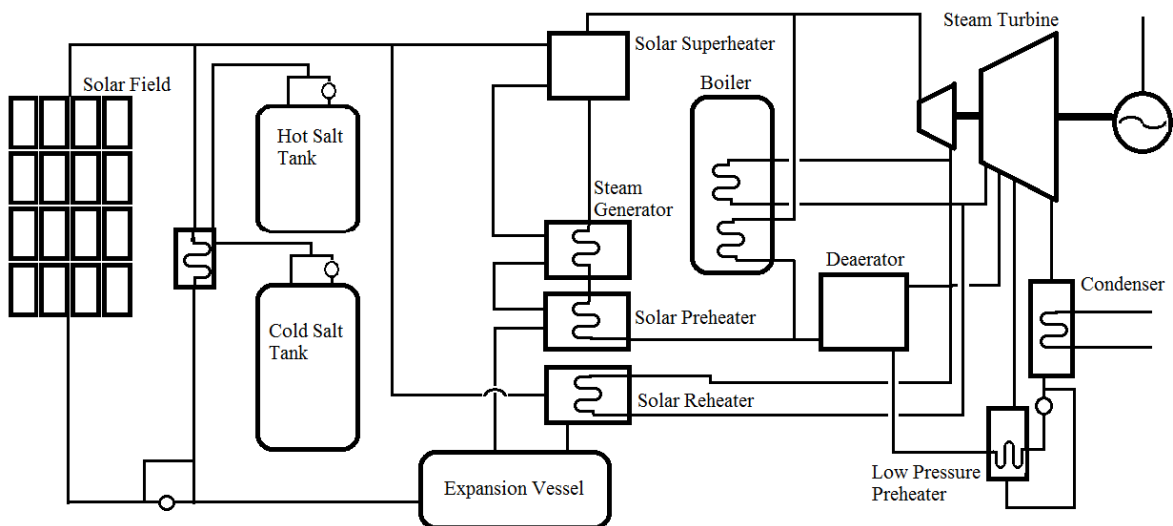


**Figure 2.1: Schematic flow diagram of a parabolic trough power plant with 2-tank molten salt storage (Herrmann et al., 2004)**

The salts used in the TES are typically inorganic nitrate salt mixtures such which consist of varying parts of  $\text{NaNO}_2$ ,  $\text{NaNO}_3$ ,  $\text{KNO}_3$  and  $\text{Ca}(\text{NO}_3)_2$ . These salt mixtures are chosen because of a good compromise between heat capacity, density, chemical reactivity and cost. They have freezing points varying from  $130\text{ }^\circ\text{C}$  to  $220\text{ }^\circ\text{C}$  (Herrmann et al., 2004). Evidently, the temperature of the salt must be kept above the freezing temperature to allow flow. Consequently, the storage tanks must be very well insulated to keep the temperature high and to minimize losses. Mostafavi et al. have investigated the techno-economic advantages of using single medium thermocline (SMT), dual media thermocline (DMT) and shell-and-tube (ST) systems that make use of porous concrete as filler material. Comparing these systems to the common two-tank molten salt system resulted in a reduction of 7%, 9% and 20% in electrical energy generated over one year for the SMT, DMT and ST systems respectively for the same theoretical storage capacity. Although they were found less performant than the two-tank molten salt system, the normalized cost per unit of electricity generated was 55% and 46% less for the DMT and ST systems respectively (Mostafavi et al., 2017). A DMT tank is cheaper but it has the problem of ratcheting stresses on the tank walls which could lead to mechanical failure of the tank (Mira-Hernandez & Garimella, 2014). During heating, the tank walls and the filler material expand differentially resulting in an annular gap between the two. The filler material, typically consisting of natural rocks, then settle to occupy the gap. When the tank cools, the rocks impede the contraction and introduce mechanical stress in the tank walls.

Although this general type of system has been deemed optimal for large scale commercial applications, it is not necessarily so for small scale, off-grid residential applications. Operating

between the same temperature range, a smaller storage tank scaled for the energy demands of a single home will require an excessive amount of insulation in order to maintain an acceptable heat loss. For example, if a large and a small storage are allowed, say, 5% of the total heat stored to be lost, the smaller storage will require a much thicker insulation.

Some industries and researchers have considered the use of graphite as a sensible heat storage material. An Australian utility company with a concentrated solar power plant uses high purity, high crystallinity graphite blocks as a heat storage material (<http://graphiteenergy.com/graphite.php>, 2015). The thermal properties of graphite seem to vary considerably depending on purity and crystallinity. One source states the thermal conductivity as 96 W/m/K (Entegris Inc, 2013) while another source states that it varies between 25-470 W/m/K (CERAM Research, n.d.). Entegris states that the thermal conductivity decreases with increasing temperature. However, the specific heat capacity increases with temperature. The specific heats at 600K and at 1000K are 1.42 kJ/kg\*K and 1.76 kJ/kg\*K respectively (Page, 1991). The mass of graphite required for a 25kWh storage device operating between these temperatures would be

$$m = (25 \text{ kWh}) * (3600 \text{ kJ/kWh}) / (1.59 \text{ kJ/kgK}) / (1000 \text{ K} - 600 \text{ K}) = 141 \text{ kg} \quad (1.1)$$

The advantages of using graphite are its high conductivity, high specific heat capacity, high temperature resistance and high thermal shock resistance. One of the disadvantages of using graphite is that it oxidizes, resulting in degradation and mass loss. The carbon in the graphite will react with an oxidizing agent and produce a gas. The oxidizing agent is mostly oxygen but can include water, nitrate and carbon dioxide (Entegris Inc, 2013). Significant oxidation occurs at

350 °C and the rate increases with temperature. Any ash remaining from the oxidation consists of the oxides of the metal impurities found in the graphite. Entegris does not suggest any methods of preventing oxidation but creating a barrier between the graphite and the oxidizing agent would theoretically work. Besides the oxidation problem, graphite seems to be a promising high temperature sensible heat storage material.

### **2.3 Latent Heat Storage**

Latent heat, as the name implies, is associated to a change in the lattice structure, or the geometric arrangement of atoms or molecules, of a substance. For example, liquid water, when heated to its boiling point will become a gas. During the vaporization, at a molecular level, the intermolecular Van der Waals bonds are broken and the molecules are freed from each other. Some heat is required to break these bonds. This heat, at a given temperature and pressure, is known as the heat of vaporization. The phase change can be reversed, in which case vapor condenses to liquid and the change is exothermic rather than endothermic. Even though liquid and gaseous water exist at the same temperature, the gas has more heat. This is an example of a phase change. Similarly, there is a heat of solidification, which again, can be endothermic or exothermic, depending on whether the change is from solid to liquid or the inverse. At the same temperature, a liquid has more heat than a solid for the same reason; heat is required to break bonds. The same amount of heat is returned when the bonds are reformed. Latent heat applies to any substance that can undergo a phase change. Some industries have made use of this concept as a heat storage method. Table 2.2 lists some common phase change materials (PCM).

**Table 2.2: Phase Change Materials (IEA-ETSAP and IRENA, 2013)**

<b>PCM</b>	<b>Melting Temperature (°C)</b>	<b>Melting Enthalpy (kJ/kg)</b>	<b>Density (kg/m<sup>3</sup>)</b>
Ice	0	333	920
Na-acetate-Trihydrate	58	250	1300
Paraffin	0 to 120	150 - 240	770
Erytritol	118	340	1300

As can be seen from table 2.2, none of these materials would be suitable for generating electricity from a heat engine since their equilibrium temperatures are too low. These would only be suitable for direct space heating or cooling. A PCM with a higher equilibrium temperature is required. In addition to low equilibrium temperature, these PCMs have low thermal conductivity so they do not transfer heat effectively. The use of miniature copper-water heat pipes embedded into the paraffin PCM as a method of improving the heat transfer has been proposed (Khalifa et al., 2016). Several different mixtures of salts are commonly used as PCM's whose melting temperature varies between 300 °C and 600 °C (Kalaiselvam, 2014). Some examples of these PCM's are mixtures of MgCl<sub>2</sub>, KCl and NaCl in varying concentrations and Na<sub>2</sub>CO<sub>3</sub>, K<sub>2</sub>CO<sub>3</sub> and Li<sub>2</sub>CO<sub>3</sub> also in varying concentrations of each salt (Kalaiselvam, 2014). The melting enthalpy of these salts typically vary between 177 kJ/kg and 858 kJ/kg but their thermal conductivities are quite low in the range of 0.5 W/mK to 1.2 W/mK (Kalaiselvam, 2014). Their melting enthalpies are adequately high but their very low thermal conductivities necessitate an added complexity to any system that makes use of them. Because of the low thermal conductivity, the heat transfer must be increased by convection when in the liquid phase which in turn requires pumps and a piping system. To further improve the heat transfer, some researchers have analyzed the possibility of nanoparticle additives in the molten salts and have found a 30% reduction in charging times (Miliozzi et al., 2015).

As mentioned, the thermal efficiency of a heat engine increases with increasing temperature. However, higher temperatures require materials that can withstand them, which in general, increases the cost. Higher temperatures are thus not necessarily desired. Besides the cost, achieving a high enough temperature to melt the PCM may not be possible, depending on the source of heat and the mechanical components of the system. For heat storage purposes of a solar concentrator, a temperature range of 400 – 600 °C is ideal. Zauner et al. have designed a latent-sensible heat storage based on HDPE as a PCM in a shell and tube arrangement. However, their maximum temperature was 154°C which is too low to run a heat engine efficiently (Zauner et al., 2017). One of the objectives of the storage device to be designed is to be able to store 25kWh of heat. Taking 33wt%NaCl-67wt% CaCl<sub>2</sub> as the heat storage material, the mass required to store 25 kWh would be

$$m = (25 \text{ kWh}) * (3600 \text{ kJ/kWh}) / (281 \text{ kJ/kg}) = 320 \text{ kg} \quad (2.2)$$

which seems like a large quantity (Kalaiselvam, 2014). These materials would be suitable if not for the fact that a large quantity would be required. The mass of 46 %LiF – 44% NaF<sub>2</sub> - 10% MgF<sub>2</sub> required would be much more practical and its thermal conductivity is higher.

$$m = (25 \text{ kWh}) * (3600 \text{ kJ/kWh}) / (858 \text{ kJ/kg}) = 104 \text{ kg} \quad (2.3)$$

This mass seems reasonable but this material will only melt at 632 °C, meaning that if that temperature cannot be obtained, then only sensible heat would be stored, making this material essentially useless. Considering the variable and unpredictable nature of solar irradiance,

guaranteeing this temperature is not likely. This material is also not mass produced and does not consist of abundant, cheap materials.

Sodium nitrate has been proposed as a higher temperature PCM for power-to-heat applications on industrial and domestic scales (Nepustil et al., 2016). The equilibrium temperature was 306°C and heat was provided with electric heating coils immersed directly into the PCM. The purpose of this device was ultimately for space and process heating, not for CSP generation. Although the temperature is relatively high for latent heat storage, it is inadequate for CSP. These salts also typically have low thermal conductivity. To address this problem, various configurations for exchangers between the PCM and the HTF have been proposed to enhance the heat transfer. One such configuration is concentric pipes with HTF in the inner pipe and PCM in the outer pipe (Ma et al., 2017). This research group proposed the use of eutectic carbonate nano-materials (62 mol%  $\text{Li}_2\text{CO}_3$  – 38 mol%  $\text{K}_2\text{CO}_3$ ) with melting point and heat of fusion of 484.8 °C and 311.8 kJ/kg respectively (Tao et al., 2015). This temperature would be suitable for CSP applications but the cost and availability of this material may be restrictive. The ideal class of PCMs for CSP applications are chlorides, carbonates and fluorides since they have an equilibrium temperature in the range of 500 °C to 800 °C (Paksoy, 2007).

Similarly to sensible heat storage, phase change materials as heat storage are most commonly used for space heating, not for use as input to a heat engine. The advantage of latent heat storage over sensible heat storage is that the energy density is significantly higher. They are thus better suited for long term, seasonal heat storage (Johansen et al., 2016). A brief description of the commonly used techniques with PCMs follows.

### **2.3.1 Direct Impregnation**

This is the simplest way of integrating a PCM into a building. The porous construction material such as wood, gypsum, concrete or plaster absorbs the liquid PCM (Hawes, 1991). The building envelope is thus saturated with the PCM. Hawes proposes the use of fatty esters, fatty alcohols and paraffins as impregnation materials in concrete. The PCM also acts to fill the pores of the building material and increase the thermal conductivity. During the day, the PCM will absorb heat while melting, keeping the building cool. During the night, it expels heat while it solidifies, keeping the building warm. Ultimately, the daytime to nighttime temperature variation is reduced. Employing this method would not only stabilize indoor temperature but would also stabilize heating load variation throughout the day, reducing the peak hours power demand from the electric utility (Karim Lee, 2014).

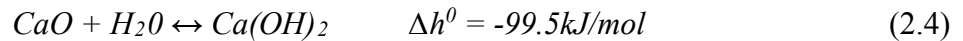
Some PCMs have been reported to leak out of the building material or to react chemically with it, which causes slow deterioration of the materials and reduces the effectiveness of the heat storage.

### **2.3.2 Microencapsulation**

This method consists of encapsulating powdered PCM into a polymeric micron sized polymeric capsule (Kalaiselvam, 2014). These capsules are then integrated into a composite building material. They are directly incorporated into the matrix material. This method eliminates chemical reactivity between the PCM and the building material as long as the polymeric capsule remains chemically inert and does not rupture. In either method, the most commonly used PCM is paraffin. CenoPCM microcapsules, as proposed by Liu et al. consist of hollow fly ash (cenospheres) from coal burning power plants coated in silica (Liu et al., 2017).

## 2.4 Thermochemical Heat Storage

Thermochemical heat, or thermochemical enthalpy, is the energy associated to a chemical reaction. Any chemical reaction has reagents and products. Two or more reagents combine and form a primary bond, either ionic or covalent, resulting in a third substance - the product. Before the bond is formed, the reagents are at a high energy state. Forming the bond lowers their energy state and releases energy in the form of heat. However, chemical reactions are reversible. If some heat is supplied to the product and the temperature is high enough, the primary bonds will break and the product will dissociate into its reagents. Precisely the same amount of heat is expelled during the formation of the product as is absorbed during the dissociation of the product. This heat and temperature are known as the enthalpy of reaction and equilibrium temperature, respectively. The following chemical reaction equation summarizes the process.



The double-sided arrow indicates that the reaction is reversible. From left to right, the reaction is exothermic, but will only occur if the temperature is below the equilibrium temperature. From right to left, the reaction is endothermic, but it will only occur if the temperature is above the equilibrium temperature. This particular example is the hydration of calcium oxide to form calcium hydroxide.

Thermochemical heat storage is similar to latent heat storage in that both are reversible, are the result of bonds forming and breaking, have an equilibrium temperature and the materials undergo a change of properties. However, latent heat storage materials undergo a phase change during

which the substance remains the same. Thermochemical heat storage materials undergo a chemical change, during which the substance becomes a different substance upon combining with another. For the purposes of heat storage suitability, thermochemical heat has a major advantage. The energy associated to bonds forming and breaking comes from primary bonds, whereas for latent energy, it is from secondary bonds. Primary (ionic or covalent) are much stronger than secondary (Van der Waals) bonds and have much higher bonding energies. Ultimately, what this means is that for the same heat storage capacity, a thermochemical storage will require much less material than a PCM storage.

**Table 2.3: Potential thermochemical TES materials (Renewable Energy and Climate Change Program, SAIC Canada, 2013)**

Material	Dissociation Reaction	Storage Density (kWh/m <sup>3</sup> )	Equilibrium Temperature (°C)
Calcium Sulfate	$\text{CaSO}_4 \cdot 2\text{H}_2\text{O} \leftrightarrow \text{CaSO}_4 + \text{H}_2\text{O}$	400	90
Iron Hydroxide	$\text{Fe}(\text{OH})_2 \leftrightarrow \text{FeO} + \text{H}_2\text{O}$	630	150
Magnesium Sulfate	$\text{MgSO}_4 \cdot 7\text{H}_2\text{O} \leftrightarrow \text{MgSO}_4 + 7\text{H}_2\text{O}$	633	122
Iron Carbonate	$\text{FeCO}_3 \leftrightarrow \text{FeO} + \text{H}_2\text{O}$	743	180
Ammonia	$2\text{NH}_3 \leftrightarrow \text{N}_2 + 3\text{H}_2$	800	450
Magnesium Hydroxide	$\text{Mg}(\text{OH})_2 \leftrightarrow \text{MgO} + \text{H}_2\text{O}$	943	250 - 400
Calcium Hydroxide	$\text{Ca}(\text{OH})_2 \leftrightarrow \text{CaO} + \text{H}_2\text{O}$	1260	550
Zinc Oxide	$\text{ZnO} + \text{C} \leftrightarrow \text{Zn}(\text{g}) + \text{CO}$	4571	1400

Table 2.3 lists some thermochemical heat storage materials that have been considered viable by various researchers and industries.

To qualify for the proposed design, the equilibrium temperature must be greater than 400<sup>0</sup>C. From table 2.3, ammonia, calcium hydroxide and zinc oxide would qualify. The highest enthalpy of reaction, or storage density, is also desirable. Zinc oxide has the highest, but its equilibrium temperature is much too high. It would be difficult to obtain the required temperature by concentrated solar radiation. Between ammonia and calcium hydroxide, the latter is the better choice since its storage density is significantly higher and it is abundant and cheap, not to mention that ammonia presents a corrosive, toxic and environmental hazard according to the globally harmonized system of hazardous materials. This leaves calcium hydroxide as the best choice in the list.

Calcium hydroxide is obtained by combining calcium oxide with water. Calcium oxide, also known as lime, is obtained from heating calcium carbonate, also known as limestone, according to the following reversible reaction.



Limestone is a naturally occurring compound and is abundant in Earth's crust. Furthermore, lime production is already a very large industry since it is used in construction mortar and chalk. Of the proposed thermochemical storage materials, calcium hydroxide may not have the highest storage density but it is definitely one of the cheapest, it is non-toxic and its equilibrium temperature is ideal for coupling with a heat engine. Most gas-solid thermochemical heat storages have either the packed bed, continuous or direct-type reactors with the packed bed reactor being the most common (Pan & Zhao, 2017). The packed bed reactor consists of solid powdered reactant laid in between the fins of a heat exchanger where heat transfer fluid

circulates. There is no contact between the solid reactant and the HTF. A continuous-type reactor simply a series of packed bed reactors. The direct-type reactor has no heat exchanger. Instead, the HTF is mixed with the reacting gas and flows directly through the solid reactant. Heat transfer is increased by the direct contact of the HTF with the solid particles. However, the significant friction in the flow through the powder causes a large pressure drop and requires more power to pump compared to packed bed reactors (Pan & Zhao, 2017). Tescari et al. suggests a solution to these problems with a rotary kiln reactor. This reactor has no HTF and the powdered reactant is heated directly by concentrated solar radiation while the reactor rotates (Tescari et al., 2014). The rotation mixes the powder to increase the heat transfer and to prevent agglomeration of the particles. The absorption-desorption of hydrogen by magnesium demonstrates better cycling characteristics than the hydration of CaO. Tests performed on MgH<sub>2</sub> by Paskevicius et al. demonstrate minimal degradation of the microstructure and performance of the heat storage material over 20 cycles (Paskevicius et al., 2015).

A calcium hydroxide based TES proposed by Y.A. Criado operates with the packed bed reactor concept (Criado et al., 2014). The reactor consists of storage tanks for liquid water, CaO and Ca(OH)<sub>2</sub>. During the discharging period, powdered CaO and steam enter the bed where the chemical reaction is allowed to occur. Thermochemical heat is released during the reaction and is used as output heat. The Ca(OH)<sub>2</sub> that exits the bed contains enough sensible heat to vaporize the liquid water flowing towards the bed as they exchange heat in a heat exchanger. The Ca(OH)<sub>2</sub> is then stored. During the charging process, concentrated solar radiation heats the Ca(OH)<sub>2</sub> in the fixed bed, producing steam and CaO. The CaO is then stored while the steam condenses in the heat exchanger in order to preheat the Ca(OH)<sub>2</sub> flowing towards the bed. The water is thus stored as a liquid. The general concept is shown in figures 2.2, 2.3 and 2.4.

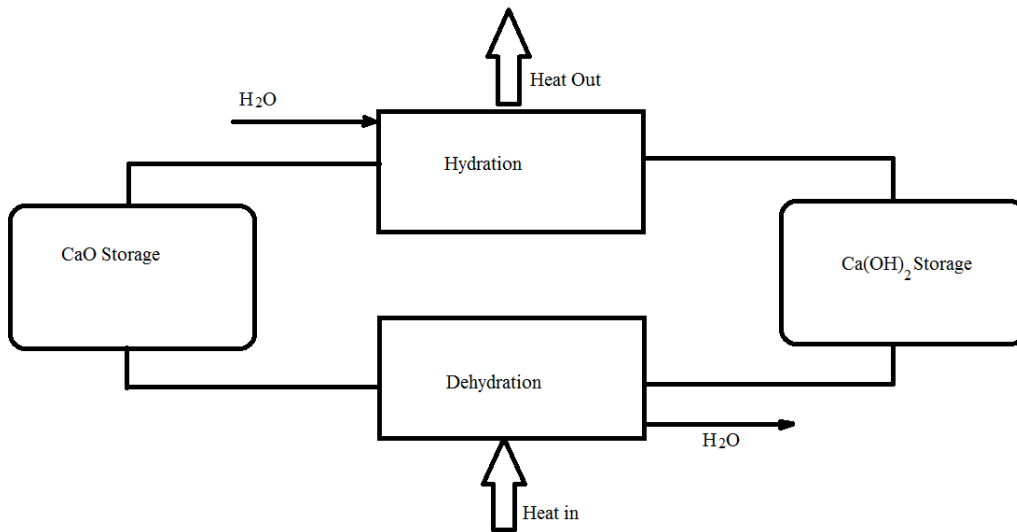


**Figure 2.2: General Concept of thermochemical CaO/Ca(OH)<sub>2</sub> TES (Criado et al., 2014)**

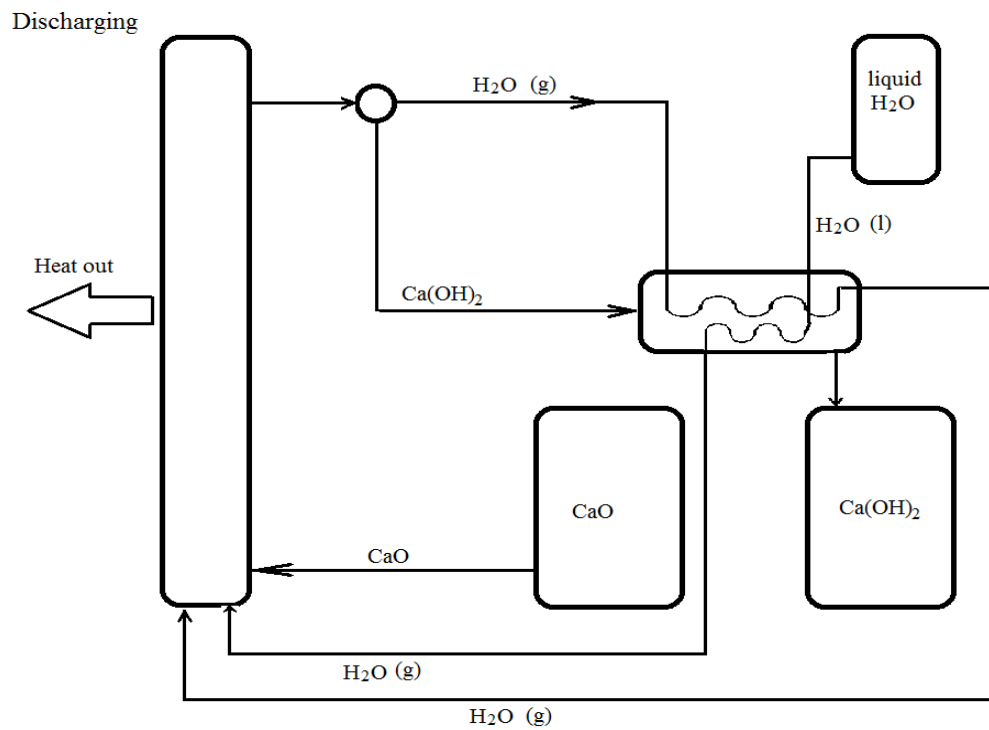


**Figure 2.3: Discharging Process Scheme of CaO/Ca(OH)<sub>2</sub> TES (Criado et al., 2014)**

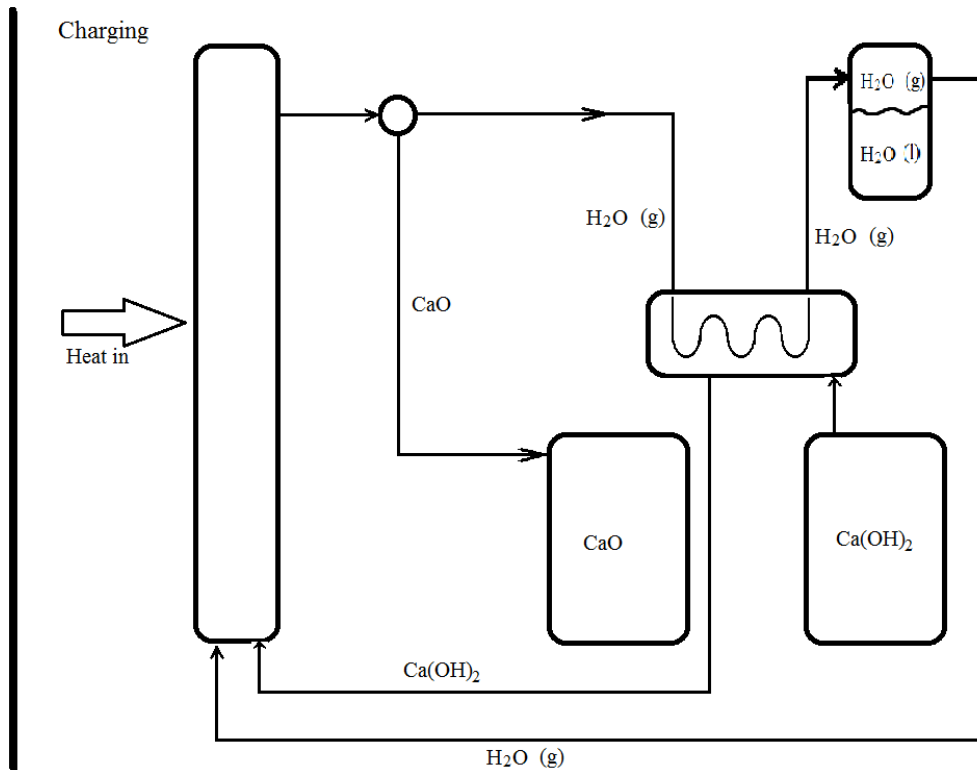


**Figure 2.4: Charging Process Scheme of CaO/Ca(OH)<sub>2</sub> TES (Criado et al., 2014)**

As mentioned, calcium oxide reacts with carbon dioxide, therefore it is important that no air is allowed into the system in order to prevent the formation of calcium carbonate. This reaction is also reversible with an even higher enthalpy of reaction than the hydration of calcium oxide but the equilibrium temperature is approximately 850 °C (Halikia et al., 2001), which may be excessive. It is also important that the water reacting with the calcium oxide is vaporized before the reaction. Otherwise, a large portion of the heat produced by the reaction will be used to vaporize that water and will thus not be available for its intended application.

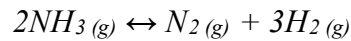
Schmidt et al. have found the discharge power of the CaO/Ca(OH)<sub>2</sub> system with a packed bed reactor to be 325 kW/t-Ca(OH)<sub>2</sub> (Schmidt et al., 2015). They noted, however, that after several cycles, the solid particles agglomerated, resulting in reduced heat transfer. SiO<sub>2</sub> nano-particles were introduced to reduce this effect. Sakellariou et al. have introduced aluminum particles with

the calcium oxide as another means of enhancing the particle integrity and crystallinity, ultimately to reduce cycling degradation (Sakellariou et al., 2015).

This proposed scheme is intended for a large scale TES. Scaling it down to a residential level may not be economically justifiable considering the amount of components involved. This remains to be determined. However, a hybrid reactor in which both hydration and carbonation of CaO is allowed may be advantageous. In this case, ambient air would flow through the powdered CaO. The already vaporized moisture contained in the air would produce  $\text{Ca(OH)}_2$  and the  $\text{CO}_2$  contained in the air would produce  $\text{CaCO}_3$ . There would be no need for a water storage tank and heat exchanger, ultimately reducing the cost. As long as the solar concentration factor is high enough such that the fluidized bed reaches temperatures above  $850\text{ }^\circ\text{C}$  during charging, no immediate complications are evident.

One research group has investigated the possibility of a thermochemical heat storage based on the carbonation of CaO. They found that the high reaction temperature resulted in sintering of the powdered CaO after several cycles. This problem was addressed by intermediate hydration of the CaO as well as the addition of  $\text{Al}_2\text{O}_3$  composites (Obermeier et al., 2017). Although their research showed that alternating between carbonation and hydration reduced degradation of the CaO powder, it did not address the question of whether simultaneous hydration and carbonation is feasible. However, Yan et al. investigated the effect of  $\text{CO}_2$  on the hydration reaction of CaO and found that even 1% molar  $\text{CO}_2$  severely reduced the cyclic storage capacity of the system due to formation of  $\text{CaCO}_3$  (Yan et al., 2017). However, the highest test temperature was  $500\text{ }^\circ\text{C}$ , which is not high enough to reverse the carbonation. No research paper could be found that addressed the simultaneous hydration and carbonation of CaO as a potential heat storage method.

Literature on calcium oxide as a heat storage material for CSP is abundant, most probably because of its high equilibrium temperature, high storage density and low cost. Thus far, it seems to be the best candidate, considering all aspects. Other, less frequently investigated materials should also be considered. The gas-gas dissociation of ammonia has also been investigated by several researchers.



This reversible reaction at 20 MPa and 300 K, has an enthalpy of 66.8 kJ/mol. A reactor was tested with a 20 m<sup>2</sup> parabolic dish concentrator. (Lovegrove & Luzzi, 1996). Another potential reversible reaction is the dissociation of silicon trioxide with an equilibrium temperature in the range of 773-873 K with the presence of a catalyst. Dayan et al. found that the storage efficiency of this integrated into a solar-steam cycle was 58% (Dayan et al., 1979). In fact, the list of possible reactions is very long.

**Table 2.4: Promising thermochemical heat storage reactions (Yan et al., 2015)**

Reaction	Specific Enthalpy (kJ/mol)	Equilibrium Temperature (K)
$BaO_2(s) \leftrightarrow BaO(s) + 1/2O_2(g)$	80.9	1011
$PbO_2(s) \leftrightarrow PbO(s) + 1/2O_2(g)$	55.1	565
$LiO_2(s) \leftrightarrow Li_2O(s) + 1/2O_2(g)$	38.4	460
$MgO(s) \leftrightarrow Mg(g) + 1/2O_2(g)$	752	3360
$ZnCO_3(s) \leftrightarrow ZnO(s) + CO_2(g)$	67	406
$SrCO_3(s) \leftrightarrow SrO(s) + CO_2(g)$	234	1381
$Mg(OH)_2(s) \leftrightarrow MgO(s) + H_2O(g)$	84	531

Some researchers have attempted to increase the efficiency of thermochemical heat storage devices based on salt hydrates by recovering condensation heat rejection to the environment. This cascade device is a two-stage device that recovers the heat rejection by condensation that would otherwise be lost. They found that the exergy of the device increased by a factor of 1.8 (N'Tsoukpoe et. al, 2016).

#### **2.4.1 Hydrogen Energy Storage**

The heat from concentrated solar radiation can also be stored thermo-chemically in hydrogen. Although this method is not based on a reversible chemical reaction, it can serve the purpose of creating fuel from concentrated solar radiation. Rather than the typical CSP plant arrangement in which solar radiation heats the storage, which in turn heats and HTF that drives a turbine to ultimately drive a generator, this system would heat the HTF directly without the intermediary heat storage. The electrical work produced by the generator would power the electrolysis of water to produce H<sub>2</sub> gas as a combustible fuel. The energy is thus stored as a fuel (Dincer & Rosen, 2011).

#### **2.5 Hybrid Heat Storage**

Hybrid heat storage devices are an attempt to retain the favorable characteristics of different types of storage methods such as sensible, latent or thermochemical, while minimizing the unfavorable characteristics. Such a device combines two or more of the main types such as the one proposed by Ströhle et al. which combines sensible heat storage and thermochemical heat storage into one device. The majority of the heat is stored in the sensible heat section consists of natural rocks as the storage material. To solve the problem of unsteady temperature and heat flux during discharging common to all sensible storage devices, the thermochemical section acts as a throttling component. By controlling the pressure in the reactor with a compressor, the reaction

can occur at any chosen temperature. Thus, when the sensible section is nearly depleted and relatively cool, the reaction temperature can be lowered such that the reactor can still draw low temperature heat to drive the reaction and charge. Once the thermochemical section is charged, the pressure and reaction temperature are increased to obtain higher thermal efficiencies for the heat engine. A transient simulation of this concept performed by the research group found energy and exergy efficiencies of 95.6% and 94% respectively (Strohle et al., 2017).

Frazzica et al. have investigated the efficiency of a sensible-latent hybrid heat storage for domestic space heating applications. The device is essentially a hot water tank with micro-encapsulated PCMs mixed in the water. Two different PCMs were tested; paraffin and a salt hydrate. Tests run on such a device with 2.7% salt hydrate by volume yielded a 10% increase in the storage density compared to pure water (Frazzica et al., 2016). However, this method is not viable for CSP applications since the temperature is too low.

If air is used as the HTF between the storage and the heat engine, Agrafiotis et al. suggest the use of porous ceramic structures coated with a  $\text{Co}_3\text{O}_4/\text{CoO}$  redox system (Agrafiotis et al., 2015). The air carries the oxygen required for the reversible redox reaction while the porous ceramic acts as the structure, increases surface area and provides some sensible heat storage. The system is thus a thermochemical-sensible hybrid heat storage.

Most large CSP plants store heat in molten salts because of their high heat capacities and cycling stability. Beltran et al. have conducted experiments and computer simulation to determine the enthalpy of fusion of nitrate salts as potential sensible-latent hybrid heat storage materials. In the case of  $\text{NaNO}_3$ , the enthalpy of fusion accounted for 3% of the total energy stored over the temperature range (Beltran et al., 2017).

### **Chapter 3: Methodology**

This thesis addresses the requirements of the heat storage device and how they might best be achieved. There is no single correct way in which this could be done. Instead, it presents a suggested design that can serve as schematics or simply as a guide for other designs. While the intent of this research is to design and test a heat storage device, some design concepts have yet to be validated and some critical information is missing in order to make the best design decisions. Therefore, the experimentation that was conducted served to quantify certain aspects and components of the heat storage and to justify implementing the design choices.

Before determining what tests should be done, a preliminary concept for the functioning of the heat storage was needed as well as the heat storage material. It was decided by the involved parties, that this heat storage would be a graphite based sensible heat storage with inward heat flux in the form of solar radiation and outward heat flux as conduction to a heat engine. With this established, the required tests were determined.

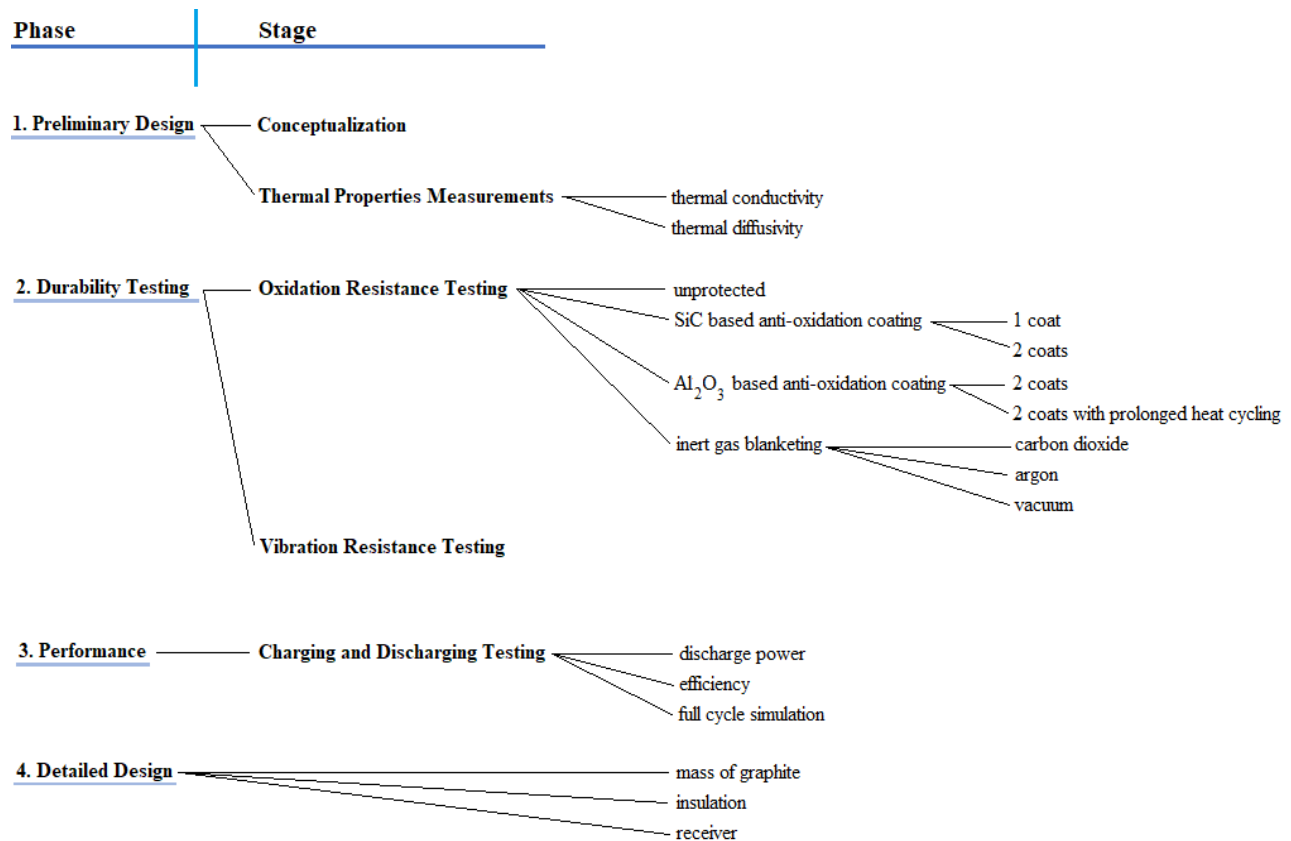


**Figure 3.1: Work Flow Chart**

Prior to conducting tests concerning durability and performance, the thermal properties of the graphite needed to be measured. Graphite exists in many forms and microstructure and the graphite samples provided by the manufacturer came with no specified properties. Therefore, measuring the thermal properties of these samples was critical to designing and testing a heat storage based on this graphite. The thermal conductivity and thermal diffusivity were both measured at several different temperatures. From these quantities, the specific heat capacity was calculated.

As mentioned in the problem statement, the factors defining the quality of the heat storage are the durability and the performance of the heat storage. For durability, the primary concern is the oxidation of the graphite. In order to anticipate and prevent oxidation problems in the heat

storage design, the oxidation behavior of some graphite samples was investigated in a series of tests. These tests served to determine the oxidation rate of the graphite provided by the manufacturer and to evaluate the effectiveness of several oxidation prevention methods. Since graphite exists in many forms, the results obtained from these tests were specific to these samples. The methods to prevent oxidation that were tested were two different types of coatings, inert gas blanketing with argon and with carbon dioxide and oxygen removal. Having obtained the oxidation rates using any of these methods, the best one could be selected and the lifespan of the heat storage could be evaluated.

Next, more testing was conducted to evaluate the performance of the heat storage. This was accomplished by testing a bench top scaled down model of the heat storage. While this model was not an exact scaled down replica with all the components of the prototype, it had the necessary components required to test the heat transfer mechanisms. The model consisted of an insulated block of graphite in contact with some resistance heaters on one side and a water-cooled heat sink on the other. While the mechanisms of heat transfer for a heat sink and resistance heaters differ from that of solar radiation and an engine, a dimensionless number was introduced as a means of establishing an equivalent heat transfer. In this way, the results obtained from the model could be applied and scaled up for the actual prototype. The details of how this was accomplished are explained in chapter 6.

Finally, the durability of the heat storage was once again evaluated. Since the device's intended use is to provide heat to a Stirling engine with reciprocating pistons, it will be subjected to vibration due to the contact between the two. Again, a scaled down model of the prototype was subjected to vibration conditions that were expected for the actual prototype in order to test the degrading effects of vibration on the structure. This scaled down model also was not an exact

replica and only had the necessary components for testing the effects of vibration. This test applied more specifically to the graphite – the heat storage material – rather than the device itself.

A more detailed methodology and description of the experimental setup for each of these aspects are laid out in the relevant chapters.

After having obtained the results of all the tests, the design of the heat storage was completed based on the results. Chapter 8 presents an analysis of the design and the specifications and technical drawings are shown in appendix A.

### **3.1 Performance**

In general, the performance qualifies how well the storage accomplishes its task of absorbing, retaining and dispensing heat. These three tasks can be quantified by charging efficiency and the charging-discharging efficiency. The charging efficiency  $\eta_c$  is defined as the ratio of heat absorbed  $Q_c$  by the graphite to the incident concentrated solar radiation  $Q_{sol}$ . Some of the incident solar radiation will be absorbed by the graphite and then lost by re-radiation from the surface of the graphite or by convection to ambient air.

$$\eta_c = \frac{Q_c}{Q_{sol}} \quad (1.1)$$

The discharging efficiency  $\eta_d$  is defined as the ratio of the heat discharged  $Q_d$  to the engine to the heat absorbed by the solar radiation over an 18-hour storage period. The solar radiation is

considered negligible for 18 out of 24 hours during which the graphite absorbs no heat. During these 18 hours, losses will occur by conduction through the insulation.

$$\eta_d = \frac{Q_d}{Q_c} \quad (3.2)$$

The overall efficiency  $\eta$  is the product of the charging efficiency and the discharging efficiency.

$$\eta = \eta_c \eta_d \quad (3.3)$$

Another performance parameter is the heat rate discharged to the engine  $\dot{Q}_d$ . If the discharging heat rate is too small, the engine will stall. If the heat rate is too high, the rate of electricity production will exceed the demand for the first few hours of discharging and the heat storage will quickly be depleted. Therefore, the discharge heat rate must be kept above the stalling heat rate and controlled to match the demand. This performance parameter is qualitative.

Chapter 6 describes the tests involved in quantifying the performance as well as the results obtained from these tests.

### **3.2 Durability**

Chapters 5 and 7 are about oxidation and vibration resistance respectively. Together, these chapters describe the tests and results that define the durability of the prototype. It is obviously desirable for the heat storage to last for as many charging cycles as possible without degrading its performance or requiring maintenance. The main obstacle for this is the oxidation of the graphite. At high temperatures, the carbon in the graphite will react with oxygen, producing

carbon dioxide. Thus, solid carbon is lost and the mass of the graphite is reduced which in turn reduces the heat capacity of the storage. The graphite also becomes more porous, which reduces the thermal conductivity. So, the oxidation rate must be kept to a minimum. In addition, the casing and insulation must withstand high temperatures, high or low pressures and moisture. In addition, the graphite will be subject to vibrations caused by the reciprocating engine. This vibration could cause excessive wear or cracking on the surface of the graphite. This must be minimized. Figure 3.1 summarizes how each parameter ultimately affects the heat storage quality.

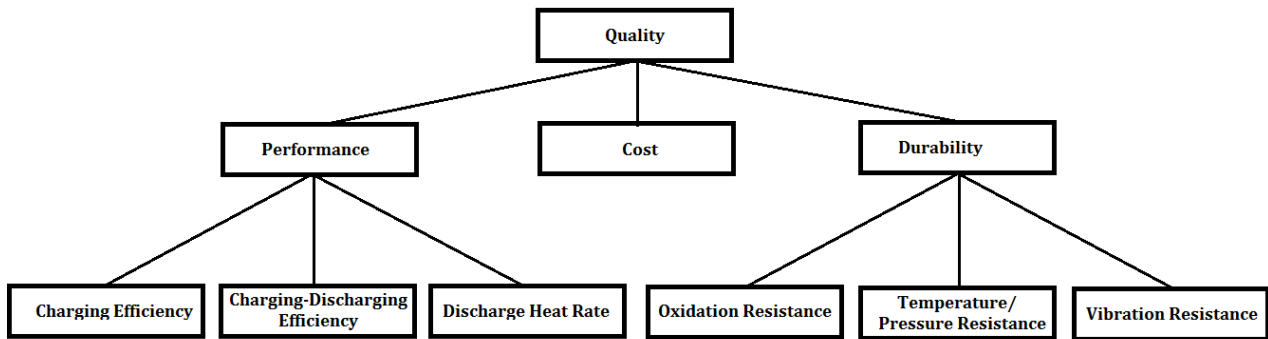


**Figure 3.2: Factors affecting TES quality**

## Chapter 4: Thermal Properties of Graphite

The supplier of the graphite used for the heat storage prototype did not provide any specifications or properties for the graphite other than that one was higher grade and one was lower grade. Lacking this information, some tests were conducted to determine the thermal properties of the graphite. Since the graphite was to be used for sensible heat storage, the most important material properties are the specific heat capacity and the thermal conductivity.

The specific heat capacity is a critical property since it determines how much heat can be stored, per unit mass, for a certain amount of material and temperature range. Therefore, a material with a high heat capacity is desired.

In addition to its ability to store heat, the material must also be able to absorb and release heat at an acceptable rate. The material property that governs this ability is the thermal conductivity.

### 4.1 Thermal Conductivity

The driving force of heat transfer by conduction through a material is a temperature gradient with the heat flowing from high to low temperature. The thermal conductivity  $k$  of a material is a measure of the ease with which heat can flow through the material and is simply the constant of proportionality between heat flux and temperature gradient. For one dimensional heat flow

$$q \propto \frac{dT}{dx} \quad (4.1a)$$

$$q = -k \frac{dT}{dx} \quad (4.1b)$$

where direction of the heat flux  $q$  is parallel to  $x$ . In the case of one dimensional and steady heat conduction, the temperature gradient is linear such that

$$q = -k \frac{\Delta T}{\Delta x} \quad (\text{W/m}^2) \quad (4.1c)$$

Taking into consideration the cross-sectional area through which the heat flows, the heat rate is given by

$$\dot{Q} = -kA \frac{\Delta T}{\Delta x} \quad (\text{W}) \quad (4.1d)$$

so that

$$k = -\frac{\dot{Q}\Delta x}{A\Delta T} \quad (\text{W/mK}) \quad (4.1e)$$

However, like other thermal properties, the thermal conductivity is not constant. It depends on the temperature of the material.

The purpose of this test was to empirically determine the thermal conductivity of the two different grades of graphite at different temperatures. Several methods to measure thermal conductivity exist but they vary very slightly. All of them consist necessarily of establishing steady state, one dimensional heat conduction while measuring the temperature gradient and the heat flow.

The details of the test apparatus used to determine the thermal conductivity of the graphite samples is shown in figure 6.1.

The graphite block was heated at constant power by the resistance heater on one side while it was cooled on the opposite side by the water-cooled heat sink in order to establish a temperature gradient. This simultaneous heating and cooling was maintained until the temperature of the graphite block reached steady state, ensuring that the temperature gradient was linear and constant. Once steady state was reached, the heater power was reduced and the graphite was allowed to cool until steady state was reached once again. This was repeated several times for different steady state temperatures.

All six temperatures, the input power and the water flow rate were measured and recorded every minute for the duration of the test. Knowing the temperatures at thermocouple 1 and 3 and the distance between them, the temperature gradient was calculated at steady state and was related by equation 4.1e to the heat removal by the heat sink.

The heat flow was constrained to one dimension by insulating the sides of the graphite which only allowed for heat to flow from bottom to top. The one-dimensional flow was ensured by comparing  $T_2$  and  $T_4$ . The fact that  $T_2$  and  $T_4$  were always nearly identical implied that the plane parallel to the heated surface that contains  $T_2$  and  $T_4$  had nearly zero heat flux in it since the temperature gradient in that plane was nearly zero. Of course, some small amount of heat is lost through the insulation which implied that there was some heat flow in the horizontal direction. It is precisely for this reason that the vertical temperature gradient was related to the heat removal by the heat sink and not to the heat provided by the heater.

In other words, the horizontal temperature gradient, which is very small, is attributed to the heat loss through the insulation, which is also very small. The vertical temperature gradient is associated to the heat removed by the heat sink. The sum of the horizontal and vertical components of heat flow is equal to the heat provided by the heater.

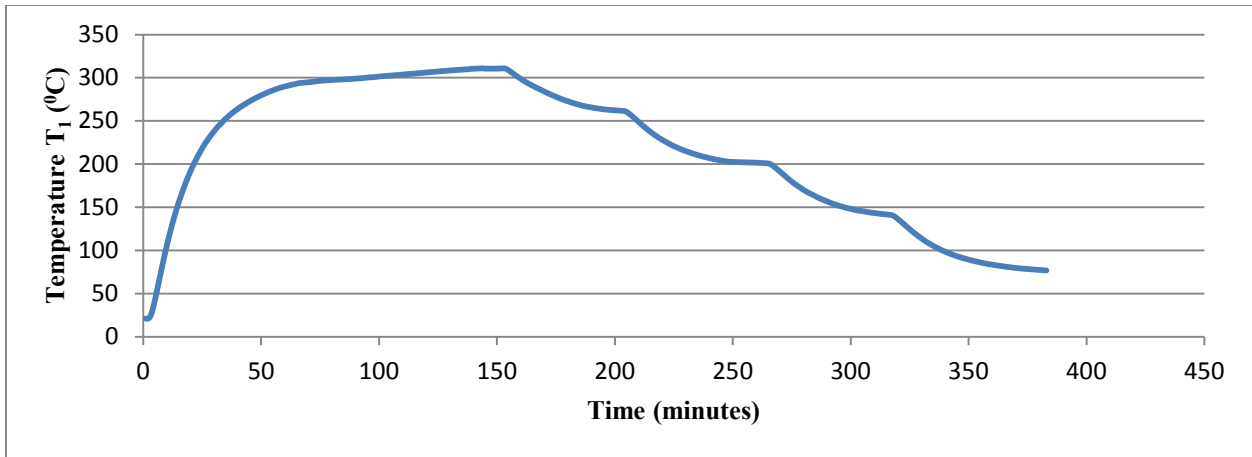
The heat removal by the heat sink was calculated by applying an energy balance on the flowing water. Knowing the specific heat capacity of water, the internal energy change of the water, as it flows through the sink is

$$\dot{Q}_{out} = \dot{m}c(T_6 - T_5) \quad (\text{W}) \quad (4.2)$$

The thermal conductivity was calculated by substituting equation 4.2 into the definition of the thermal conductivity

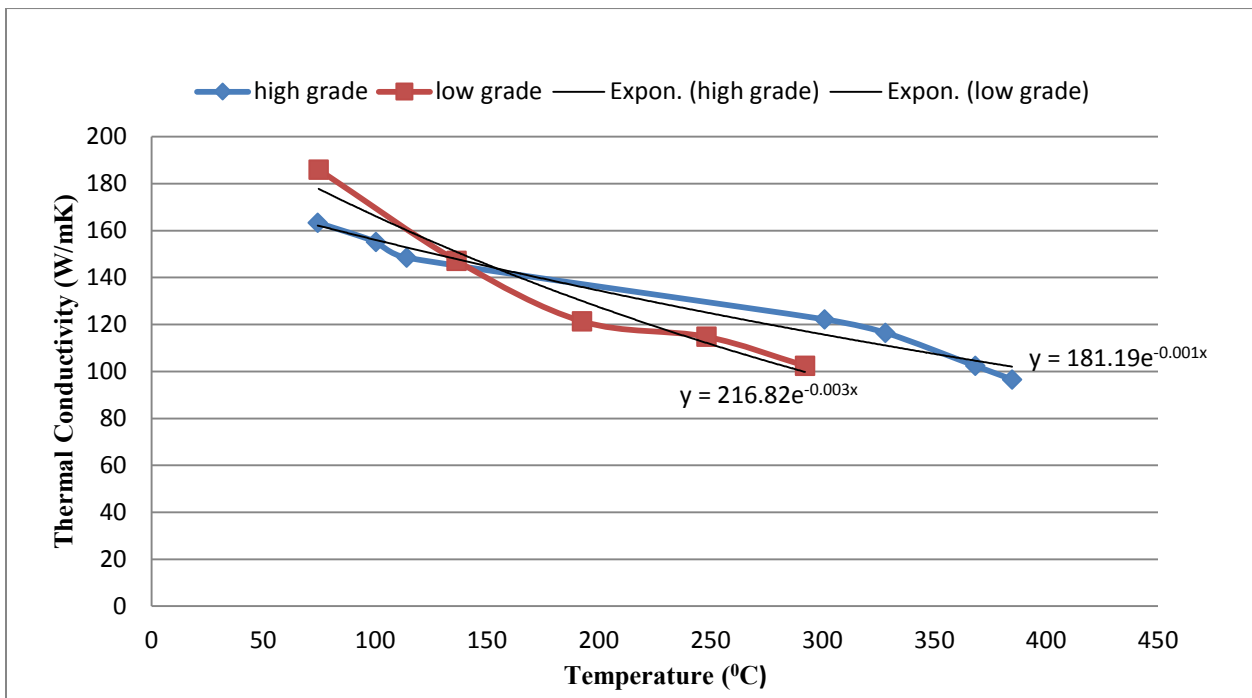
$$k = \frac{\dot{m}c(T_6 - T_5)\Delta x}{A(T_1 - T_3)} \quad (\text{W/mK}) \quad (4.3)$$

Figure 4.1 summarizes the experimental procedure. The thermal conductivity was calculated from the measured temperatures at the steady points, where the slope was nearly zero, just before the discontinuities. The discontinuities were due to sudden change in power supplied by the heater. The sudden change in power was done deliberately in order to decrease the temperature. The slopes before the discontinuities were not exactly zero but they were close enough to assume a linear temperature gradient. Reaching true steady state would have taken an excessive amount of time.



**Figure 4.1: Reaching steady state temperatures for measuring thermal conductivity**

Figure 4.2 shows the thermal conductivities of both grades of graphite as a function of their temperature.



**Figure 4.2: Thermal conductivity of graphite as a function of temperature**

There is considerable error in these results but the trendline, which is expected to be an exponential function, mitigates the error. As expected, the high grade graphite typically has higher thermal conductivity. It also varies less with temperature.

The high grade graphite, having a higher density than the low grade graphite, had a lower porosity and a higher degree crystallinity. With higher porosity, the effective cross-sectional area of the material is less than the actual cross-sectional area because some fraction of the area is occupied by gases rather than the graphite. In this case, the gas was air, which has a much lower thermal conductivity than graphite. These air-filled pores impede the heat flow. As a result, the thermal conductivity of the bulk material is a function of its porosity. Several models exist for the relationship between thermal  $k$  conductivity and porosity  $f$ . The Maxwell model suggests

$$k = k_0 \frac{1 - f}{1 + 0.5f} \quad (4.4)$$

where  $k_0$  is the thermal conductivity of the perfectly crystalline, non-porous material (Colbert et al., 2014). The porosity  $f$  is defined as the ratio of the number of vacant atoms to the number of atoms in a perfect crystal.

$$f = \frac{N_c}{N_p} = \frac{4}{3} \pi \left( \frac{r}{b} \right)^3 \quad (4.5)$$

In equation 4.5,  $r$  is the average radius of the pores and  $b$  is the lattice parameter of the crystalline cubic unit cell. None of these parameters were known for the graphite samples, however, the model provides some insight as to why the lower grade graphite had lower conductivity.

## 4.2 Thermal Diffusivity

The ability of a material to absorb and store heat is quantified by its thermal diffusivity, defined as

$$\alpha = \frac{k}{\rho c} \quad (\text{m}^2/\text{s}) \quad (4.6)$$

It relates all material properties that influence heat transfer. It is a secondary material property defined by more fundamental concepts such as density, thermal conductivity and specific heat capacity. Although the specific heat capacity is a critical property for a heat storage, this property alone does not ensure a good heat storage since the amount of heat it can absorb and contain will also depend on the mass, and therefore the density, and the conductivity. It was defined merely due to convenience as it appears in the general heat conduction equation.

$$\frac{\partial}{\partial x} \left( k \frac{\partial T}{\partial x} \right) + \frac{\partial}{\partial y} \left( k \frac{\partial T}{\partial y} \right) + \frac{\partial}{\partial z} \left( k \frac{\partial T}{\partial z} \right) + \dot{q} = \rho c \frac{\partial T}{\partial t} \quad (4.7a)$$

Assuming constant thermal conductivity  $k$ , it can be taken out of the brackets such that

$$\frac{\partial^2 T}{\partial x^2} + \frac{\partial^2 T}{\partial y^2} + \frac{\partial^2 T}{\partial z^2} + \frac{\dot{q}}{k} = \frac{\rho c}{k} \frac{\partial T}{\partial t} \quad (4.7b)$$

The coefficient in front of the time derivative on the right side is simply the reciprocal of the thermal diffusivity. Thus, in short-hand notation, for constant thermal conductivity, the general heat conduction equation becomes

$$\nabla^2 \cdot T + \frac{\dot{q}}{k} = \frac{1}{\alpha} \frac{\partial T}{\partial t} \quad (4.7c)$$

A test was conducted to determine the thermal diffusivity of the two grades of graphite at different temperatures. The intent was to determine the specific heat capacity, which could be obtained if the density and thermal conductivity were also known. The apparatus used to measure the thermal diffusivity was a Netzsch LFA 447 laser nano-flash device. The device exposes the front face of the sample to a short pulse of light and measures the temperature rise of the back face of the sample using an infrared detector. The signal from the detector is amplified and corrected for initial temperature and ambient conditions so that the temperature rise is due to the light pulse alone. The integrated software calculates the thermal diffusivity  $\alpha$  using the model proposed by Parker et al.

$$t_{50} = \frac{0.1388d^2}{\alpha} \quad (4.8)$$

where  $d$  is the sample thickness and  $t_{50}$  is the time at which  $T/T_{peak} = 0.5$  (Parker & Jenkins, 1961). The thermal diffusivity was measured in this manner for sample initial temperatures ranging from 25 °C to 295 °C at 30 °C intervals for a total of 10 measurements per sample.

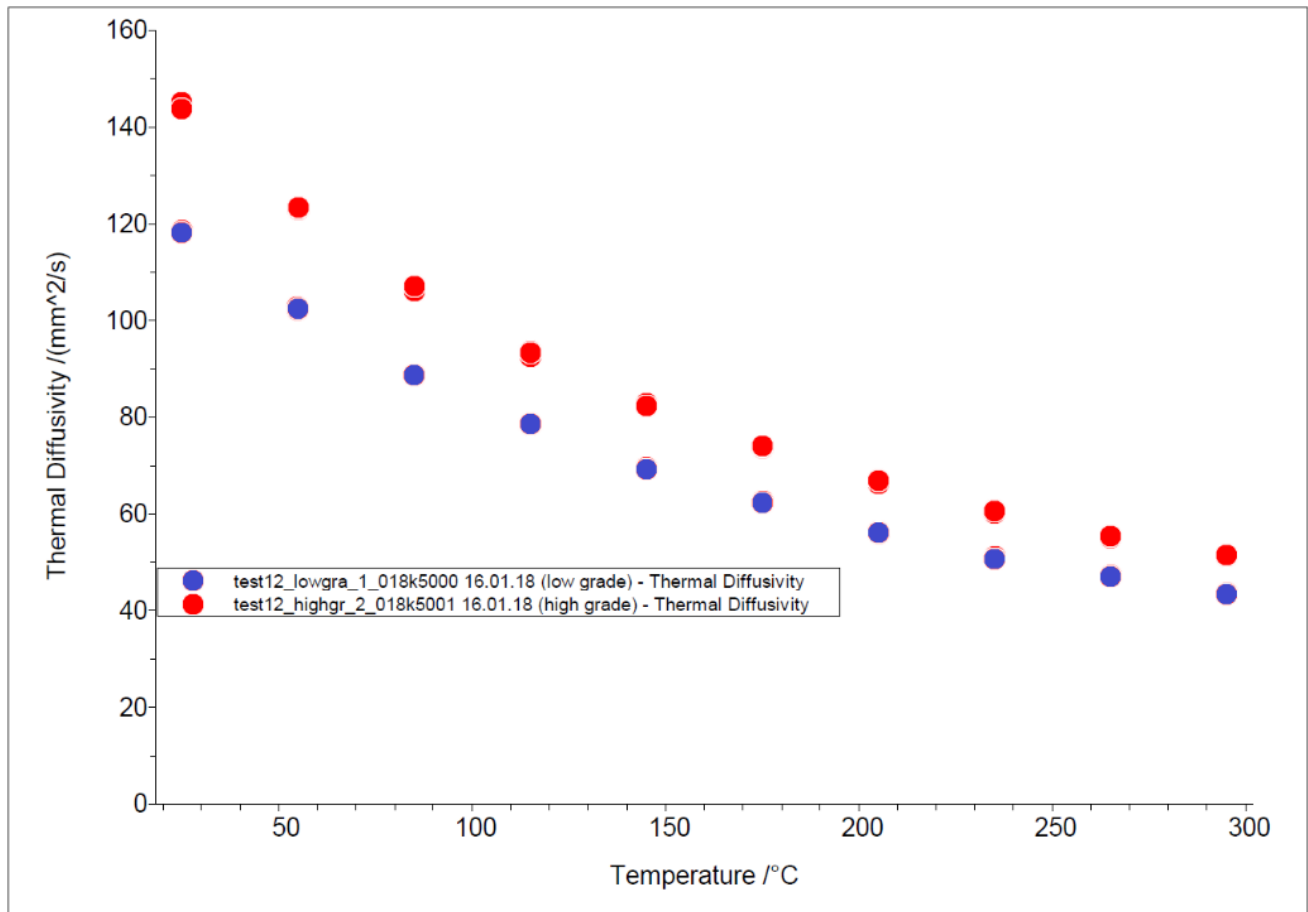


**Figure 4.3: Thermal diffusivity of graphite as a function of temperature**

Next, to determine the specific heat capacity of the graphite, the thermal diffusivity was compared to their thermal conductivity and density at the corresponding temperatures using equation 4.6. Since the data obtained from the thermal conductivity test was not measured at the same temperatures, the curve fitting exponential functions shown in figure 4.2 were used.

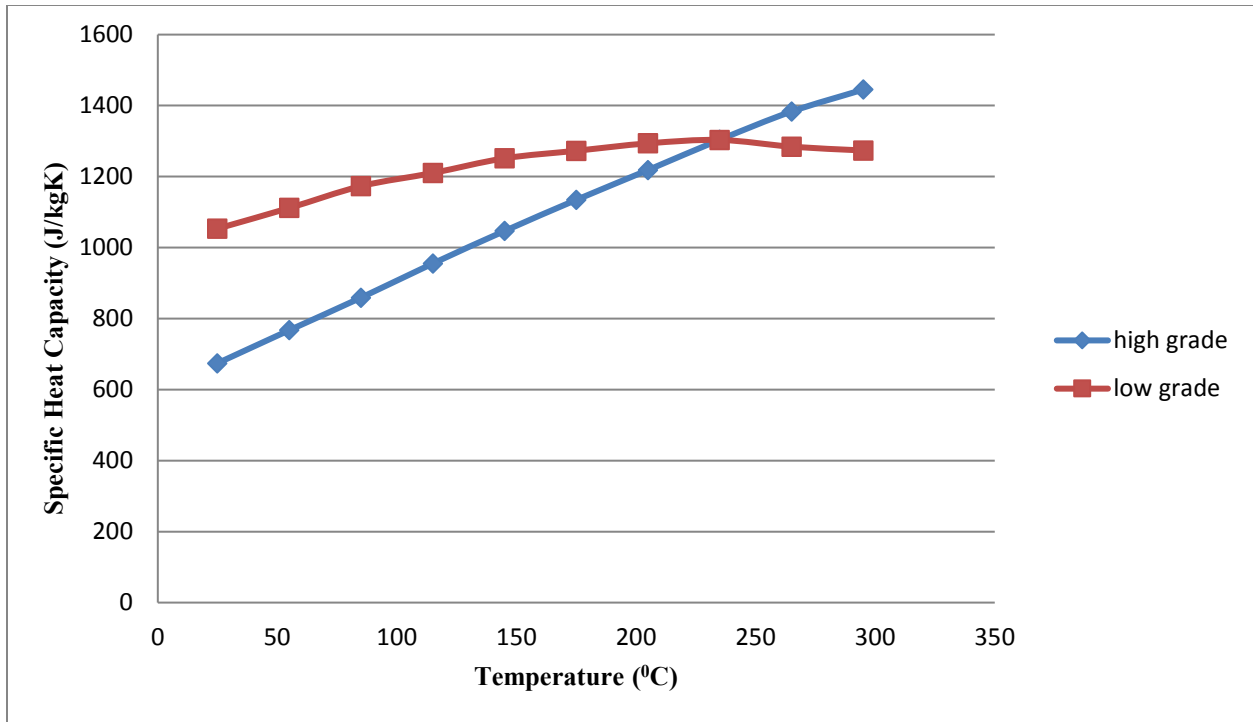


**Figure 4.4: Specific heat capacity of graphite as a function of temperature**

From the measured values of thermal conductivity and specific heat capacity obtained from these tests, we can see that the thermal properties of these two grades of graphite are comparable to those of aluminum, which is often chosen as a material for its favorable thermal properties. Aluminum is often used in cookware, finned heat sinks and radiators because of its ability to conduct and store heat. Therefore, an aluminum based sensible heat storage would be approximately as effective as a graphite based storage with the exception that graphite has a much lower cost, in general. In addition, aluminum has a melting temperature of 660 °C which imposes a limit on the maximum temperature of the storage whereas graphite can reach much higher temperatures, as long as oxidation is prevented with any of the available methods.

## Chapter 5: Oxidation of Graphite

### 5.1 Silicon Carbide Based Anti-oxidation Coating

The purpose of this experiment was to determine the effectiveness of the *Aremco Pyro Paint<sup>TM</sup> 634 SiC* anti-oxidation coating that was applied to graphite blocks.

In order to assess the effectiveness of the coating, the oxidation rate with the coating should be compared to the oxidation rate without the coating. Thus, a test was conducted to determine the oxidation rate of unprotected graphite.

#### 5.1.1 Unprotected Graphite Oxidation

Graphite consists of mostly carbon with some trace amounts of unknown impurities. At high temperatures, the solid carbon reacts with oxygen in the ambient air to form carbon dioxide gas or carbon monoxide gas, depending on the completion of the reaction. As the reaction progresses, solid carbon in the graphite is lost to form carbon dioxide. Therefore, the mass of the graphite will decrease. The rate at which this oxidation occurs depends on several factors including temperature, pressure, geometry, porosity, impurities, degree of graphitization and so on. Since the graphite provided by the manufacturer had no specifications other than that one was higher grade with small low porosity and one was lower grade with higher porosity, the only factor that could be controlled or known was temperature. The figures 5.1 and 5.2 summarize the experiment without the coating.

The graphite samples, which measured 5x5x5 cm were placed into a *Fisher Scientific Isotemp* furnace and heated to the desired temperature. The high and low grade samples' mass were 226.76 g and 201.69 g respectively. The cold samples were placed into the cold furnace to allow the samples to gradually heat at thermal quasi equilibrium with the furnace and to allow for any

moisture to evaporate. Once the desired temperature was reached and thermal equilibrium established, the samples were removed from the furnace and weighed on a scale. The samples were then replaced into the furnace. The weighing process was repeated at regular time intervals.

Although the furnace did impede gas flow, it is not a sealed environment therefore gases can enter or exit during operation. However, it did not have an active ventilation system. Any flow or circulation of gases was due to natural convection. Every time the door was opened to measure the weight, the gases inside were restored to mostly air. Measuring the actual composition of the gas within the furnace was not possible with the available instrumentation.

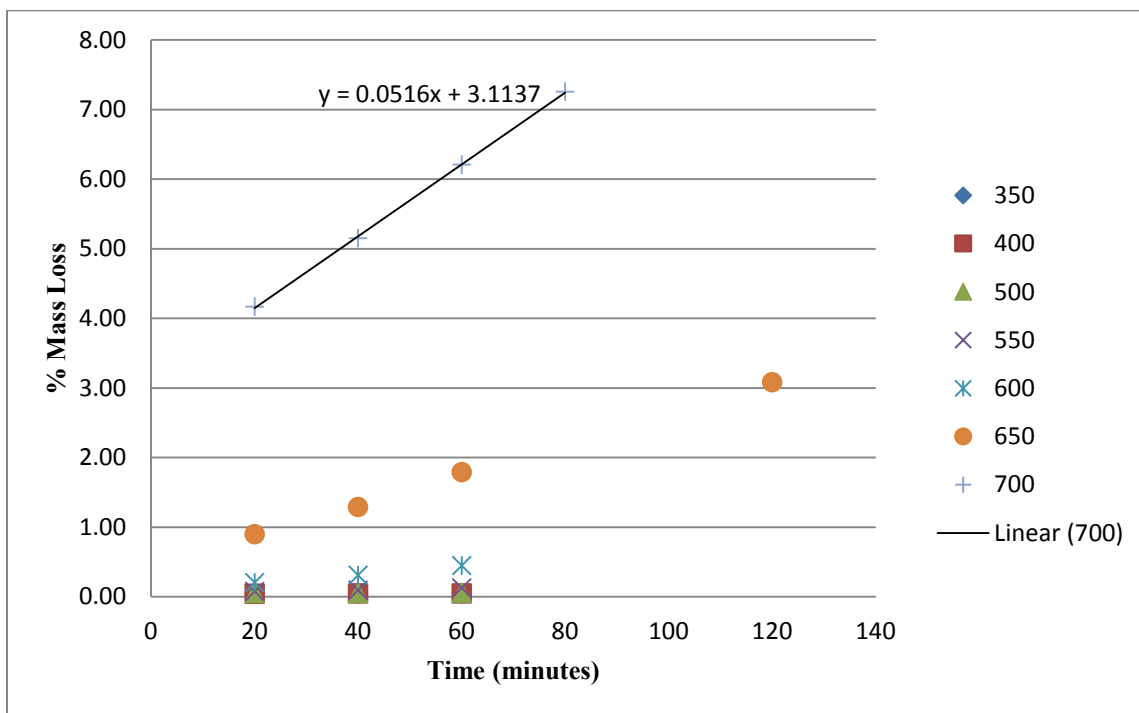


**Figure 5.1: Sample 1 oxidation rate of lower grade graphite with no coating at several temperatures**

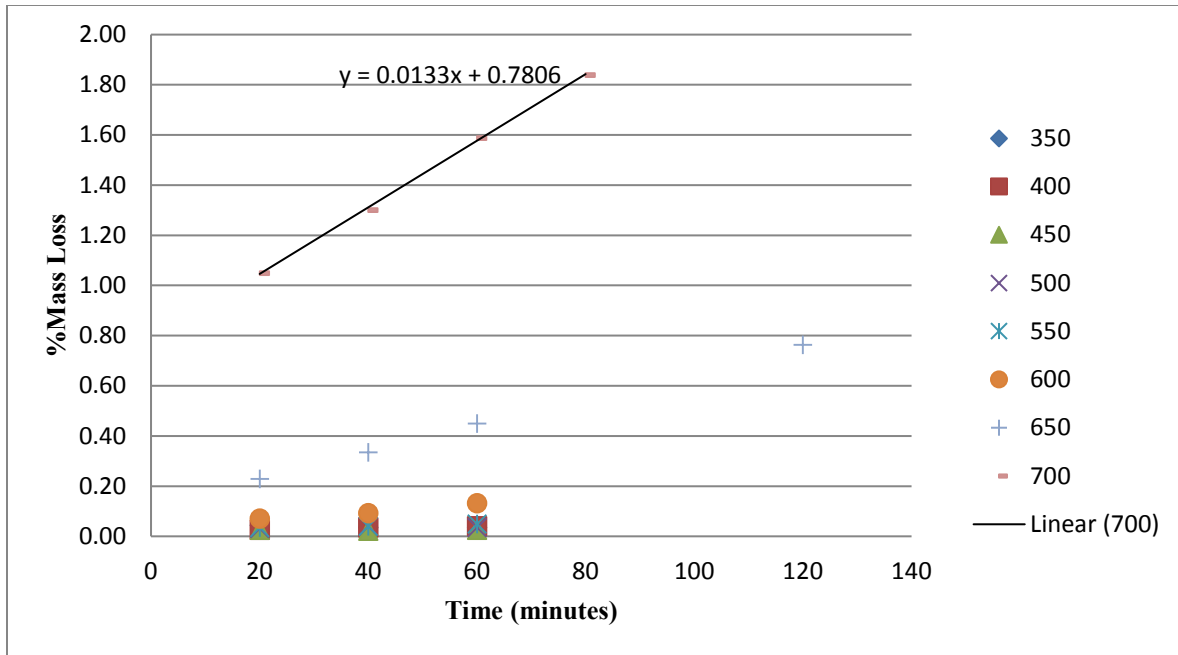


**Figure 5.2: Sample 2 oxidation rate of higher grade graphite with no coating at several temperatures**

According to these results, significant oxidation only begins at temperatures above 550 °C. The slope of the line for the 700 °C test indicates that the graphite loses mass at 0.052 %/minute and 0.013 %/minute for the lower grade and the higher grade respectively. The lower grade graphite oxidized 4 times faster than the higher grade graphite. Assuming these rates remain constant for all time, than the graphite will be completely lost after 32 hours and 128 hours of exposure to a 700 °C environment, respectively. The considerable difference between these two oxidation rates can only be caused by the quality and porosity of the graphite, since all other factors were the same for both samples.

### 5.1.2 Single Coat of SiC Based Coating

Figure 5.3 shows the results of the oxidation test with 1 coat of the *Aremco* anti-oxidation coating. The coating acts as a physical barrier between oxygen and carbon to prevent the reaction

from taking place. The test was done at 700 °C only, since it is the highest operation temperature of the thermal storage. The graphite samples that were used for this test were the same as for the test with no coating. This means that the graphite was already oxidized before applying the coat. The fact that these samples were pre-oxidized has an appreciable effect on the validity of the comparison between coated samples and non-coated samples. Results from subsequent tests show that oxidation rate is not constant but that it increases as the oxidation progresses. These results will be shown in subsequent sections. However, for a relatively short oxidation time of 60 minutes, the non-linearity can be ignored while maintaining a meaningful comparison.

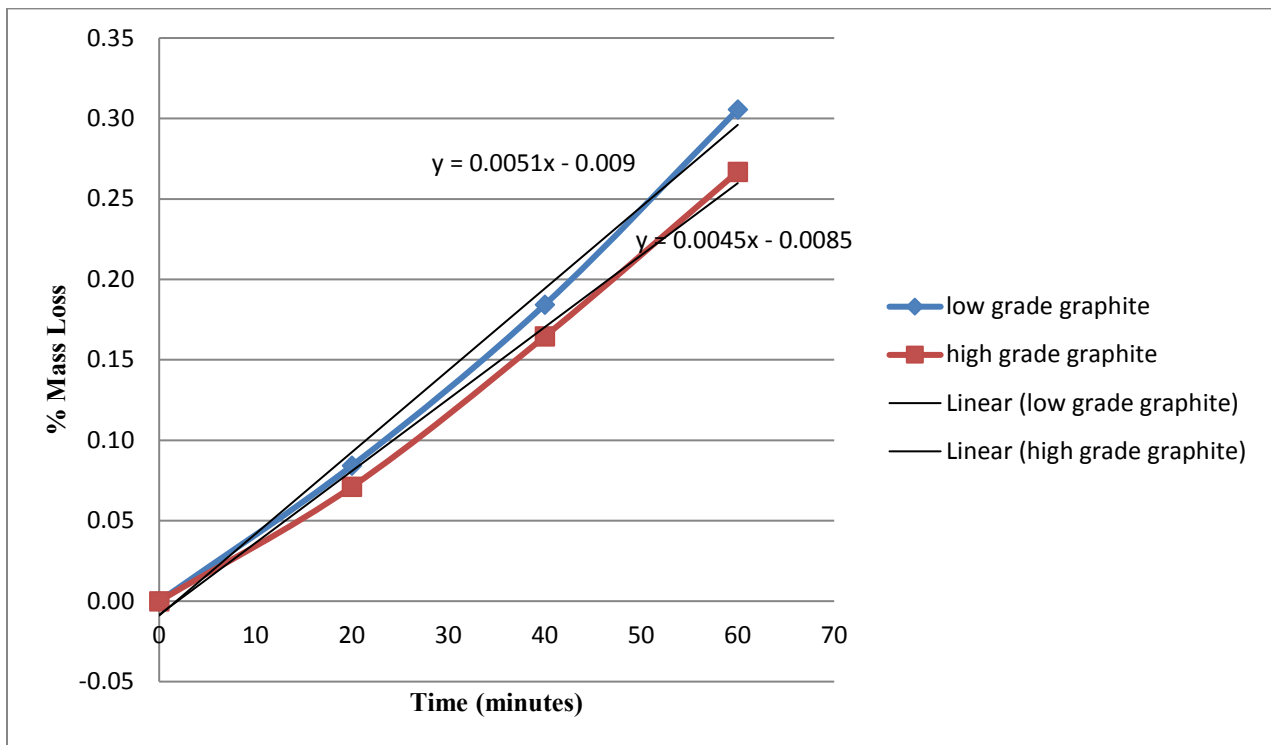


**Figure 5.3: Oxidation rate with Aremco anti-oxidation coating at 700°C (pre-oxidized, 1 coat)**

### 5.1.3 Double Coat of SiC Based Coating

A third test was conducted on new, unoxidized graphite samples with two coats of the *Aremco* anti-oxidation coating. Figure 5.4 summarizes the results.

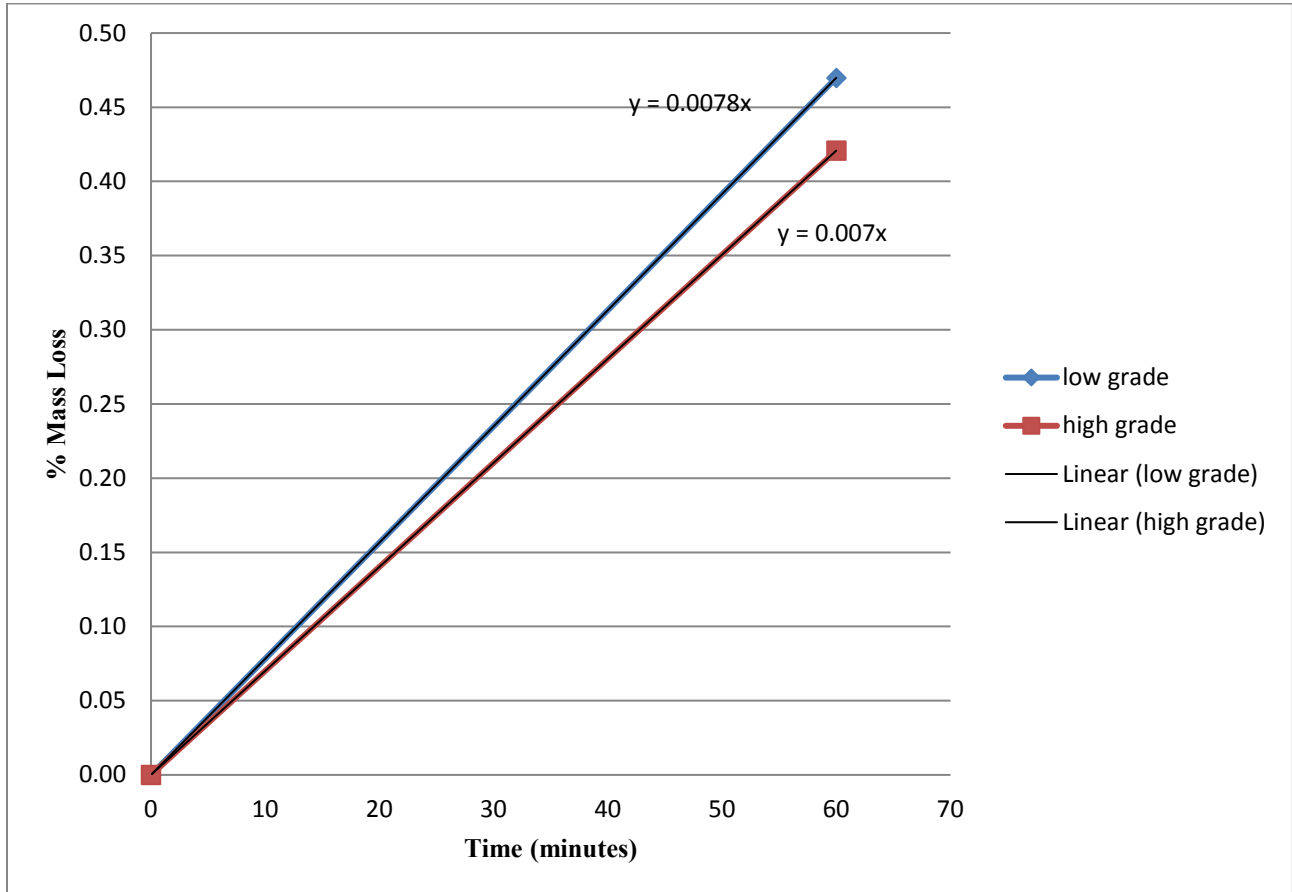


**Figure 5.4: Oxidation rate with Aremco anti-oxidation coating at 700°C (unoxidized samples, 2 coats)**

Again, assuming the oxidation rate is constant for all time, the lower grade and the higher grade graphite will be entirely lost after 333 hours and 370 hours respectively. Table 5.1 is a summary of the oxidation rates and lifespans of both graphite qualities, with and without the coating, all at 700 °C.

**Table 5.1: Oxidation rates and lifespan for various conditions**

<b>700°C</b>	<b>oxidation rate (%mass loss / minute)</b>	<b>oxidation rate (g/min)</b>
<b>Lower grade, without coating</b>	0.052	0.1000
<b>Higher grade, without coating</b>	0.013	0.0290
<b>Lower grade, with 1 coat Aremco coating (pre-oxidized)</b>	0.0051	0.0097
<b>Higher grade, with 1 coat Aremco coating (pre-oxidized)</b>	0.0045	0.0101
<b>Lower grade, with 2 coats Aremco coating (fresh samples)</b>	0.0078	0.0161
<b>Higher grade, with 2 coats Aremco coating (fresh samples)</b>	0.007	0.0160

It is important to note that the values in table 5.1 were determined from 5x5x5 cm cubes of graphite and that they will not be the same for the actual thermal storage block. The actual storage block will not be cubic either. The surface area of the samples is 150cm<sup>2</sup> and the surface area of the actual storage block is 12800 cm<sup>2</sup>. The mass of the high grade sample is 226.7 g while the mass of the actual storage block is 147 kg, assuming it will have the same density. Assuming that the oxidation rate, in g/min, is proportional to surface area, then the oxidation rate for the actual storage block can be found by multiplying the rate for the samples by the ratio of area, which is 12800/150. Tables 5.2 and 5.3 show these oxidation rates and the associated lifespan, respectively.

**Table 5.2: Expected oxidation rates for the actual storage block (constant rate)**

<b>700°C actual storage block</b>	<b>oxidation rate (%mass loss / minute)</b>	<b>oxidation rate (g/min)</b>
<b>Lower grade, without coating</b>	0.00648	8.500
<b>Higher grade, without coating</b>	0.00168	2.470
<b>Lower grade, with 1 coat Aremco coating (pre-oxidized)</b>	0.000631	0.827
<b>Higher grade, with 1 coat Aremco coating (pre-oxidized)</b>	0.000586	0.862
<b>Lower grade, with 2 coats Aremco coating (fresh samples)</b>	0.00105	1.374
<b>Higher grade, with 2 coats Aremco coating (fresh samples)</b>	0.000929	1.365

**Table 5.3: Expected lifespan of actual storage block (constant rate)**

<b>700°C actual storage block</b>	<b>Lifespan (hr)</b>	<b>Effective Lifespan (hr)</b>
<b>Lower grade, without coating</b>	257	51
<b>Higher grade, without coating</b>	992	198
<b>Lower grade, with 1 coat Aremco coating (pre-oxidized)</b>	2641	528
<b>Higher grade, with 1 coat Aremco coating (pre-oxidized)</b>	2844	569
<b>Lower grade, with 2 coats Aremco coating (fresh samples)</b>	1587	317
<b>Higher grade, with 2 coats Aremco coating (fresh samples)</b>	1794	359

It is interesting to note that the oxidation rate with two coats was greater than that with one coat. This result is unexpected and can only be attributed to inconsistent graphite quality provided by the manufacturer. These values may seem low, but these values are from oxidation at 700 °C, which is the maximum expected temperature. The temperature of the graphite is expected to vary between 350 °C and 700 °C. It will only be at 700 °C for approximately 3 hours per day. Also, the lifespan in figure 5.3 is the time it would take for the entire mass of graphite to oxidize. The storage block will become inadequate long before that. After a certain amount of oxidation, the storage block will have lost mass and will eventually be in need of replacing. It is convenient to know an effective lifespan, which we will define as the time needed to lose 20% of the mass.

So far the oxidation rate has been assumed constant. That is, the relationship between time and percent of mass loss has been assumed to be linear. Figure 5.5 shows the results of a test conducted over 6 hours as opposed to 1 hour in order to assess the validity of the assumption. This test was done on samples that had already been oxidized.

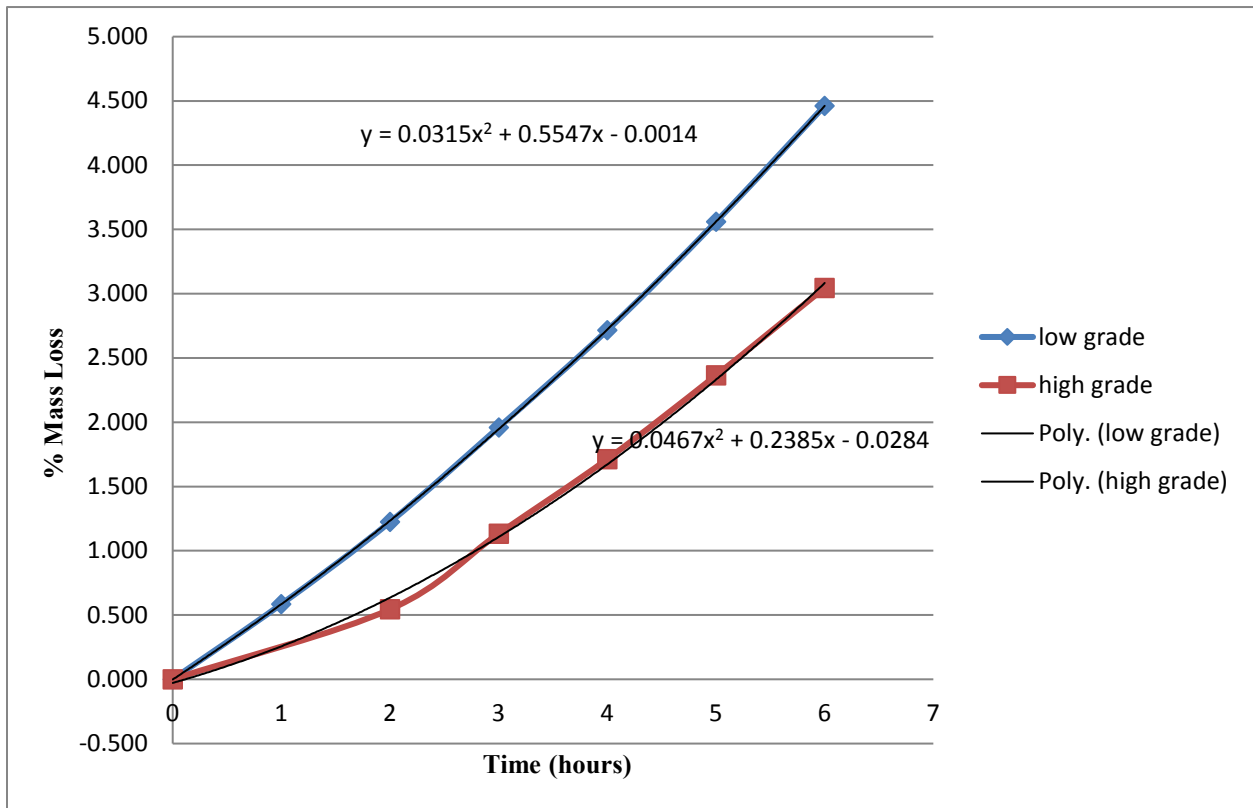


**Figure 5.5: Oxidation rate over prolonged heat exposure with 2 coats of Aremco coating at 700°C**

Figure 5.5 suggests that the rate is not constant, but increases with time according to the approximated curve fitting equations. Multiplying the variable rate of oxidation by the surface area ratio, we can predict the oxidation rate of the actual storage block and its lifespan. Using this model the expected lifespans are summarized in table 5.4.

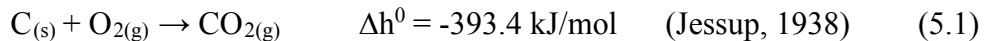
**Table 5.4: Expected lifespan of the actual storage block (variable rate)**

<b>700<sup>0</sup>C with <i>Aremco</i> coating</b>		<b>lifespan (hr)</b>	<b>effective lifespan (hr)</b>
	<b>low grade 2 coats</b>	155	65
	<b>high grade 2 coats</b>	125	55

Taking into account the variable oxidation rate, we can see by comparing tables 5.3 and 5.4 that the effective lifespan is greatly reduced. Predicting these values were obtained by up-scaling the results of the tests done on small samples to the actual storage block, based on the assumption that the oxidation rate is only dependent on the surface area. While this assumption seems logical and reasonable, the reality is most likely more complex. Conducting these same tests on the full-sized storage blocks is the only way to determine with accuracy the effective lifespan. For the design purposes, these predicted values provide enough insight to suggest a design direction.

#### **5.1.4 Heat of Combustion**

Combustion is essentially oxidation at a high rate. The combustion of graphite occurs according to the following reaction.



The reaction is exothermic. This implies that as the graphite storage block oxidizes and loses its capacity for heat storage, it also produces heat. These two processes have opposing effects but happen simultaneously. The graphite acts like a fuel and produces useful heat. It is practical to

know the amount of useful heat over the effective lifespan of the graphite storage block. Taking the best effective lifespan in table 5.3, the total heat produced by combustion of the 147kg block over 569 hours at 700 °C is

$$Q = (0.20) * (147000g) / (12.01g/mol) * (393.4kJ/mol) / (3600kWh/kJ) = 267.5 kWh \quad (5.2)$$

If we take the best effective lifespan in table 5.3 of 569 hours, and assume that the storage will be at 700 °C for 3 hours per day, then the storage block would need to be replaced after

$$(569 \text{ hr}) / (3 \text{ hr/day}) = 190 \text{ days} \quad (5.3)$$

The amount of heat of combustion produced per day would be

$$Q = (267.5 \text{ kWh}) / (190 \text{ days}) = 1.4 \text{ kWh/day} \quad (5.4)$$

The graphite block is designed to store 25 kWh/day, so the total heat available to the engine, from storage and combustion is

$$25 \text{ kWh/day} + 1.4 \text{ kWh/day} = 26.4 \text{ kWh/day} \quad (5.5)$$

and the percentage of that heat, coming from combustion alone is

$$100*(1.4 / 26.4) = 5.3\% \quad (5.6)$$

Again, the above analysis considers only oxidation at 700 °C. Also, the percentage of heat from combustion is an average value. It will increase along with the oxidation rate. The mechanics of the process are overly simplified here. Nonetheless, they provide some insight.

It is interesting to note that the oxidation rates of the lower and higher grades were nearly the same with the coating, whereas without the coating, the lower grade oxidized 4 times faster than the higher grade. This suggests that, with the coating, dominant factor was the amount of oxygen diffusing through the coating. Since the coating was the same on both samples, the available oxygen was the same and the oxidation rates were also nearly the same.

On the pre-oxidized samples, the addition of the coating increased the lifespan by a factor of 10.4 for the lower grade graphite and by a factor of 2.9 for the higher grade graphite. It is important to note that these tests were done on 200g samples of graphite but the actual thermal storage graphite block will be 147 kg.

Contrary to expected results, the oxidation rates increased by 53% for the low grade graphite and 55% for the high grade graphite when the test was done with 2 coats on un-oxidized samples compared to 1 coat with pre-oxidized samples. The cause of this remains unknown, but to speculate, the ash of impurities in the graphite may form a protective barrier on the surface, effectively blocking contact between the graphite and the oxygen. The pre-oxidized samples, having already oxidized and accumulated a layer of ash, may be less susceptible to further

oxidation. A more likely explanation is that the consistency of the graphite quality provided by the manufacturer is variable.

The method of application of the coating was, in both cases, done with a paint brush by hand. This introduces some unaccountable variation in the thickness of the coats.

The prolonged exposure test did show that the oxidation rate was not constant but that it increases with time. This eliminates the possibility of a protective ash barrier slowing the oxidation. The accuracy of the measurements for this test, and all subsequent conclusions, are limited.

These tests were conducted at 700 °C. Significant oxidation occurs at around 600 °C. It is difficult to account for the oxidation rates at different temperatures, for non-uniform temperature distribution within the block and for reduced surface area as oxidation progresses. However, if we take the best effective lifespan in table 5.3 of 569 hours, and assume that the storage will be at 700 °C for 3 hours per day, then the storage block would need to be replaced after

$$(569 \text{ hr}) / (3 \text{ hr/day}) = 190 \text{ days} \quad (5.7)$$

However, if we adopt the variable oxidation rate model, then it would need to be replaced after

$$(65 \text{ hr}) / (3 \text{ hr/day}) = 22 \text{ days} \quad (5.8)$$

This value neglects the oxidation at temperatures below 700 °C. Taking it into account would reduce the number of days. However, the reduced surface area as oxidation progresses was also

not taken into account. This would have an effect of increasing the number of days. Therefore, 190 days is a rough estimate. Regardless, 190 days is much too short as an effective lifespan for a cost-effective heat storage. Thus, oxidation protection using the silicon carbide based coating by *Aremco* is inadequate. Some other coating or another method entirely must be implemented to increase the effective lifespan.

## **5.2 Aluminum Oxide Based Anti-Oxidation Coating**

### **5.2.1 Double Coat of Al<sub>2</sub>O<sub>3</sub> Based Coating**

Having determined that the silicon carbide based coating was inadequate, some testing was done using an aluminum oxide based anti-oxidation coating. The procedure was the same in that the sample was placed in the same furnace at 700 °C and its mass was measured at certain times of exposure to heat. This coating was also applied by hand using a paintbrush. In order to compare the silicon carbide based coating to the aluminum oxide based coating, the test conducted was identical to the test which generated the data shown in figure 5.5. Two coats of aluminum oxide anti-oxidation coating, supplied by *Aepco*, was applied by paintbrush. The proper curing procedure was followed, as specified by the supplier. The samples were then placed in a cold furnace as it heated up to 700 °C. Once the desired temperature was reached, the samples were weighed at that moment and at every consecutive hour for six hours. The low grade and high grade graphite samples weighed 211.13 g and 228.99 g respectively after the application and curing of the coating. After reaching 700 °C, they weighed 210.65g and 228.69 g respectively. This mass loss that occurs during the heat up process is attributed to moisture contained within the graphite. Thus, the reference time and mass is taken after the heat up process when the samples have just reached 700 °C and all moisture is removed. This test produced the results shown in figure 5.6.

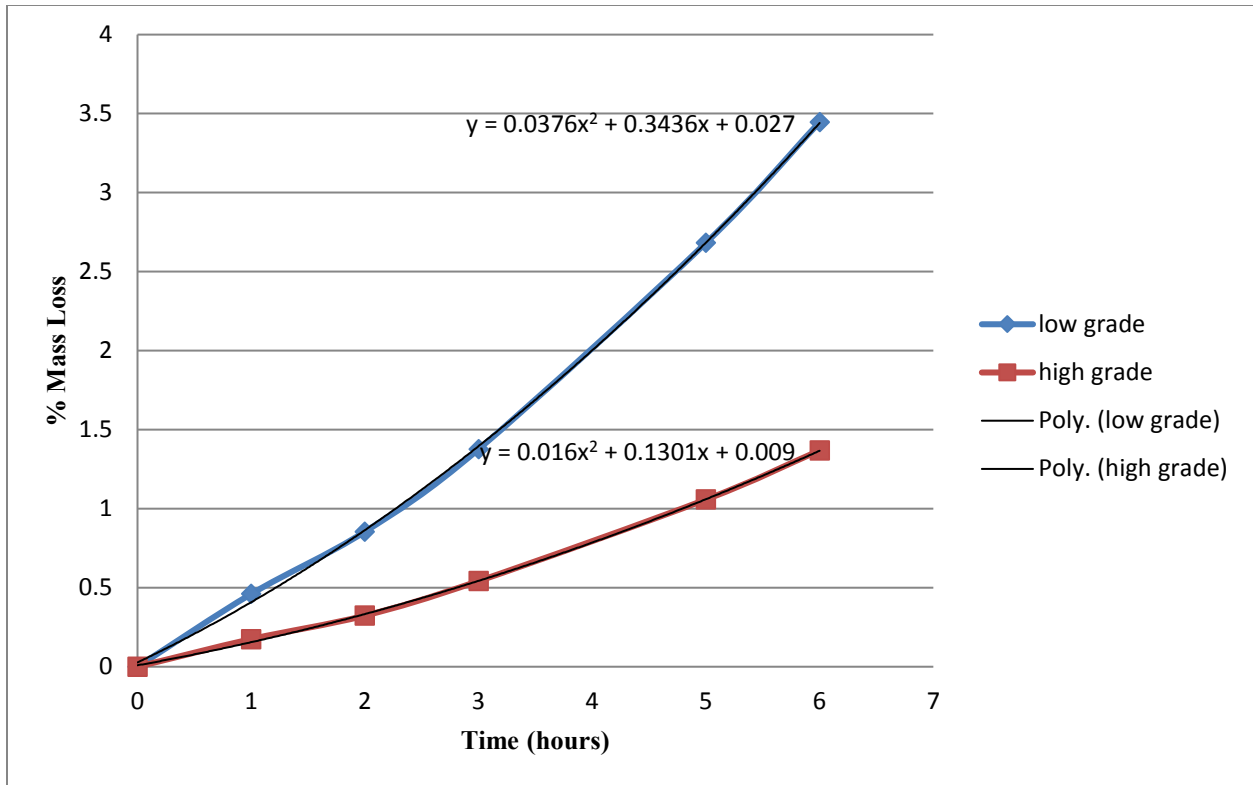


**Figure 5.6: Oxidation rates of graphite with two coats of Aepco aluminum oxide based anti-oxidation coating at 700°C**

Plotting the data from figure 5.5 and figure 5.6 together in figure 5.7, we can compare the effectiveness of the *Aremco* and *Aepco* coatings since the tests were done in exactly the same manner.

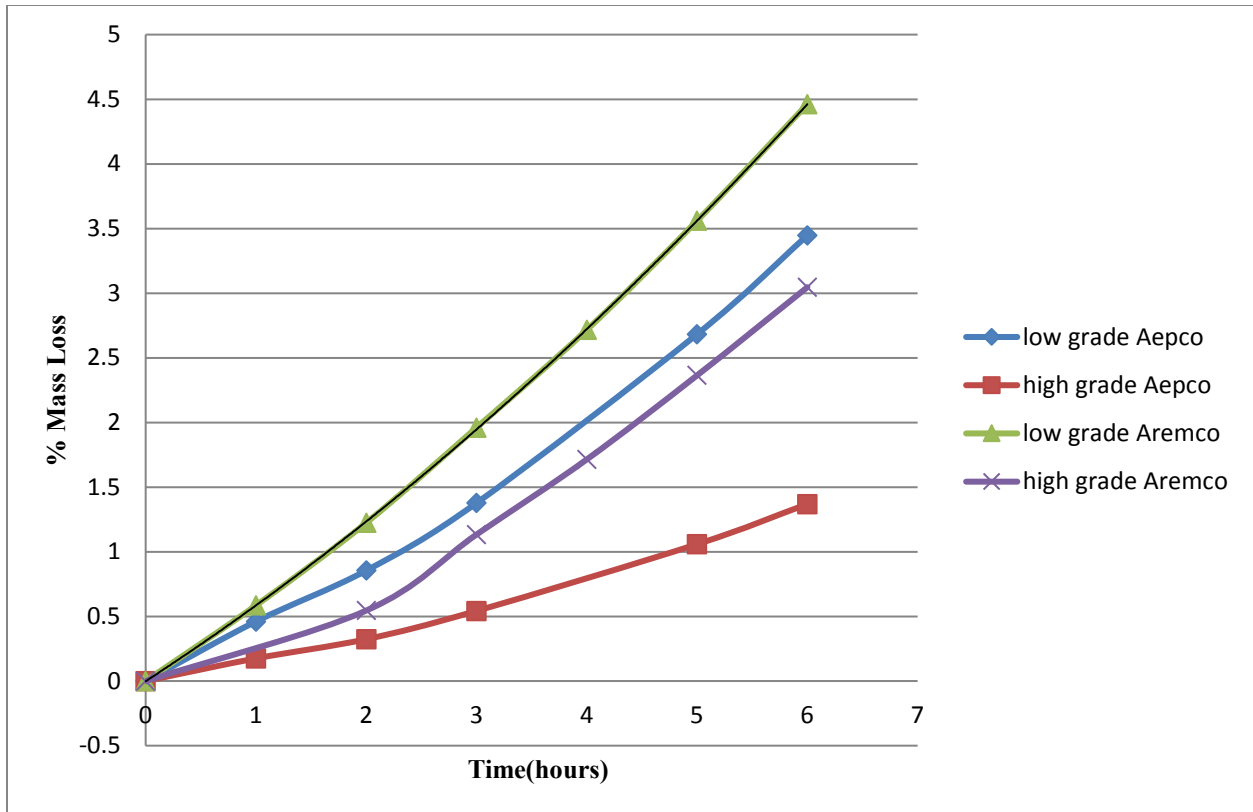


**Figure 5.7: Comparison of the effectiveness of two coats of *Aremco* (SiC) to two coats of *Aepco* (Al<sub>2</sub>O<sub>3</sub>) anti-oxidation coatings at 700°C.**

Examining figure 5.7, it is clear that the aluminum oxide based coating is more effective than the silicon carbide based coating. For the high grade of graphite, the sample with the aluminum oxide based coating oxidized 55% less than the one with the silicon carbide based coating after six hours. For the low grade graphite, the sample with the aluminum oxide based coating oxidized 23% less than the one with the silicon carbide based coating after six hours. Since the oxidation rates are not constant, these differences would increase as time progresses beyond 6 hours. Thus, the *Aepco* coating is significantly better. The lifespan and effective lifespan of the

actual storage block of graphite, shown in table 5.5, was calculated in the same way as described for the *Aremco* coating.

**Table 5.5: Lifespan and effective lifespan of the actual heat storage block of graphite**

700 <sup>0</sup> C with <i>Aepco</i> coating	lifespan (hr)	effective lifespan (hr)
low grade 2 coats	143	62
high grade 2 coats	213	93

These lifespans are an improvement from those obtained using the *Aremco* coating, but they are still much too low for a cost-effective heat storage.

### 5.2.2 Prolonged Heat Exposure

The tests that generated the data in figure 5.7 were conducted over one period of six hours. This implies that there was no cooling and reheating within this period. Although the tests were useful for determining the mass loss as a function of time for a given temperature, they do not realistically replicate conditions of the actual heat storage for two main reasons.

Firstly, the actual heat storage will operate much longer than 6 hours. There may be some discontinuity in the oxidation function that occurs beyond 6 hours. Second, the actual storage will have heating and cooling cycles which was not imposed on the previous test samples. Therefore, the effect of thermal fatigue was not evaluated.

To provide some insight on the effects of prolonged heat exposure and thermal fatigue, another oxidation test was conducted to include exposure time and the number of exposures. Figure 5.8 presents the results. Note that each time interval between data points is one heat exposure period

at 700 °C. The time of cooling and reheating is not included in the figure. Before entering a new data point, the sample was cooled to room temperature by natural convection and then reheated to 700 °C.

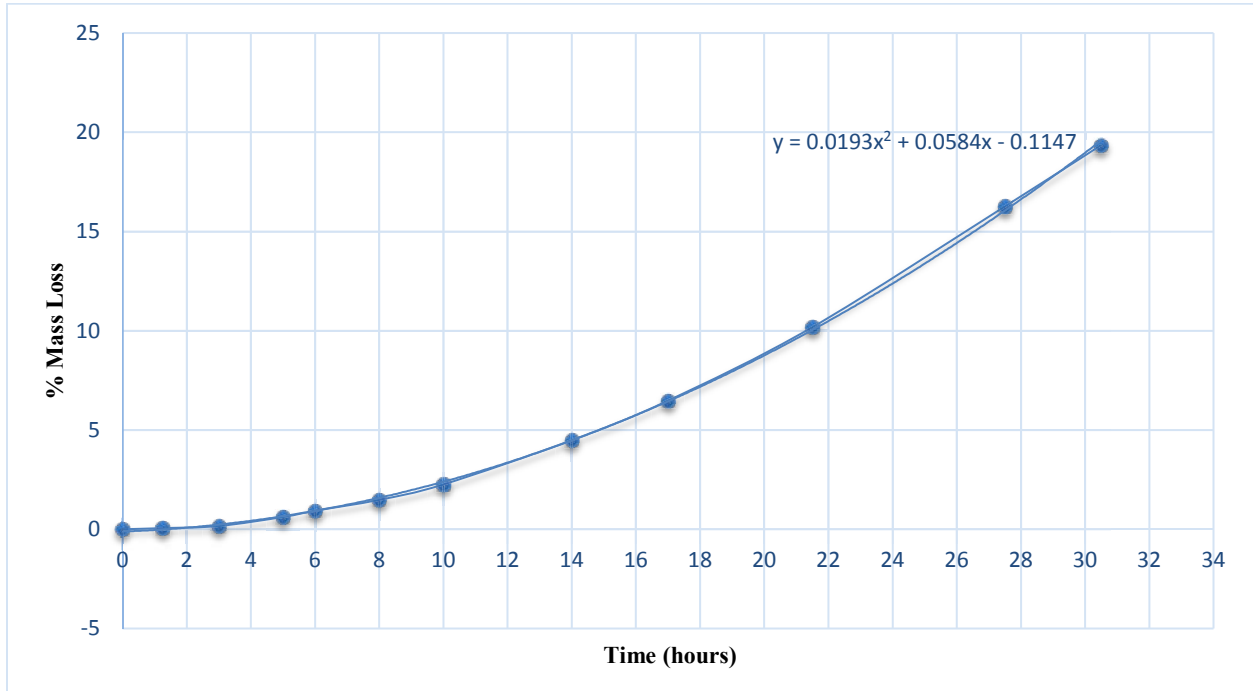


**Figure 5.8: Graphite (high grade) oxidation rate at 700°C with 1 coat of Aepco (Al<sub>2</sub>O<sub>3</sub>) anti-oxidation coating with heating and cooling cycles**

The curve is very similar to the curve representing the high grade graphite found in figure 5.7. The rate was slightly higher for this test but that is to be expected due to the lack of a second coat of anti-oxidation coating. This similarity suggests that heating and cooling cycles do not affect the oxidation rate. The function remains continuous up to 30.5 hours. However, during the final cooling, the Al<sub>2</sub>O<sub>3</sub> coating began to crack and fall off leaving the graphite underneath

completely exposed to oxygen. The protective coating thus completely fails after 30.5 hours of heat exposure at 700 °C.

The exposed graphite that was directly beneath the coating had turned to a fine powder due to excessive oxidation. This is the most probable cause for the coating to crack; the solid graphite surface to which that coating had originally adhered to had turned to powder and was unable to support the layer of coating. The very thin and brittle Al<sub>2</sub>O<sub>3</sub> coating was no longer supported by a solid graphite surface and cracked off with the slightest manipulation.

This prolonged exposure test was not conducted with the *Aremco* SiC coating. However, since this coating is equally thin and brittle, cracking and peeling should be expected to occur with this coating as well. A plausible solution to this cracking problem would be to apply an excessive amount of coats such that it would be thick enough to support itself. However, this would severely reduce the ability of the graphite to release its heat during discharging. The anti-oxidation coating would effectively act as permanent insulator. It should be noted that, regardless of the type of coating or the size of the block of graphite, this cracking should be expected to occur at 30.5 hours since it is related to the thickness of the powdered graphite layer. Beyond a certain thickness of graphite powder, the coating will crack and this thickness is independent of the size of the block.

It seems that any anti-oxidation coating that can withstand 700 °C is not a viable option to protect graphite as a heat storage for two main reasons. The protection it offers, for a reasonable number of coats, is inadequate as found by the low effective lifespan of 93 hours. Also, cracking will inevitably occur before reaching the effective lifespan.

### **5.3 Inert Gas Blanketing**

In this section, the possibility of enveloping the graphite in an inert gas as a means to prevent oxidation is evaluated. The mechanism of protection from oxidation is similar to that of coatings in that a layer of inert gas acts as a barrier between the graphite and the oxygen in the ambient air. Figure 5.9 is a schematic representation of the experimental setup used to test this method of oxidation protection. The aluminum box was sealed and airtight with the exception of the gas supply hose and the gas escape orifice. The experimental procedure is as follows. The uncoated high grade graphite sample with a hole drilled through its center was weighed and put in the sealed box. The inert gas was then allowed to flow into the sealed aluminum box from the supply hose and out through the escape orifice for ten minutes to flush out all gases with the exception of the inert gas. At this point, the inert gas was the only gas present in the box. The heater, which was previously inserted into the graphite, was then supplied power. The power supply was tuned to maintain a steady state temperature of 700 °C. The gas flow rate was then reduced just enough to ensure that no air could enter through the escape orifice due to constant outflow of the inert gas. This temperature and flow were maintained for 4 hours. The power was then cut and the graphite sample was removed and weighed immediately while still hot to minimize the oxidation time during the weighing. This test was conducted twice; once using carbon dioxide as the inert gas and another using argon.

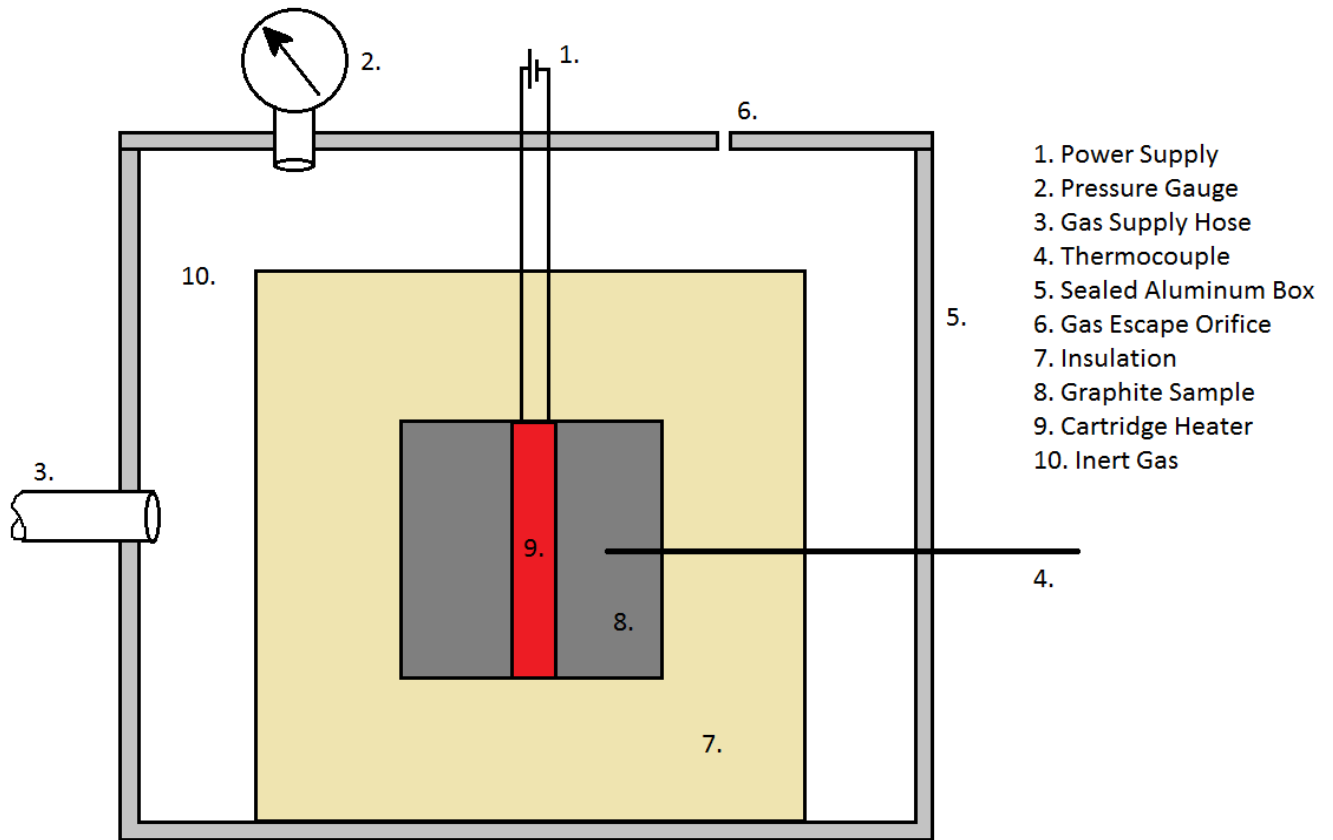


**Figure 5.9: Schematic of inert gas blanketing oxidation test**

A third test, using the same experimental setup, was conducted to evaluate the effectiveness of a vacuum to prevent oxidation. In this case, the gas supply hose was connected to a vacuum pump and the gas escape orifice was sealed.

**Table 5.6: Effective lifespans of the test sample and of the actual storage block using inert gas blanketing**

inert gas	time (hr)	temperature (°C)	initial mass (g)	final mass (g)	% mass loss	effective lifespan (hr)	
						sample	actual
CO <sub>2</sub>	4	700	220.32	220.27	0.023	3478	27562
Ar	4	700	220.38	220.34	0.018	4444	34454
vacuum	4	700	220.235	215.89	1.97	41	317

The effective lifespan of the inert gas blanketing is clearly much longer than those obtained using a protective coating. Assuming that the storage block will be at 700 °C for 3 hours per day, it would only need replacing every 31 years. However, the effective lifespan obtained for the vacuum is still inadequately low. Theoretically, all three of these methods should be 100% effective to prevent oxidation. Essentially, if there is no oxygen present in the box, then the graphite cannot oxidize and all three of these methods accomplish this ideally. That is to say that all three methods should yield an indefinitely long lifespan. These ideal conditions are hardly possible. The intent of these tests was mostly to evaluate the feasibility of reaching these ideal conditions.

For the argon and carbon dioxide tests, it should be noted that some large fraction, perhaps all, of the mass loss is due to moisture adsorbed by the graphite. At room temperature, the graphite adsorbs some moisture from the air. When it is heated, the moisture is vaporized resulting in an abrupt mass loss that is not attributed to graphite oxidation. Since there was no available way of quantifying this fraction, it was assumed to be entirely from oxidation. Even though this assumption is not reasonable, it is very conservative.

For the vacuum test, the same issue of unknown moisture loss was present. Similarly, the effective lifespan should be much longer. However, this does not explain the drastic differences in effective lifespans between inert gas blanketing and vacuum methods. The difference in effective lifespans was due to not obtaining an absolute vacuum. The gauge pressure inside the sealed box during the test was -12.4 psi (-85.5 kPa) corresponding to an absolute pressure of 2.3 psi (15.9 kPa). As a result, a significant amount of oxygen remained inside the box during the heating. With more sophisticated equipment, the pressure could be lowered resulting in less oxygen available for reaction and in turn resulting in a longer effective lifespan.

## **Chapter 6: Charging and Discharging Performance**

This chapter addresses the performance of a sensible heat storage design using graphite as the heat storage material. The performance is characterized by the charging and discharging rates as well as the charging and discharging efficiencies. These terms will be defined in subsequent sections. Sensible heat storage designs can vary but all designs will require a heat storage material, some insulation and a mechanism for heat flux in and out. The tests conducted evaluate the performance for the general design of a graphite based sensible heat storage with the heat transfer mechanism being conduction. Naturally, the performance will depend on much more factors than these. A test method was developed to account for all these factors while remaining generalized in its results and applicable to other designs. In this sense, the results are valid for other designs in which certain parameters differ from those of the test. This was accomplished by means of a dimensionless number.

Under intended operating conditions, the graphite TES will be heated by concentrated solar radiation and will be cooled by a cast iron engine head. The temperature distribution within the graphite and the heat flux in and out will depend on many factors. Some of the factors are constant and others are variable. The variable factors include time of day, season, cloud cover and electricity demand. The constant factors are the absorptivity of the graphite, the thermal conductivity of the graphite, the thermal conductivity of the insulation, the transmissivity of the glass, the thermal conductivity of the engine head and the convective heat transfer coefficient of the heat transfer fluid (helium) within the engine head. The solar irradiance cannot be replicated in the laboratory, therefore it must be substituted by an equivalent conductive heat flux.

Under operating conditions, the graphite will absorb heat by solar irradiance. The sun's rays will be reflected off the mirrors and then transmitted through the glass. The reflection and

transmission will cause some losses resulting in a reduced irradiance at the surface of the graphite. The amount of heat that is absorbed from this reduced radiation will depend on the absorptivity of the graphite. This heat flux must be calculated and then replicated by an equivalent conductive heat flux from a hot plate.

Most importantly, the question of whether or not the actual storage block will be able to provide enough power to the engine to make it run must be answered. This question will be answered by testing a scale model of the storage block. For the actual storage block, the outward heat flux will depend on many factors. It is a function of the initial temperature of the block  $T_0$ , the time of contact  $t$  between the engine and the storage, the thermal conductivity of the engine head  $k_e$  and of the graphite  $k_g$ , characteristic length of the block the  $x$ , the mass  $m$ , the contact area  $A_c$  and the heat transfer fluid contact area  $A_i$  inside the engine head and the heat transfer coefficient  $h$ .

$$\dot{Q} = f(T_0, t, k_e, k_g, x, m, A_c, A_i, h) \quad (6.1)$$

$$x = (\text{volume of block})^{1/3} \quad (6.2)$$

It is thus a very complex process. These variables were combined to form dimensionless quantities so that the scale of the test model has no importance. This will also reduce the amount of variables. However, the variable  $k_g$  will be the same for the test model as for the actual storage block so it can be eliminated so that

$$\dot{Q} = f(T_0, t, k_e, x, m, A_c, A_i, h) \quad (6.3)$$

The power provided by the test block will be much less than the actual block. Thus, in order to make the test valid regardless of scale, the specific power, or the power per unit mass will be plotted as a function of time  $t$ , initial temperature  $T_0$ , and one dimensionless number  $\Pi$ .

$$\frac{\dot{Q}}{m} = f(T_0, t, \Pi) \quad (6.4)$$

$$\Pi = \frac{xhA_i}{k_eA_c} \quad (6.5)$$

In the relationship above, all eight variables are taken into account. The function that relates these variables should be the same regardless of the scale of the test. Therefore, the results of the scale model test should apply to the actual storage block. However, the test sample will not be an exact scaled replica of the actual storage block. The shape will be slightly different so this test will have some error due to this.

This model is thus valid for any graphite based sensible heat storage shaped as a rectangular prism in which the outward heat flux is accomplished by contact with another mass in which a heat transfer fluid flows.

Testing of thermal properties and performance was done with a multipurpose test rig shown in figure 6.1. The test rig was designed to resemble a scaled down model of the actual heat storage prototype. In this way, the performance of the prototype can be simulated by evaluating the performance of the test rig. It was also designed to measure thermal conductivity for the graphite samples placed inside.

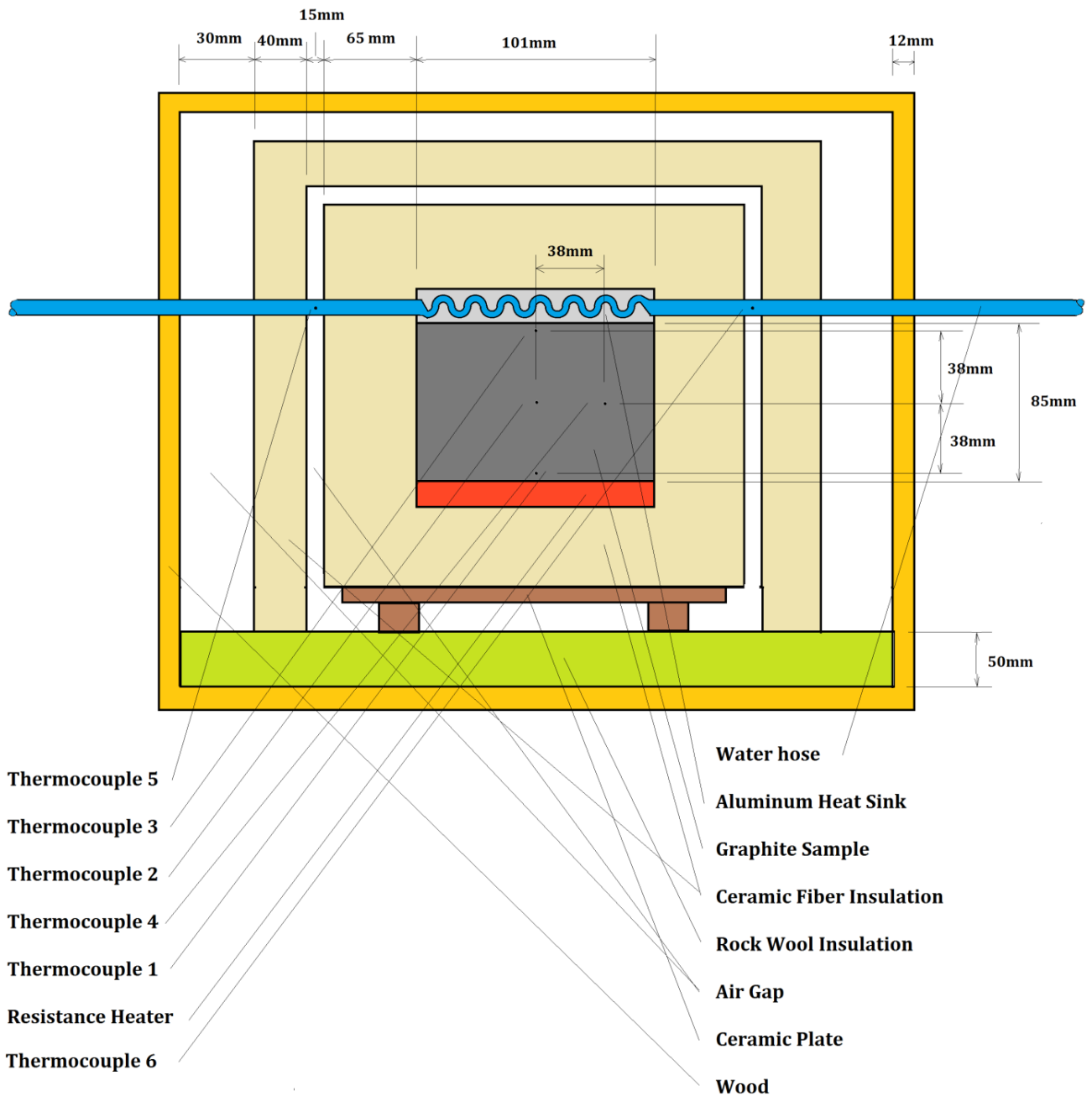


**Figure 6.1: Multipurpose test rig setup**

The sample inside is expected to reach temperatures above 700 °C so the insulation used must withstand these high temperatures. Unfortunately, high temperature resistance most often correlates with relatively high thermal conductivity for insulation. To minimize heat losses, several layers were used with air gaps in between. The wooden box has little insulation value but adds an additional air gap to reduce convective heat losses to the ambient air. The graphite sample is heated on one side with an electrical resistance heater. The opposite side is cooled with a water cooled aluminum heat sink. Four orifices of 1.59 mm diameter were created, all 38 mm apart into which were inserted thermocouples so that the temperature, at different locations could be monitored. The hose that provides water to the heat sink had 2 holes for thermocouples – one for water inlet temperature and one for water outlet temperature.

### **6.1 Discharge Power**

The test was initiated without the heat sink and hoses. The graphite was heated from room temperature by the resistance heater until 500 °C was reached at  $T_1$ . The heat flux provided by the heater was set to 534 W and the mass of the graphite block was 1.57 kg for the high grade sample and 1.40 kg for the low grade sample. Once 500 °C was reached, the power to the heaters was cut, the heat sink was placed onto the graphite sample and water was allowed to flow through it. At every 1 minute interval all six temperatures were recorded as well as the flow rate of the water. This process simulates the discharging by the engine head. This data was recorded until the temperature  $T_1$  reached below 40 °C.

All parameters needed to calculate the dimensionless  $IT$  number are known with the exception of  $h$  and  $A_i$ . These parameters depend on the geometry of the heat sink flow channels. Firstly,  $A_i$  is the area of the flow channel walls inside the heat sink. The heat sink used had a rectangular cross

section flow channel with width and height of 6.5mm and 14mm respectively. The flow path length in the heat sink was 814mm. These values produce a flow channel area of

$$A_i = 0.814 * 2 * (0.014 + 0.0065) = 0.0334 \text{ m}^2 \quad (6.5)$$

The convective heat transfer coefficient  $h$  is found using the Colburn equation relating the dimensionless Nusselt, Reynolds and Prandtl numbers (Cengel & Boles, 2009) where  $n = 0.4$  if the fluid is being heated and  $n = 0.3$  if the fluid is being cooled. This equation only applies to turbulent internal flow in pipes.

$$Nu = 0.023 * Re^{0.8} Pr^n \quad (6.6)$$

The definition of the Nusselt number is

$$Nu = \frac{hL_c}{k} \quad (6.7)$$

The turbulence inside the flow channel, and therefore the validity of the Colburn equation, is ensured due to the several 180° bends in the flow path. The Prandtl number for water is tabulated corresponding to fluid temperatures and was taken as 8.09 at an average temperature of 15°C at the inlet of the heat sink (Cengel & Boles, 2009). The Reynolds number is calculated using

$$Re = \frac{\rho v L_c}{\mu} \quad (6.8)$$

Thus, the convective heat transfer coefficient depends on the Nusselt number, which depends on the Reynolds number, which in turn depends on the flow velocity and the flow velocity depends on the flow rate. It is this volumetric flow rate that was selected to correspond to nominal values and all other dependent parameters were calculated based on this selection. The chosen values were 0.75, 1.14, 2.0 and 2.685 liters per minute. The value of 2.685 L/min was chosen such that the corresponding dimensionless number  $IT$  corresponds to that which is expected to apply to the heat transfer fluid flow rate in the Stirling engine head. The other three values were chosen to obtain a more versatile graph that could apply for any heat storage – heat engine system.

The data provided by these tests was intended to be generalized and valid for heat storage with the same geometry and heat transfer mechanisms to the heat engine. The results are presented in such a way as to be applicable for any scale of heat storage and engine that makes use of graphite as a sensible heat storage material. In other words, figures 6.2 and 6.3 can be used as a reference to determine the discharge rate of any similar heat storage device. It must have similar geometry and identical materials. Since having identical geometry between the test apparatus and a prototype is unlikely, the results of these tests should be used as a guide to predict general trends of discharging behavior. For both samples, the initial temperature at the onset of discharging was 500 °C.

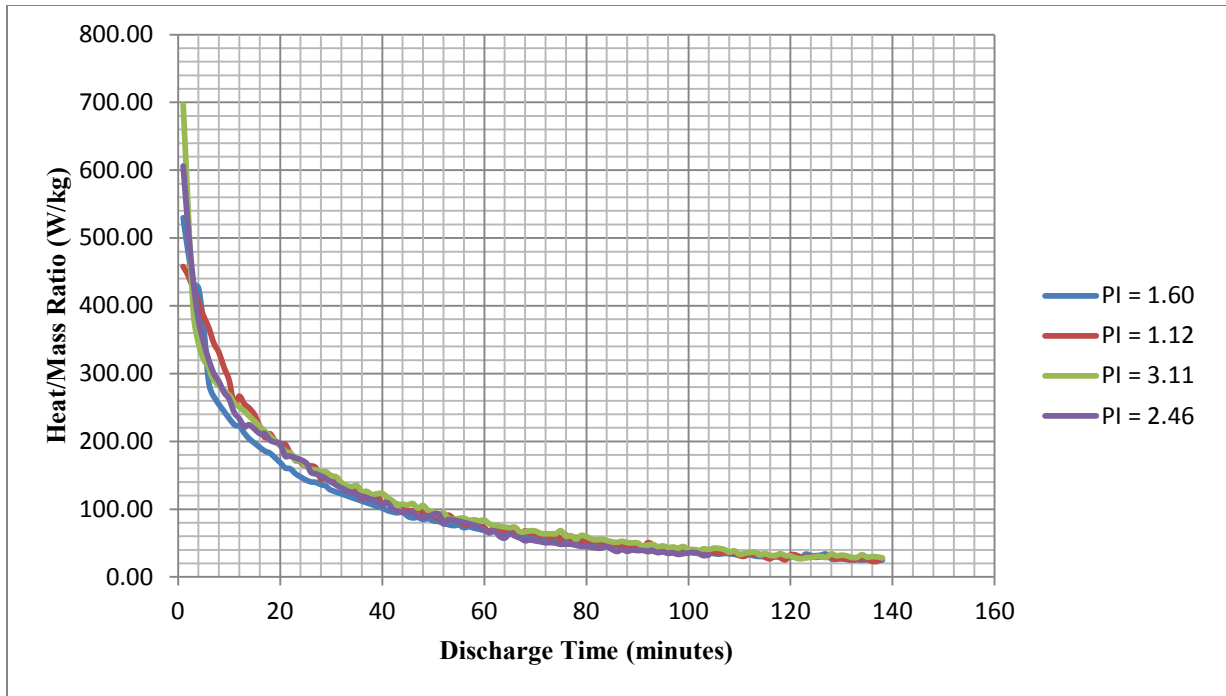


**Figure 6.2: Discharging power per unit mass of a graphite based sensible TES (high grade graphite)**

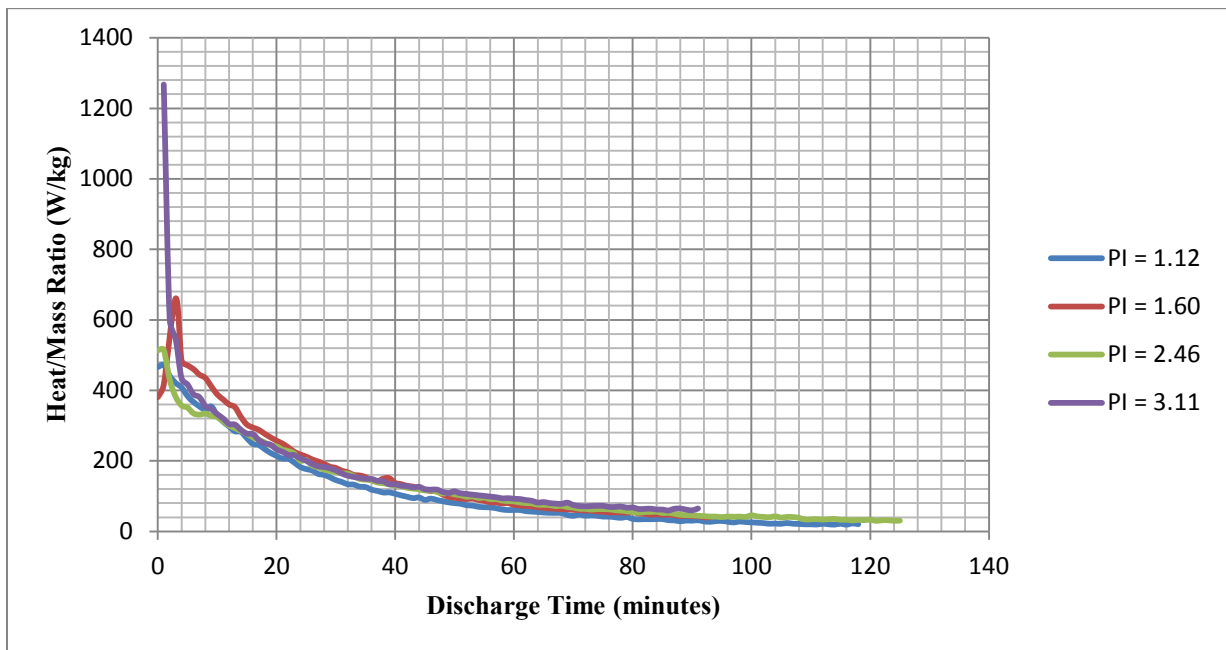


**Figure 6.3: Discharging power per unit mass of a graphite based sensible TES (low grade graphite)**

In both of high and low grade graphite, the differences in discharging heat rates for different dimensionless numbers is greatest in the first few minutes of discharging. As time progresses, the discharge heat rates rapidly converge to a common value regardless of the dimensionless number. Although, the difference and the convergence is less pronounced for the low grade graphite. This would suggest that the dimensionless number  $\Pi$  has very little effect on the discharging heat rate since all curves are nearly superimposed. However, the dimensionless number was changed by varying the fluid flow rate. All other parameters were unchanged. Therefore we can conclude that the fluid flow rate, and thus the convective heat transfer coefficient has very little effect on the discharging heat rate. This conclusion agrees with the principle of the Biot number  $Bi$

$$Bi = \frac{hL_c}{k} \quad (6.9)$$

$$L_c = \frac{V}{A_s} \quad (6.10)$$

which is a ratio of convection on the surface of a body to the conduction within the body. For  $\Pi = 2.654$ , the corresponding Biot number is 1.3. Since it is greater than unity, convection is dominant and the heat transfer is limited by the conduction in the graphite. This is the reason why varying the flow rate had little effect. If the test had been conducted such that the Biot number was less than unity, the convective heat transfer coefficient and thus the dimensionless number  $\Pi$  would have had a greater effect on the discharging heat rate. There would be a greater separation between curves. In this case however the thermal resistance of the graphite itself was greater than the thermal resistance of the heat sink. The temperature distribution in the material

can be assumed to be uniform if  $Bi \leq 0.1$  (Cengel & Boles, 2009). In this case, the heat can only be removed as quickly as the convection permits and the conduction is limited, hence the uniform temperature distribution. The Biot number for this test represents the opposite. The heat removal can only be accomplished as quickly as the conduction allows, which explains why varying the flow rate had little effect. However, these are merely assumptions. The Biot number remains a ratio that only identifies whether convection or conduction is dominant. If the flow rate had been reduced such that the dimensionless number  $Bi$  had been small enough such that  $Bi \leq 0.1$ , then conduction would be dominant and convection would be the limiting factor. In this case, there would have been a greater separation between discharging curves.

## **6.2 Full Cycle Simulation and Efficiency**

In the previous section, several plots of discharging power were presented for a graphite based, rectangular prism shaped sensible heat storage. The data was presented in such a way as to make the scale of the test irrelevant and was intended to be used as a design guide for this type of heat storage.

In this section, the charging behavior and charging-discharging efficiency are discussed and evaluated. The intent was to determine the adequacy of the insulation used and to quantify the heat loss through the insulation.

### **6.2.1 Efficiency**

The experimental setup used for this test was the same as the discharging test and is shown in figure 6.1. First, the graphite was heated from room temperature to 500 °C using the resistance heater with a resistance of 23 Ω. The charge voltage was set to 110.5 V and kept constant until the temperature was reached. This took 45 minutes. At this moment, the charge power was cut

and the heat sink was placed onto the graphite with an average water flow rate of 0.0083 kg/s. The graphite was allowed to cool by the heat sink until it returned to room temperature. The data for all six temperatures and the flow rate were recorded by a data acquisition module every five minutes during the entire test which lasted a total of 225 minutes for the full charge-discharge cycle.

The intent was to determine how much of the heat delivered to the graphite was lost through the insulation during the cycle. This quantity represents the quality of the insulation material and construction. Knowing how much power was delivered by the heater and the time over which it was applied, one can calculate the total charge energy provided to the graphite according to

$$Q_c = \frac{V^2}{R} \Delta t \quad (6.11)$$

Since the voltage was kept constant, the time increment in this equation was the entire charging period. All of the discharged energy is ultimately provided to the water flowing in the heat sink. To calculate the total energy discharged by the graphite to the heat sink, one can make use of the known specific heat capacity of water of 4.18 kJ/kgK at room temperature using

$$Q_d = \dot{m}c(T_6 - T_5)\Delta t \quad (6.12)$$

to calculate the change of internal energy of the water. However, the mass flow rate and the temperature difference varied during the discharging period, thus the time increment could not be

the entire discharge time. Rather, the energy discharged was calculated using an integral approximation by discretizing the time increments.

$$Q_d = \int_0^t \dot{Q}_d(t) dt \approx \sum_{i=1}^n \dot{m}_i c (T_{6,i} - T_{5,i}) \Delta t \quad (6.13)$$

The time increment was equal to the data measurement time increment which was 5 minutes. The accuracy of this approximation increases with smaller time increments. The data for this test is shown in figure 6.4 and 6.5.

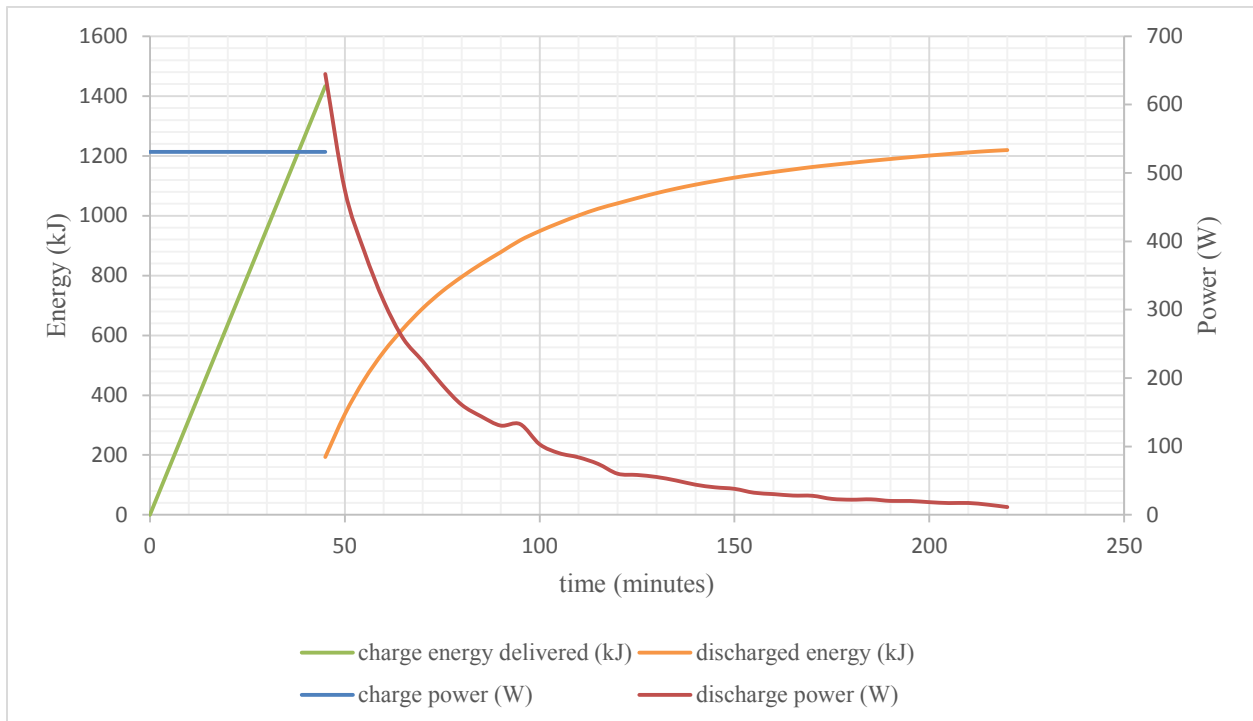


**Figure 6.4: Charge and discharge energy and power (high grade)**

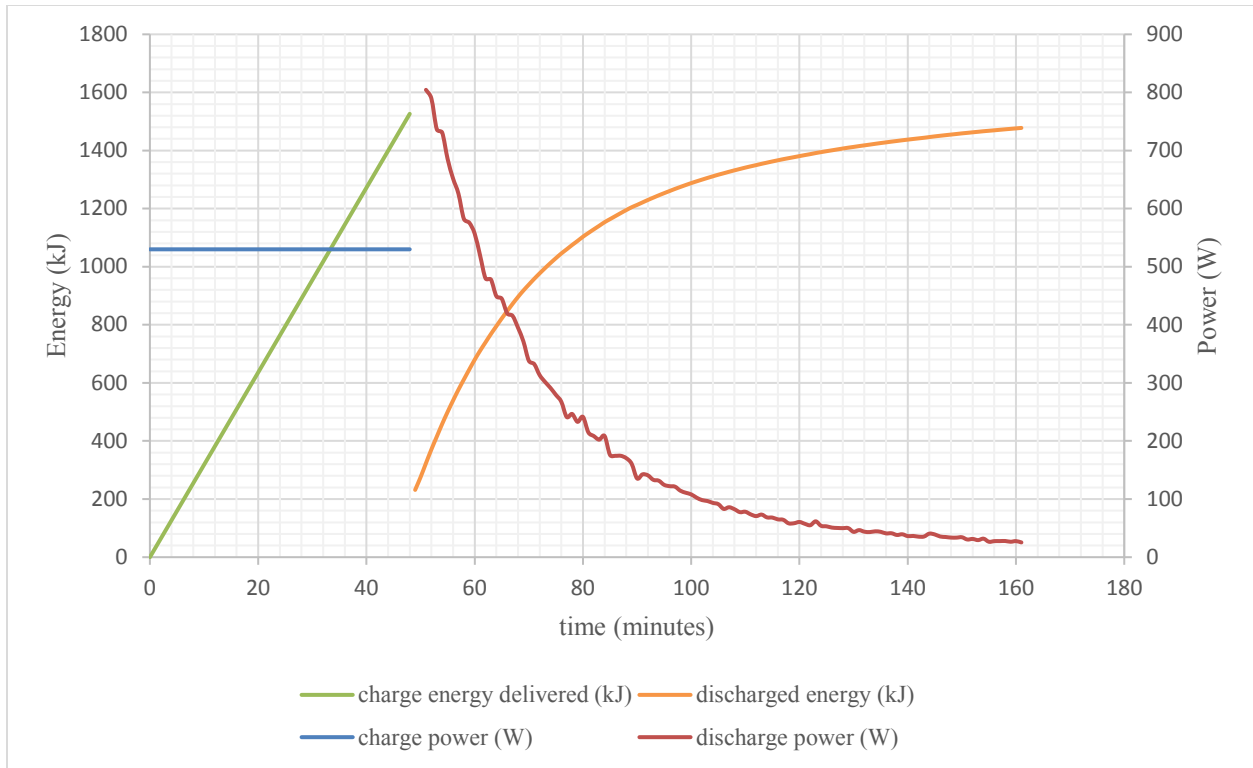


**Figure 6.5: Charge and discharge energy and power (low grade)**

In accordance to the first law of thermodynamics, any difference between the heat provided  $Q_c$  to the graphite during the charging and the heat provided by the graphite  $Q_d$  must be attributed to heat that was lost through the insulation, provided that the graphite was cooled back to its original temperature before heating. This heat loss should be minimized and the quality of the insulation can be quantified by the discharging efficiency  $\eta_d$  defined as

$$\eta_d = \frac{Q_d}{Q_c} \quad (6.14)$$

The electrical energy delivered to the high grade graphite was 1433 kJ and it discharged 1219 kJ of heat to the heat sink resulting in a discharging efficiency of 85%. The low grade graphite was provided 1526 kJ of electrical energy and only discharged 1477 kJ of heat to the heat sink resulting in a discharging efficiency of 97%.

The difference in efficiencies between the high and low grade graphite is mostly due to lack of precision of the instruments used to measure the discharged energy and the method used to calculate it. In theory, the efficiencies should be the same since it is a property of the insulation, not the type of graphite, and the same insulation was used in both cases.

A considerable source of error was the transition from charging to discharging. During the charging period, there was no heat sink on the graphite in order to avoid including the heat capacity of the heat sink itself to the heat storage. This implies that when came the time to cut the power and discharge, the insulation was opened and the graphite was exposed to ambient air. During this transition period, the heat sink was placed onto the exposed surface, the hoses were connected to the heat sink, the water flow was activated and finally the insulation was closed once again until the end of the test. This transition period required fine motor skills and as such, the time it took varied. As a result, some heat was lost by convection to the ambient air that was not accounted for while the insulation was open.

Furthermore, the erratic flow rate of the water caused considerable error. Sometimes, the flow rate would drastically decrease randomly without tampering with the valve. This implies that the flow rate that was measured at the end of every time interval may have been very different from the actual flow rate during that interval. Considering the discretized integral approximation used

to calculate the discharged energy, one can see how this would cause some error since the equation is dependent on flow rate.

The efficiencies determined from this test only apply to this test since it depends strongly on the time to complete a full cycle. In this test, the discharging began immediately after the charging was completed. During operation of an actual heat storage, the charge would most likely be held for some time before discharging. The discharging would also be periodic, responding to an energy demand from the user. Longer cycle times, as well as higher maximum temperatures, result in greater losses through the insulation. Therefore, the efficiencies determined from this test are only valid for the specific case of a maximum temperature of 500 °C, constant power supply of 530 W and immediate discharging after charging.

### **6.2.2 Full Cycle Simulation**

In the previous section, the quality of the insulation was quantified by attributing a charging-discharging efficiency to the heat storage which was defined for a specific set of parameters such as charging power, maximum temperature and immediately discharging after charging. Although this efficiency is a good indicator of the quality of the insulation, it does not provide much insight as to how the heat storage would perform under standard operating conditions. There are several ways in which the efficiency test differs from operation.

The most important difference is the constant charging power. During the efficiency test, the power was constant and set to maximum until 500 °C was reached. In reality, the heat provided to the heat storage would vary according to the position of the sun as the day progresses. Another difference is that the maximum temperature was arbitrarily chosen to be 500 °C while the actual maximum temperature is unknown. A third difference is the immediate and continuous

discharging after the charging was completed. During typical operation, the charge would be held for some time and the discharging would be randomly intermittent.

To gain some insight as to how the heat storage would perform under standard operating conditions, a test was conducted to simulate, as best as possible, a full charging and discharging cycle as it would typically happen during operation. However, due to the random and intermittent nature of the discharging during operation, a standard operating condition cannot be defined. For this reason, the simulation considers only the charging of the heat storage.

The same test apparatus, shown in figure 6.1, was used without the heat sink to simulate the charging under normal operation. This was accomplished by providing variable input power. The CSP system, of which the heat storage is a component, was intended to be used in warm countries located near the equator. New Delhi, India, in January, was chosen as the reference location and time to evaluate charging performance. Hourly solar irradiance data for New Delhi was used as the basis for the test (energyplus.net, 2016). The solar concentration factor is defined as the ratio of the irradiance at the TES receiver to the irradiance on the mirrors. Using this hourly data and multiplying it by the solar concentration factor of 62.4 due to the mirrors, the solar radiation incident on the actual graphite block was obtained. The solar concentration factor of 62.4 was determined by analysis of the concentrator conducted by a partnered research group. In order to simulate the actual heat storage, the ratio of the solar radiation incident on the actual block to the electrical power provided to the test sample was set equal to the ratio of their masses. Using a 5 kWh capacity, 65 kg actual storage block, the ratio of their masses and their input power was 42. This way, both the actual storage block and the sample have the same heat-mass ratio. Therefore, being composed of the same material and having the same specific heat capacity, they would reach the same temperatures for every hour of the charging period.

The geometry of the mirrors is such that the solar radiation concentrated by the mirrors is only significant between the hours of 9:00 am and 3:00 pm. Beyond these hours, the angle of incidence is too acute and the rays are not captured by the mirrors. As a result, the charging period lasts 6 hours. The test sample was charged for six hours and the electrical power provided to it was changed every 15 minutes in accordance to the expected heat-mass ratio. The power provided is shown in table 6.1.

**Table 6.1: Variable input power provided to TES model to simulate solar flux**

<b>time of day</b>	<b>concentrated solar radiation on actual storage (W)</b>	<b>electrical power provided to test sample (W)</b>
9:00	1400	34
9:15	1777	43
9:30	2154	52
9:45	2531	61
10:00	2908	71
10:15	3170	77
10:30	3432	83
10:45	3694	90
11:00	3956	96
11:15	4169	101
11:30	4382	106
11:45	4595	112
12:00	4808	117

12:15	4624	112
12:30	4440	108
12:45	4256	103
13:00	4072	99
13:15	3832	93
13:30	3592	87
13:45	3352	81
14:00	3112	76
14:15	2807	68
14:30	2502	61
14:45	2197	53
15:00	1892	46

The test began at room temperature and the variable power was provided according to table 6.1 for six hours. Figure 6.6 shows the temperature of the graphite as it was being charged. Although the input power was changed every fifteen minutes, the temperature was measured every minute.

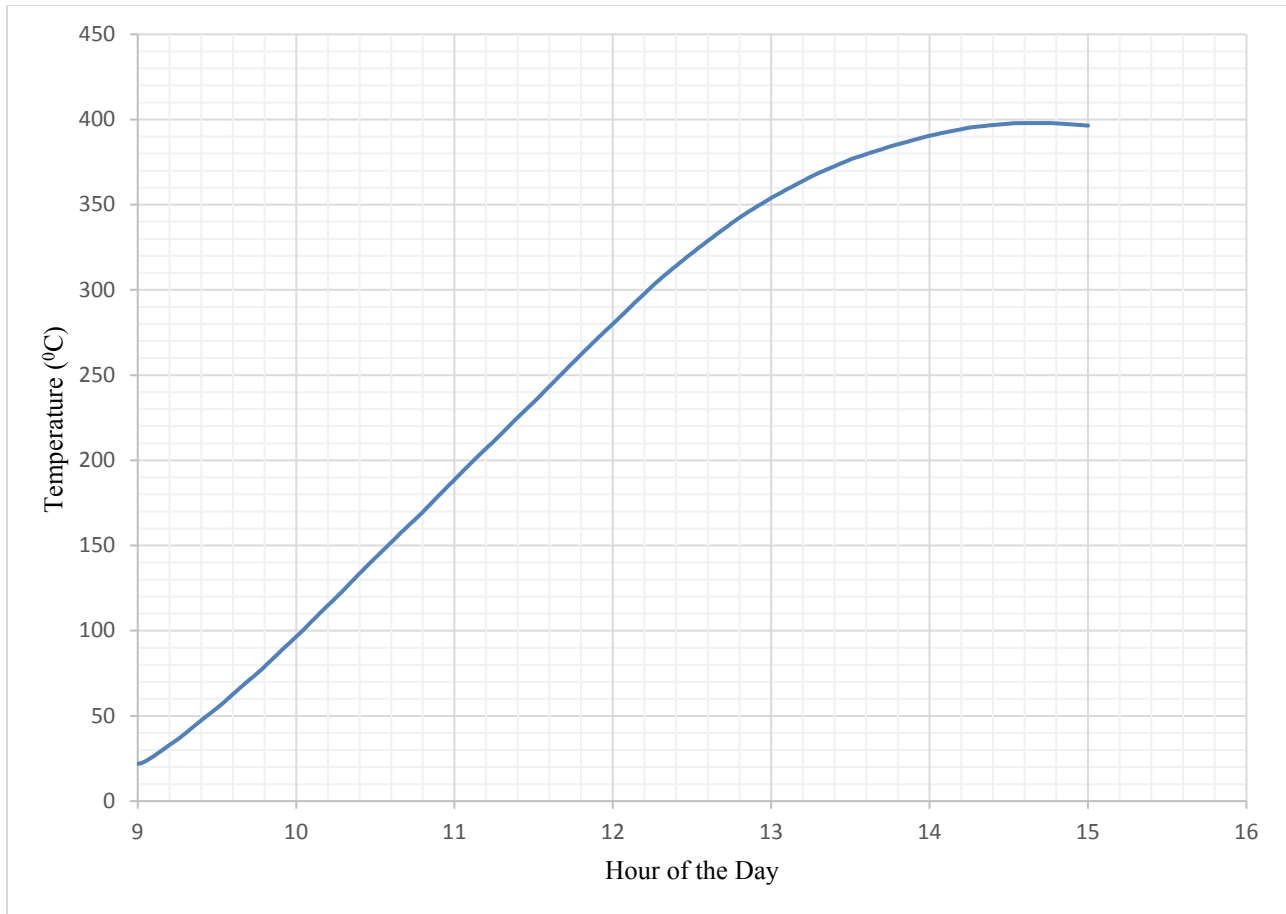


**Figure 6.6: Temperature of TES during the daytime charging period (high grade graphite)**

Note that the maximum temperature reached was 398 °C at 14:44 hrs and that the temperature began to decrease after this time despite the fact that it was still being heated. This indicates that the heat loss through the insulation actually exceeded the heat input after that moment. Unlike the parameters for the efficiency test, the maximum temperature was not 500 °C. Therefore, as mentioned in previous sections, the results found from the charging-discharging test and the efficiency test do not represent the performance of the heat storage under standard operating conditions. They merely quantify the quality of the heat storage under test conditions.

The main quantity of interest, obtainable by this test, is the amount of absorbed heat. Knowing the heat capacity of the graphite and the temperature difference between initial and final conditions, one can calculate the specific internal energy change of the graphite according to

$$\Delta u = c\Delta T \quad (6.15)$$

As it is written, the equation is independent of mass, making it applicable to any scale of heat storage of similar design. Since the specific heat capacity of the graphite varies with temperature, its value is taken as that at the average temperature of the process. In this test, the initial and final temperatures are 22 °C and 396 °C respectively. Using these values to calculate internal energy change would yield the amount of absorbed solar radiation during the charging period. However, this does not necessarily represent the amount of useable energy. The heat from this storage is intended for use with a heat engine. Preliminary analysis of the Stirling engine which was intended to be used in conjunction with this heat storage indicated that it had a minimum operating temperature of 300°C at the interface between the heat storage and engine head. Below this temperature, the heat flux to the engine is insufficient to overcome internal friction. In essence, the engine stalls below this temperature. Therefore, the useable heat that the engine can provide to the Stirling engine occurs between 396 °C and 300 °C.

For this reason, two different quantities for internal energy change are calculated – the absorbed heat, occurring between 22 °C and 396 °C, and the useable heat, occurring between 300 °C and 396 °C. Table 6.2 presents the results per unit mass of graphite for this type of heat storage-heat engine system.

**Table 6.2: Graphite based TES capacity**

	kJ/kg	kWh/kg
<b>Absorbed heat</b>	468	0.13
<b>Useable heat</b>	160	0.044

According to these results, a 65 kg graphite based sensible heat storage would be able to provide 2.86 kWh of useable heat to the Stirling engine. It is important to note that these values depend not only on the heat storage. The absorbed heat also depends on the solar concentration factor provided by the mirrors. The useable heat depends on the solar concentration factor and the engine. An engine with a stall temperature of less than 300 °C is preferable. Thus these, values evaluate the performance of the entire system and not the storage alone. Furthermore, if the charging period had begun with an initial temperature of 300 °C instead of 22 °C, the maximum temperature reached during the charging may have been higher, resulting in a higher useable heat. During operating conditions, the heat storage would never cool to 22 °C.

Since the objective of this research is to evaluate the feasibility of the heat storage alone, the charging efficiency  $\eta_c$  should be independent of the effects of the engine which effects the useable heat. For this reason, the charging efficiency is defined as the ratio of the absorbed heat to the heat provided. Defined this way, the charging efficiency under standard charging conditions is 40.2%.

## Chapter 7: Resistance to Vibration

The Stirling engine is expected to vibrate vertically and horizontally. The harmonic motion of the engine's head will therefore cause some forces normal to and parallel to the surface of the graphite through direct contact during discharging periods. Considering the mechanical properties of graphite, the shearing forces on the surface may cause significant wear while the normal forces may cause some brittle fracture. The vibration in the graphite may also cause the internal microstructure of the graphite to degrade due to fatigue.

The ease with which wear occurs on graphite is due to its microstructure which is illustrated in figure 7.1. Carbon typically forms 4 covalent bonds. In graphite, only three of these bonds are strong covalent bonds while the fourth is a weak secondary bond. This weak bond can easily be broken, causing adjacent planes to shear off easily. This makes it particularly sensitive to shear stresses. This is one of the reasons graphite powder is often used as a dry lubricant. With a flexural strength of 55 MPa, it is relatively brittle and is therefore susceptible to brittle fracture (Entegris, 2013).

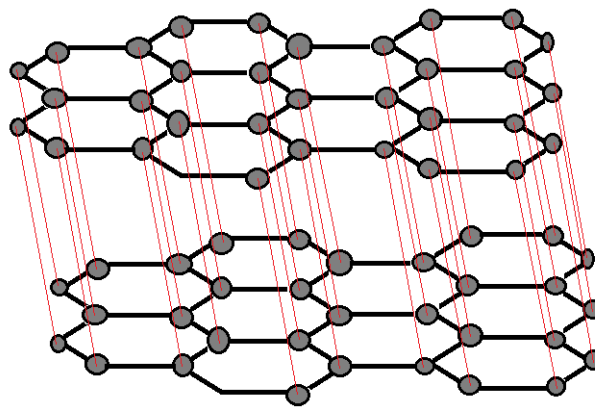


**Figure 7.1: Crystal structure of graphite showing primary bonds (black lines) and weak secondary bonds (red lines)**

A test was conducted to evaluate the degrading effects of vibration on the surface and the structure of the graphite. Again, this test was set up in such a way as to be a scaled down model of the prototype with only the components necessary to evaluate the effects of vibration.

As shown in figure 7.2, a piston was inserted into a cylindrical hole that was drilled into the graphite. The diameters of the piston and the hole were such that there was a very small clearance so as to allow free motion of the piston while ensuring contact along the majority of the circumference. The piston was smooth mild steel. The opposite end of the connecting rod was linked to a motor with a crankshaft with an eccentricity of 3.175 mm. It was set up as a classic crank and slider mechanism resulting in a stroke of 6.35 mm for the piston, in accordance to the specifications of the engine as provided by the designers. The connecting rod was supported only by the graphite at one end and the engine at the other end. This was to ensure constant contact between the piston and the graphite in case the hole enlarged due to wear. The graphite block was placed so that the piston would strike the bottom of the hole in order to apply a normal stress as well. The graphite block was supported such that it had only one degree of freedom which was parallel to the stroke. A sheet of polystyrene was placed behind the graphite block to act as a spring and as a damper, however the spring and damper constants are not known. They were merely introduced to prevent damage to the motor. As it was setup, the graphite experienced shear stresses on the horizontal surface and normal stresses on the bottom of the hole. The engine design team expected an operating frequency of 750 – 1000 rpm. The frequency at which this test was conducted was set to 1000 rpm, which is the highest expected operating frequency of the coupled engine.

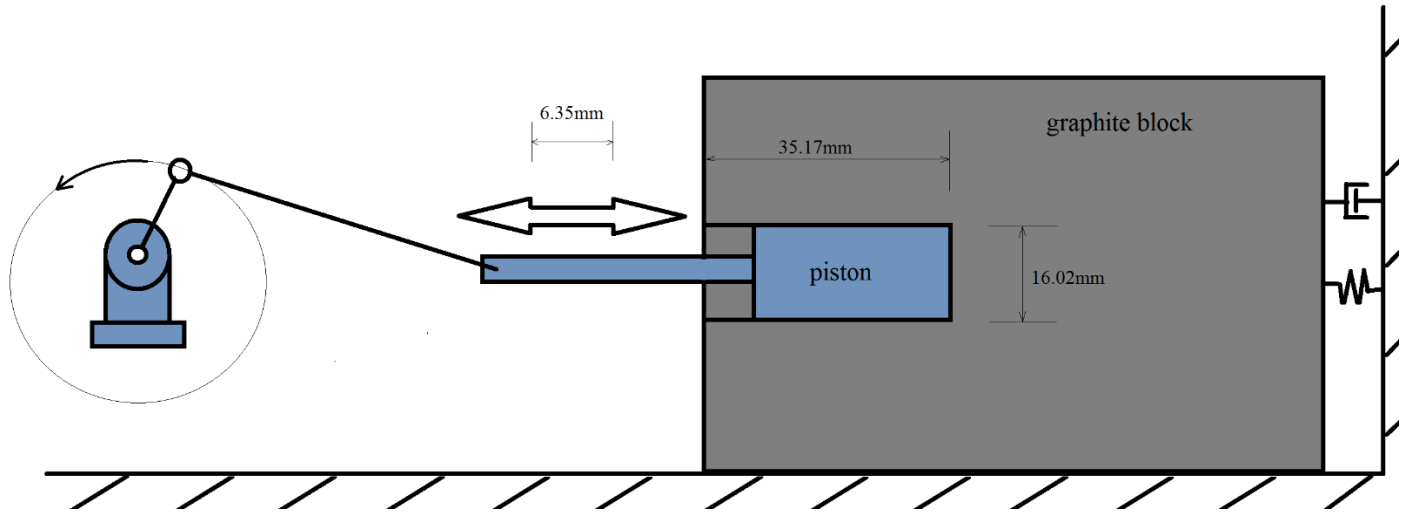


**Figure 7.2: Vibration test rig setup**

Before beginning the test, the diameter and the depth of the hole were measured using a digital Vernier caliper with a precision of 0.01 mm. Then, the block was lightly brushed to remove dust and weighed with a scale with a precision of 0.01 g. The visual appearance of the surface of the graphite inside the hole was noted and photographed.

The motor was then turned on and set to 1000 rpm. The same measurements and photographs were taken after every two-hour interval for a total of 6 hours of vibration exposure. During the measurements, it was also noted whether some graphite dust or debris had accumulated. This same procedure was followed for the high grade and low grade graphite. Table 7.1 summarizes the observations at each measurement interval.

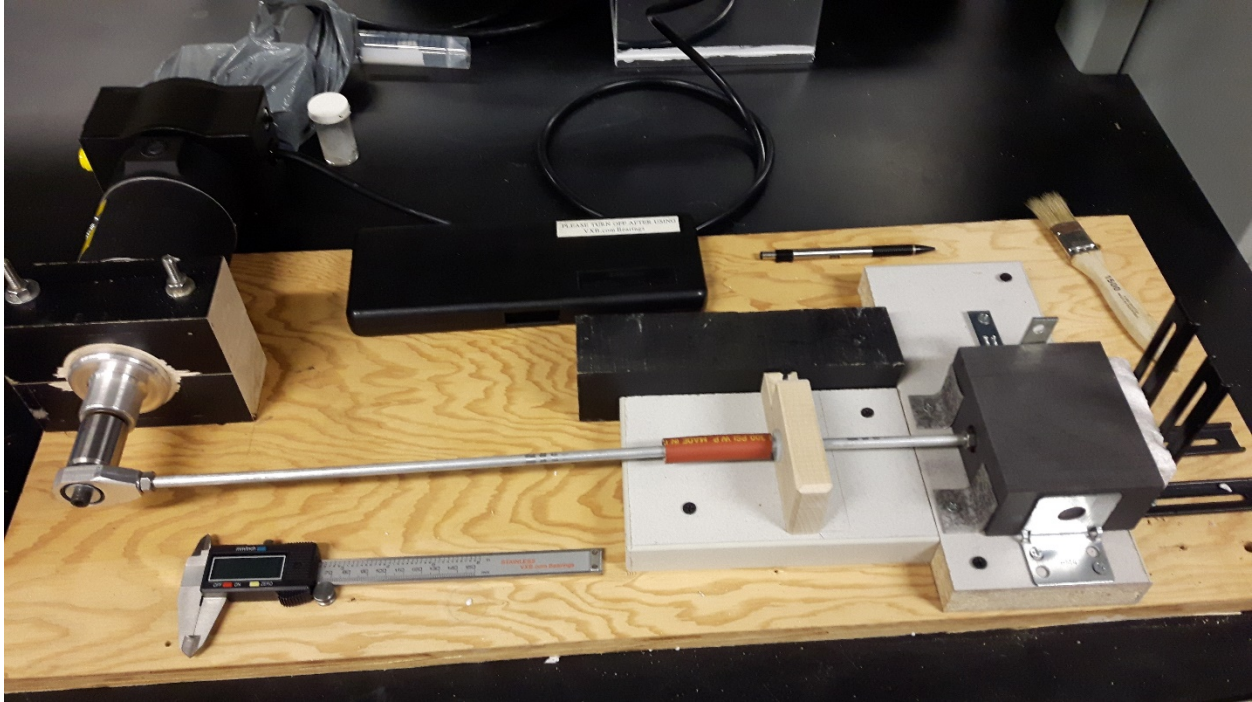


**Figure 7.3: Vibration test rig setup**

**Table 7.1: Degradation of high grade graphite due to vibration at 1000 rpm**

<b>Exposure Time (hours)</b>	<b>Frequency (rpm)</b>	<b>Hole Diameter (mm)</b>	<b>Hole Depth (mm)</b>	<b>Mass (g)</b>	<b>Remarks</b>
0	-	16.03	35.17	691.65	No signs of degradation, no dust.
2	1000	16.01	35.08	691.65	No signs of degradation, no dust.
4	1000	16.03	35.08	691.66	No signs of degradation, no dust.
6	1000	16.04	35.11	691.65	No signs of degradation, no dust.

**Table 7.2: Degradation of low grade graphite due to vibration at 1000 rpm**

<b>Exposure Time (hours)</b>	<b>Frequency (rpm)</b>	<b>Hole Diameter (mm)</b>	<b>Hole Depth (mm)</b>	<b>Mass (g)</b>	<b>Remarks</b>
0	-	16.08	35.68	656.53	No signs of degradation, no dust.
2	1000	16.03	35.61	656.52	No signs of degradation, no dust.
4	1000	16.10	35.60	656.50	No signs of degradation, no dust.
6	1000	16.00	35.58	656.50	No signs of degradation, no dust.

It is quite clear that at this frequency and with this type of contact, graphite undergoes no significant structural degradation. The exposure to vibration was stopped after six hours because no change was noted during that period. There was no indication the continuing the test beyond 6 hours would yield different results. The variation in the measured hole dimensions is likely due to lack of instrumental precision considering that the caliper was hand held and was thus subject to imperfect alignment. The fact that the measured diameter decreased from one interval to the next is non-sensical and can only be attributed to measurement error. Hole depth measurements were subject to the same sources of error. As for the mass measurement, they were nearly constant. For the low grade graphite, the data indicates a loss of 0.03 g over the six hour exposure. However, if any graphite had been worn off the surface, it should have been found as a fine powder somewhere on the test rig. No powder was found on the piston, on the table or in the hole. However, we must ensure that the operating frequency is far from the natural frequency of the graphite block in order to avoid resonance. The natural frequency of any elastic material in one dimension is

$$\omega_n = \sqrt{\frac{B}{m}} \quad (\text{rad/sec}) \quad (7.1)$$

where  $B$  is the spring constant and  $m$  is the mass. The spring constant can be found using

$$B = \frac{EA}{L} \quad (7.2)$$

Where  $E$  is Young's modulus,  $A$  is the cross-sectional area and  $L$  is the length. The average Young's modulus for graphite is 11 GPa (UCAR Carbon Company Inc., 1991). The dimensions of the graphite block for the prototype are 0.5x0.5x0.4 m. The natural frequency is

$$\omega_n = \sqrt{\frac{EA}{mL}} = \sqrt{\frac{11 * 10^9(0.5)^2}{152(0.4)}} = 6725 \text{ rad/sec} \quad (7.3)$$

Multiplying by  $60/2\pi$  yields 64222 rpm which far exceeds the frequency at which the engine is expected to run. Although this analysis is very crude and overly simplified, the actual resonant frequency is much larger than the operating frequency. Thus, resonance is not a concern.

Whether the parameters for this test match those that the prototype would be subject to cannot be known until the specifications for an engine are provided as well as the type of coupling between the heat storage and the engine. Again, the chosen parameters were deemed to be the most likely. Under these conditions, the graphite block undergoes no significant degradation.

## **Chapter 8: Heat Storage Prototype Design**

In this chapter, the mechanical configuration, dimensions, materials and specifications of a complete graphite based sensible heat storage device is proposed for optimal performance at minimum cost. It is essentially a suggested design for this type of heat storage. The specifications are based on the intended application of the system and on the material properties of the graphite obtained from the tests, which are presented in previous chapters. All proposed design decisions are explained and justified through detailed analysis with the goals and objectives kept in mind.

The intended application for this heat storage is to absorb heat as concentrated solar radiation and to provide heat to a Stirling heat engine. The scale of the storage is such that it can store the energy demand of one home in a developing country with a warm climate. More specifically, this energy demand was evaluated at 25 kWh per day. Therefore the heat storage system is designed to provide 25 kWh of heat, operating with a minimum temperature of 300 °C, which is the specified stall temperature of the Stirling engine. All the proposed specifications for the device are intended to optimize the performance of the storage as a component of a larger system. This system also includes an array of mirrors and a heat engine. In other words, the design is based on the specifications of the coupling between the storage, mirrors and engine. Any reader referencing this text should only take it as a general outline if the solar radiation concentration factor and engine stall temperature differ from those of this particular system. The high grade graphite is used as the storage material.

### **8.1 Mass of the Graphite Block**

The mass of the graphite block is the first quantity that must be determined since it determines the volume on which all the dimensions are dependent on. The required mass can be calculated

knowing the specific heat capacity, the required capacity of 25 kWh and the temperature variation. The high grade graphite has a specific heat capacity of 1.445 kJ/kgK at 300 °C. For the same storage capacity, a smaller mass will have a higher maximum temperature and a larger mass will have a lower maximum temperature. With higher maximum temperature, we obtain better engine efficiency and reduce the material cost for graphite, but higher temperature also decreases the effective lifespan and increases the heat losses. As a compromise, and to remain within the limits of temperatures that were tested in the laboratory for oxidation, the maximum temperature was chosen to be 710 °C. The mass of the graphite is found as follows.

$$m = \frac{Q}{c(T_{max} - T_{min})} = \frac{25 \text{ kWh} \left( 3600 \frac{\text{kJ}}{\text{kWh}} \right)}{1.445 \frac{\text{kJ}}{\text{kgK}} (710 \text{ }^{\circ}\text{C} - 300 \text{ }^{\circ}\text{C})} = 152 \text{ kg} \quad (8.1)$$

Knowing the density of the high grade graphite as 1818 kg/m<sup>3</sup>, the volume of the block is

$$V = \frac{m}{\rho} = \frac{152}{1818} = 0.0836 \text{ m}^3 \quad (8.2)$$

This analysis is based on the assumption that the graphite's temperature will vary between 300 °C and 710 °C, however the test conducted to simulate the charging yielded a maximum temperature of 396 °C. Having this maximum temperature would require a much greater mass in order to have the same storage capacity. There are two main reasons for this relatively low maximum temperature. Firstly, the actual storage would ideally never drop to below 300 °C so the charging period would not begin at 20 °C as was the case for the test.

Secondly, and more importantly, the insulation of the test apparatus was inadequate. As can be seen in figure 6.6, the temperature begins to drop at 14:30 hrs after reaching a maximum temperature of 396 °C despite the graphite being heated at 61 W. This indicated that the heat loss at temperatures greater than 396 °C exceeds the input heat. Thus at 710 °C, the heat loss would be excessively high. It is for this reason that the ceramic fiber insulation panels were inadequate.

## **8.2 Insulation**

As an alternative to the ceramic fiber panel as the insulation material, a vacuum layer is proposed. It should be noted that this method of insulation was not tested and its justification is strictly analytical. The details of the proposal are as follows.

The graphite block is encased in a sealed steel box with dimensions slightly larger than that of the graphite. In this manner, there is a small gap between the surface of the graphite and the inner walls of the steel casing. A valve is installed on the casing such that a vacuum pump can be connected and remove the air occupying the gap. Obtaining an absolute vacuum inside the casing and maintaining it indefinitely solves two major problems. Aside from the intended solution of eliminating heat loss, it also eliminates oxidation, eliminating the need for an anti-oxidation coating or inert gases. However, obtaining an absolute vacuum is virtually impossible. As a consequence, the question of what pressure in the casing is required in order for this method to be advantageous over ceramic fiber arises.

### **8.2.1 Relationship Between Pressure and Thermal Conductivity of a Gas**

In an ideal case, the absolute pressure in the casing is zero. At zero pressure, the space between the graphite and the inner walls of the casing is void of all matter. With no matter, heat can only be transferred across the gap by radiation because conduction and convection are impossible

since they both require some substance as a medium for heat flow. In reality, even the most sophisticated vacuum pumps cannot remove all gas molecules from a space. A model for the mechanism of heat transfer through a gas based on the kinetic theory of gases is presented. The model analytically predicts the thermal conductivity of a gas. However, to do so, we must analyse the mechanics of heat transfer at a molecular scale.

Conventional thermodynamics and fluid mechanics are valid in systems in which the continuum assumption is valid. That is, systems in which the scale is large enough to treat a fluid as a continuous medium, when in reality, it is composed of discrete particles that only interact with each other during collisions. Consider such a system in which non-equilibrium exists. Due to the non-equilibrium, there is a gradient of the arbitrary quantity  $a$  as illustrated in the figure 8.1, where  $a$  can represent either momentum, energy or mass. Since we are dealing with a large number of molecules, the quantity  $a$  is the average value carried by those molecules. The molecules below the line with quantity  $a$  will transfer some to those above the line with quantity  $a + da$  during collisions. The rate  $S$ , per unit area, at which these molecules cross the line and collide with those above is proportional to the number density  $n$  and the average molecular speed  $\bar{c}$ .

$$S = \beta n \bar{c} \quad (8.3)$$

where  $\beta$  is a constant of proportionality and  $n = N/V$  is the number of molecules per unit volume.

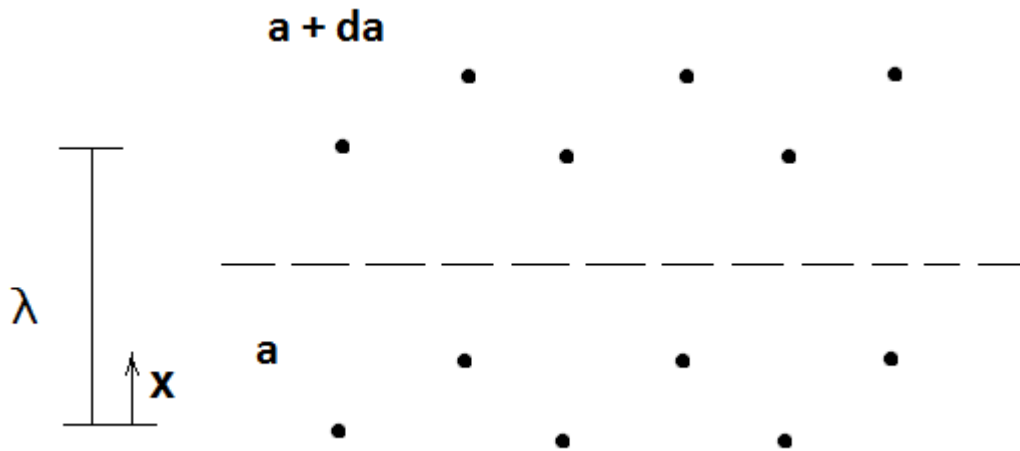


**Figure 8.1: Non-equilibrium transport of quantity  $a$  (energy or momentum or mass) carried by gas molecules**

The transport rate of  $a$ ,  $\Lambda$  per unit area is thus

$$\Lambda = \beta n \bar{c} (a - (a + da)) \quad (8.4)$$

Now, the mean free path  $\delta$ , defined as the average distance travelled by a molecule before it collides with another, is the smallest length over which any interaction can occur. In other words, the infinitesimally small length element  $dx$  becomes meaningless if it is less than  $\lambda$ . So,

$$dx = \lambda \quad (8.5)$$

Consequently, equation 8.4 can be re-written as

$$\Lambda = \beta n \bar{C} \left( a - \left( a + \frac{da}{dx} \lambda \right) \right) = -\beta n \bar{C} \lambda \frac{da}{dx} \quad (8.6)$$

This equation is valid for the transport of either momentum, energy or mass. The result suggests that the mechanism of transport for any of these quantities is the same. If we take the case of heat transfer – the transfer of molecular kinetic energy, the quantity of interest is the average energy each molecule possesses. But the average kinetic energy of the molecules in a macroscopic system is related to temperature by Boltzmann's constant  $K$ .

$$a = \frac{1}{2} m \bar{C}^2 = \frac{\xi}{2} K T \quad (8.7)$$

where  $\xi$  is the number of degrees of freedom in which kinetic energy can be stored that the molecules possess. The maximum value for  $\xi$  is 6 which includes 3 translational and 3 rotational. For example, argon, being a monatomic gas, has 3 degrees of freedom for 3-dimensional translational motion. It is treated as a point mass and therefore has no rotational kinetic energy. Nitrogen gas, on the other hand, exists as a diatomic molecule so it has 5 degrees of freedom – 3 translational and 2 rotational. The moment of inertia about the axis parallel to the bond line between the two nitrogen atoms is zero, resulting in 2 and not 3 rotational degrees of freedom.

Substituting  $a = \frac{\xi}{2} K T$  into equation 8.6, we obtain

$$\Lambda = -\beta n \bar{C} \lambda K \frac{\xi}{2} \frac{dT}{dx} \quad (8.8)$$

which now contains a temperature gradient reminiscent to Fourier's law of heat conduction

$$q = -k \frac{dT}{dx} = \Lambda \quad (8.9)$$

So thermal conductivity  $k$  of a gas is analytically determined as

$$k = \beta n \bar{c} \lambda K \frac{\xi}{2} \quad (8.10)$$

We still have an unknown constant of proportionality  $\beta$ . However, other researchers have found that  $\beta = 5/4$  agrees best with empirical data (Vincenti & Kruger, 1967). The mean free path and average molecular speed are given as

$$\lambda = \frac{1}{n\pi d^2} \quad (8.11)$$

$$\bar{c} = 2 \sqrt{\frac{2KT}{\pi m}} \quad (8.12)$$

where  $d$  is the molecular diameter (Vincenti & Kruger, 1967). Substituting these into equation 8.9, the thermal conductivity becomes

$$k = \beta \frac{\xi}{2} \frac{K}{\pi d^2} 2 \sqrt{\frac{2KT}{\pi m}} \quad (8.13)$$

This result shows that thermal conductivity does not depend on the density of the gas since neither  $n$  nor  $\rho$  is found in equation 8.13. This result is somewhat counter intuitive. We know that if there is no substance through which heat can flow, than conduction is impossible therefore thermal conductivity should approach zero as the density of the gas approaches zero. There were many simplifying assumptions made in this model, all of which are valid as long as one condition met. The counter intuitive result that thermal conductivity is independent of density is only valid if the dimensionless Knudsen number, defined as

$$Kn = \frac{\lambda}{L} \quad (8.14)$$

where  $L$  is the characteristic length of the system, is much less than unity. In the case where  $Kn \ll 1$ , the continuum model of thermodynamics and fluid mechanics is valid and thermal conductivity is independent of density. However, when  $Kn > 1$ , the continuum model is no longer valid and we enter the free molecular regime. Under this condition, collisions between molecules are rare and so there is virtually no transfer of energy, momentum or mass. In this free molecular regime in which the mean free path is comparable to the scale of the system, thermal conductivity of the gas does approach zero as density approaches zero.

Thus, the contradiction is mitigated. However, as it applies to the design of the heat storage device, the question of what pressure is required in the casing to satisfy the free molecular

regime remains. The small amount of air inside the casing is air which is composed primarily of diatomic nitrogen gas at 78%. For simplicity, the air is assumed to be entirely composed of nitrogen. Substituting the definition of the mean free path into that of the Knudsen number and satisfying the free molecular regime, we obtain

$$Kn = \frac{1}{n\pi d^2L} > 1 \quad (8.15)$$

The ideal gas law, written in terms of number of molecules is

$$PV = NKT \quad (8.16a)$$

$$P = \frac{NKT}{V} = nKT \quad (8.16b)$$

$$n = \frac{P}{KT} \quad (8.16c)$$

Substituting the result for  $n$  from the ideal gas law into the inequality yields

$$P < \frac{KT}{\pi d^2L} \quad (8.17)$$

which is the condition that must be satisfied. In the case of pure nitrogen at 500 °C,  $d = 0.4$  nm, and the characteristic length of the case is 0.6 m.

$$(8.18)$$

$$P < \frac{1.38 * 10^{-23}(500 + 273)}{\pi(0.4 * 10^{-9})^2(0.6)} = 0.035 Pa$$

Therefore, the maximum allowable pressure inside the casing is 0.035 Pa in order to block heat transfer by conduction and convection. Lower pressure would be preferable. Heat transfer by radiation remains unimpeded however.

### 8.2.2 Infrared Radiation Shielding

With the graphite block encased in a nearly evacuated steel box, the heat transfer by conduction and convection is negligible but this method does not prevent heat transfer by radiation. Low emissivity, thin sheets of aluminum lining the inner walls of the casing is proposed as infrared radiation shielding. This section presents an analysis of the effectiveness of this method.

The principle of infrared shielding is to impede the radiative heat transfer between two bodies by placing a thin sheet of a material that is highly reflective to infrared wavelengths between them. Incident electromagnetic radiation of intensity  $G$  can interact with a surface in three ways. It can be reflected, transmitted and absorbed. In accordance to the first law of thermodynamics, the sum of the reflected beam intensity  $R$ , the transmitted beam intensity  $T$  and the absorption  $A$  must equal the intensity of the incident beam.

$$G = R + T + A \tag{8.19}$$

The intensity of these secondary beams depend on the optical properties of the surface, namely the reflectivity  $\rho$ , transmissivity  $\tau$  an absorptivity  $\alpha$ , defined respectively as

$$\rho = R/G \tag{8.20}$$

$$\tau = T/G \tag{8.21}$$

$$\alpha = A/G \tag{8.22}$$

Dividing equation 8.19 by  $G$ , we obtain

$$\rho + \tau + \alpha = 1 \tag{8.23}$$

For opaque materials, the transmissivity is zero so

$$\alpha = 1 - \rho \tag{8.24}$$

Therefore for opaque materials, some fraction of the incident radiation is reflected and the remainder is absorbed. This absorbed radiation increases the internal energy of the body which in turn increases the temperature of the body, as long as no phase change occurs. At a given temperature, a surface also emits radiant heat  $E$  in the infrared wavelengths according to

$$E = \varepsilon\sigma T^4 \tag{8.25}$$

where Boltzmann's constant  $\sigma = 5.67 \cdot 10^{-8} \text{ W/m}^2\text{K}^4$  and  $\varepsilon$  is the emissivity of the material. It should be noted that emissivity, as well as absorptivity both depend on the temperature of the material  $T$ , the wavelength  $\lambda$  and the angle of incidence  $\theta$  and are more specifically named the

spectral emissivity and absorptivity . In any case, spectral emissivity and absorptivity are always equal.

$$\varepsilon(\lambda, T, \theta) = \alpha(\lambda, T, \theta) \quad (8.26)$$

It is ultimately the emissivity, or the absorptivity, that determines the effectiveness of a material as a radiation shield. Low emissivity materials are desirable since they have high reflectivity and thus impede radiation. To simplify the analysis of the heat loss due to radiation of the heat storage, the total hemispherical emissivity, defined as the integral of the spectral emissivity over all angles and wavelengths, was used.

The heat storage was modelled as a graphite rectangular prism with dimensions 500 mm x 400 mm x 400 mm in accordance to the density and mass required for a 25 kWh hour capacity. An aluminum sheet is placed on the inner surface of the steel casing and a second aluminum sheet is placed at the midpoint of the evacuated gap between the casing and the graphite. In this manner, all six faces of the graphite block are entirely surrounded by two layers of aluminum as shown in figure 8.2.

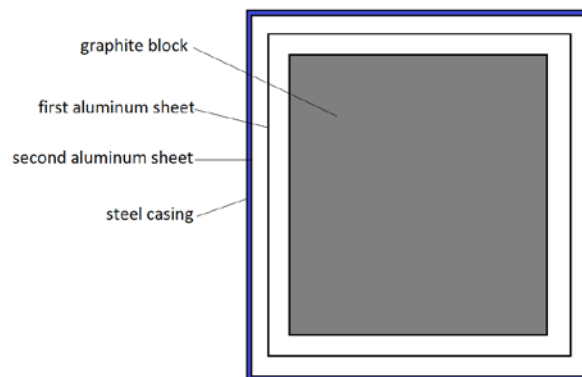


**Figure 8.2: Radiation shielding in TES casing**

The radiative heat transfer analysis was done in the form of a computational simulation program written in *Matlab*. The program was written to simulate the cooling of the heat storage while not in use with the proposed type of insulation; evacuated gap and two layers of radiation shielding. Since the casing is evacuated, convection and conduction inside the casing was considered negligible as justified in section 8.2.1. The computer simulation solves a system of energy balance equations based on the implicit finite difference method. Figure 8.3 shows the resistive network that models the heat storage and relates the emissive powers  $E_{bn}$ , surface radiosities  $J_n$  and radiative resistances  $R_n$ . For example, the energy balance equation for node  $E_{b1}$  is

$$(1/R_1)(J_1^{(i+1)} - E_{b1}^{(i+1)}) = (C/\Delta t)(T_1^{(i+1)} - T_1^{(i)}) \quad (8.27)$$

where  $i$  is the integer index corresponding to the current time step. The temperature of the graphite was assumed to be uniform in space.

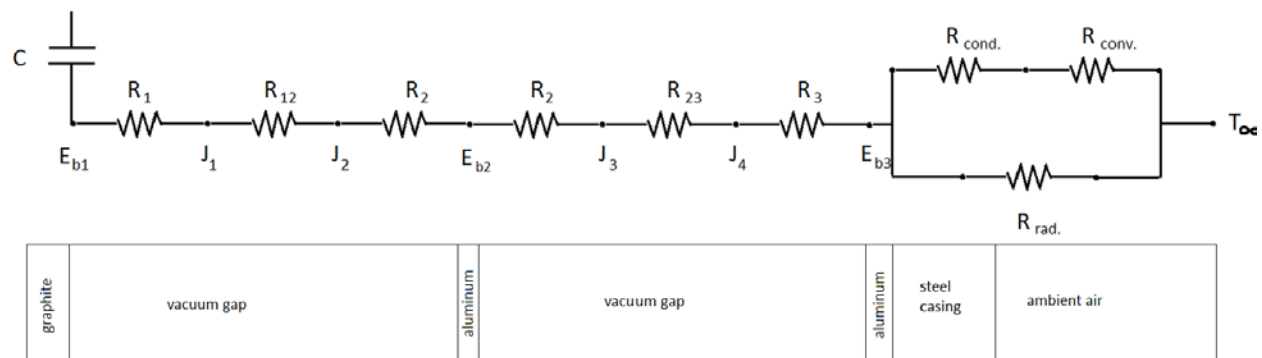


**Figure 8.3: Resistive network model of heat transfer through the radiation shielding**

The heat capacitance of the graphite  $C$  was calculated from its mass and from its measured specific heat capacity obtained from the tests described in section 4.2. The thermal capacitance and temperature gradient of the aluminum sheets were neglected because they are very thin. The heat transfer from  $E_{b1}$  to  $E_{b3}$  is purely radiative where  $R_1$ ,  $R_2$  and  $R_3$  are the surface resistances. These are only related to the emissivity and the area of the surface.

$$R_1 = \frac{1 - \varepsilon_1}{A_1 \varepsilon_1} \quad (8.28)$$

In this case, we have radiation heat transfer between graphite and aluminum. Bartl et al. suggests that the emissivity  $\varepsilon$  of aluminum, as a function of temperature is (Bartl & Baranek)

$$\varepsilon(T) = 7.2 \cdot 10^{-5} T + 3.2 \cdot 10^{-3} \quad (8.29)$$

The emissivity of graphite was found to be

$$\varepsilon(T) = 2.77 \cdot 10^{-5} T + 0.692 \quad (8.30)$$

according to *Mikron Instrument Company* (Mikron Instrument Company, 2015). The space resistances  $R_{12}$  and  $R_{23}$  are associated to the view factor between the surfaces and their areas.

$$R_{12} = \frac{1}{A_1 F_{12}} \quad (8.31)$$

the view factor from surface 1 to surface 2,  $F_{12}$ , is the fraction of the radiosity from surface 1 that is incident on surface 2. It is a purely geometric quantity. The heat transfer beyond  $E_{b3}$  towards the ambient air is conductive and convective where the nodes represent temperatures rather than radiation intensities. Since the relation between temperature and emissive power is quartic, the energy balance equations corresponding to temperature nodes could not be included in the same system of linear equations. The program simultaneously solves 5 linear equations in matrix form to obtain  $J_1, J_2, E_{b2}, J_3$  and  $J_4$ .

$$[U]\{J\} = \{Q\} \quad (8.32)$$

The 5x5 matrix  $[U]$  is a matrix of conductances, or rather the matrix of the inverse of the resistances. The vector  $\{J\}$  is the radiosities and emissive powers between the graphite and the second aluminum sheet and the vector  $\{Q\}$  satisfies the energy balance. Taking for example the node corresponding to  $J_1$ , the steady state energy balance equation is

$$U_1(E_{b1}^{(i+1)} - J_1^{(i+1)}) + U_{12}(J_2^{(i+1)} - J_1^{(i+1)}) = 0 \quad (8.33)$$

Rearranging the equation yields

$$-(U_{12} + U_1)J_1^{(i+1)} + U_{12}J_2^{(i+1)} = -U_1E_{b1}^{(i+1)} \quad (8.34)$$

Once the vector  $\{J\}$  is solved for, the temperature nodes are solved for using

$$E_b = \sigma T^4 \quad (8.35)$$

The program essentially solves 7 equations assuming steady state conditions over the time increment  $\Delta t$  of 60 seconds. However, the intent was to determine the transient process of cooling. Therefore, the program solves these 7 equations 1440 times for every minute of 24 hours. Thus, the time index  $i$  is incremented from 1 to 1440. In this way, the transient behavior is simulated with reasonable accuracy provided that the time increment is sufficiently small. The source code for this computer program is shown in appendix A for readers interested in a more detailed description of the methodology.

Running the program outputs the data as three plots to show the transient cooling process. These results are what should be expected of the actual heat storage during idle cooling.

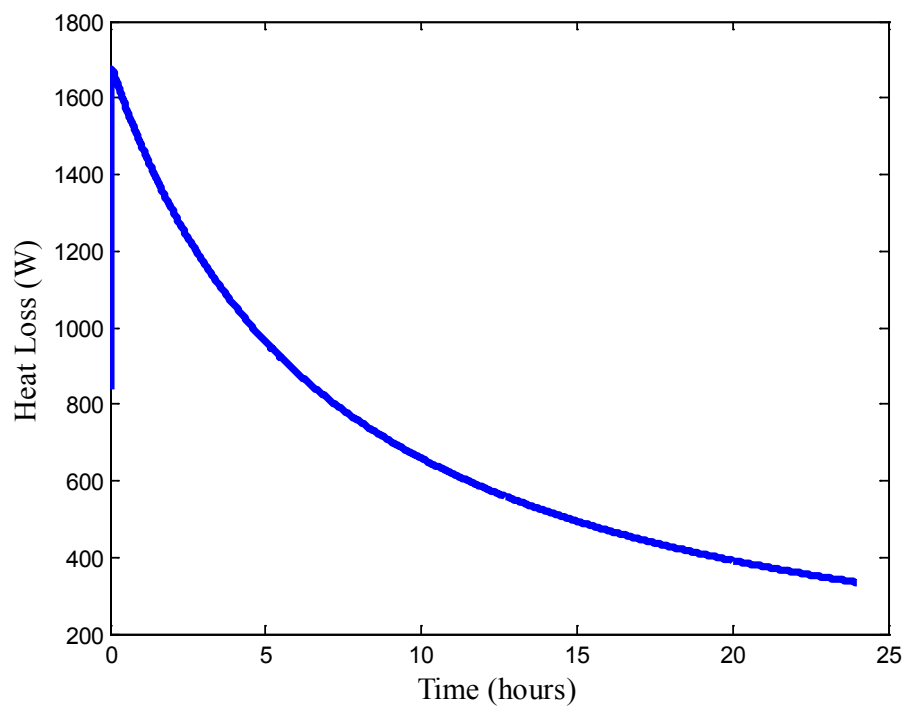


**Figure 8.4: Heat loss rate through radiation shielding**

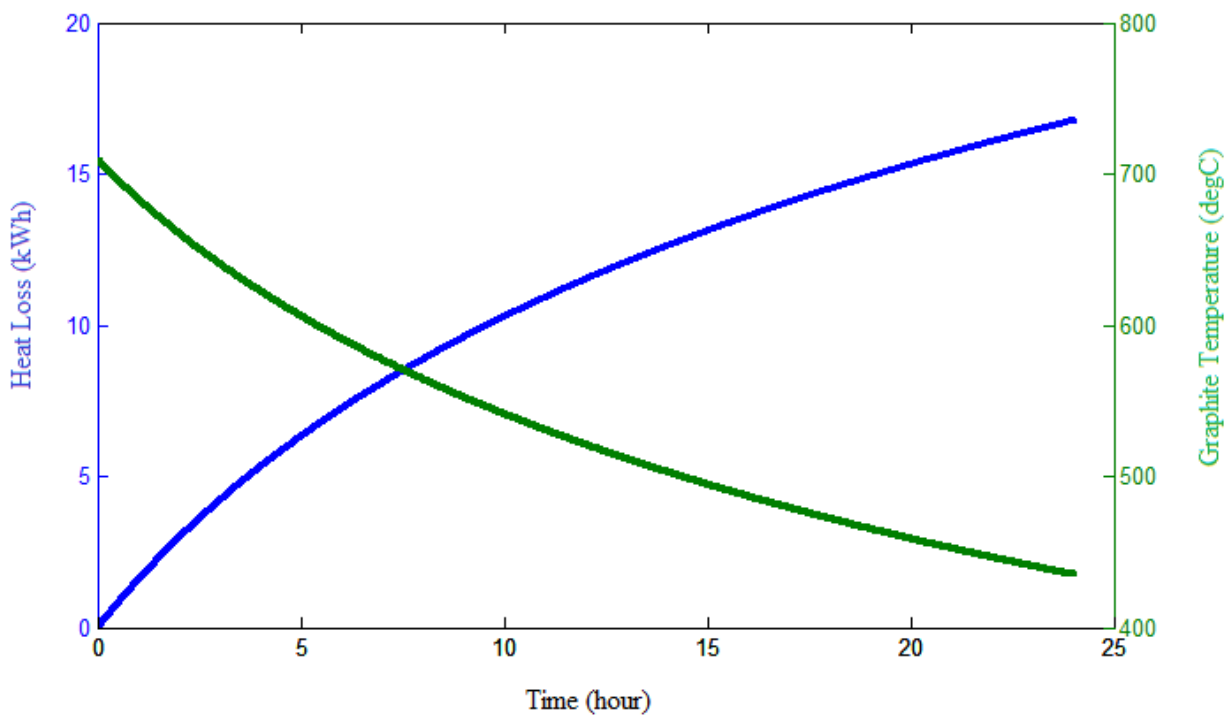


**Figure 8.5: Total heat loss and graphite temperature during a 24-hour cooling period**

As expected, figure 8.4 shows an exponential decay of the heat loss rate. With the initial temperature being the highest, the heat loss rate is also maximum at the beginning of the cooling and approaches zero as the temperature approaches ambient. Only 24 hours of cooling were simulated which was not sufficient time for thermal equilibrium to be reached. Figure 8.5 shows the total heat lost since the beginning of the cooling period and the temperature of the graphite block. The plot indicates that after a 24-hour cooling period, the heat storage will have lost 16.77 kWh of heat, which corresponds to 67% of its design capacity of 25 kWh. However, during typical operation, the cooling cycle would only last 18 hours before charging would begin once again. At 18 hours of cooling, the total heat lost is 14.5 kWh corresponding to 58% of the design capacity.

The temperature curve, plotted on the right vertical axis, indicates that the graphite drops from 710 °C to 435 °C over a 24-hour period. Over an 18-hour period, the graphite cools to 472 °C. Consequently, even after a typical 18-hour cooling period, the heat storage could still provide power to the Stirling engine because the temperature of the heat storage would still be above the stall temperature of 300 °C.

This proposed design had 2 sheets of aluminum as radiation shielding. Adding more layers of aluminum sheet would further reduce the heat loss. The radiation heat transfer between two large parallel plates of equal emissivities with no shielding between them is (Cengel & Boles, 2009)

$$\dot{Q} = \frac{A\sigma(T_1^4 - T_2^4)}{\left(\frac{1}{\varepsilon} + \frac{1}{\varepsilon} - 1\right)} \quad (8.36)$$

The radiation heat transfer between two large parallel surfaces with  $N$  layers of shielding of equal emissivities between them is given by (Cengel & Boles, 2009)

$$\dot{Q} = \frac{A\sigma(T_1^4 - T_2^4)}{(N + 1) \left( \frac{1}{\varepsilon} + \frac{1}{\varepsilon} - 1 \right)} \quad (8.37)$$

Therefore, the radiation heat transfer between two large parallel surfaces with  $N$  layers of shielding is related to that with no shielding by a factor of  $1/(N+1)$ . Therefore with  $N = 2$ , as simulated in the program, the heat loss rate is reduced to 33% of what it would be with no shielding at any given time during the cooling period.

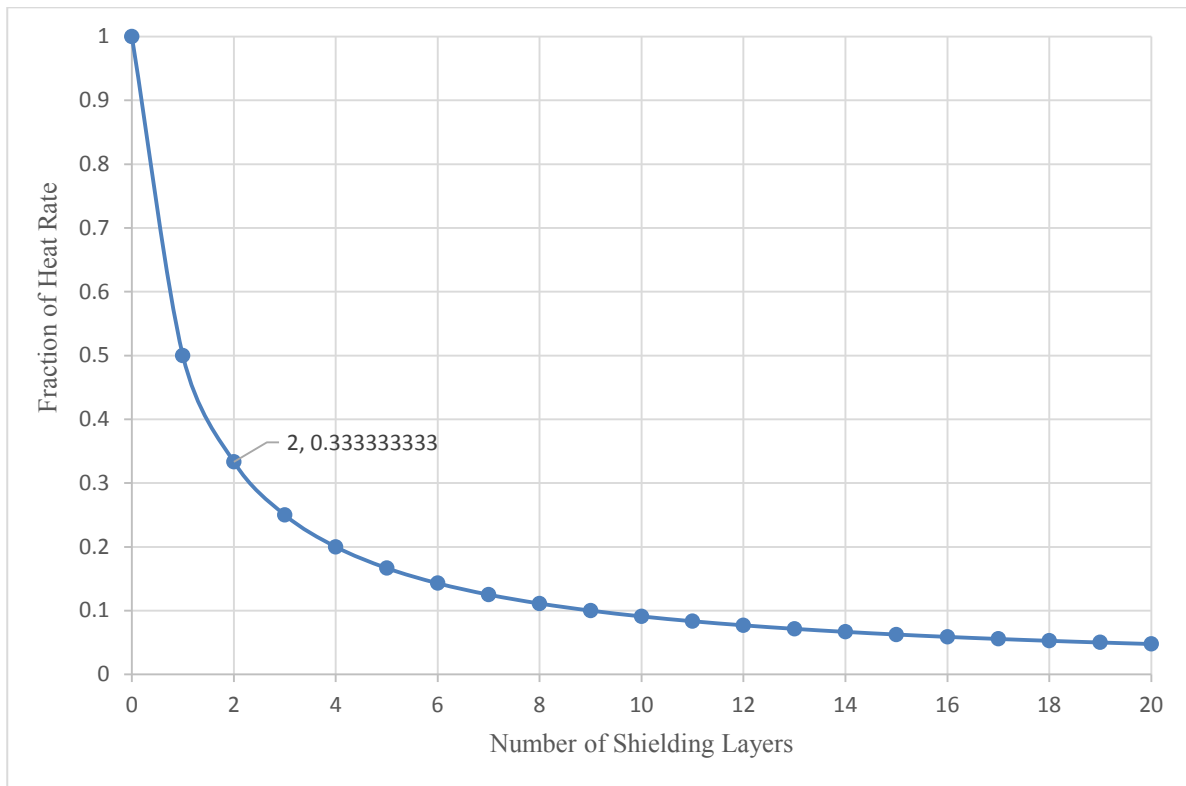


**Figure 8.6: Fraction of heat rate between two large parallel surfaces with multiple layers of radiation shields between them**

The asymptotic curve indicates that adding more shielding layers would decrease the heat loss but doing so may not justify the added complexity and cost. Beyond three layers, the added resistance is small. In this simulation, two layers were chosen because of the geometry of the construction of the frame and casing. They are built such that only two layers of shielding could be conveniently fixed to them without increasing the complexity of the frame's structure. In addition, 2 layers of shielding seems to be a good compromise between heat rate reduction and cost.

### **8.3 Receiver Design**

The receiver is the surface on the graphite on which the concentrated solar radiation is incident. The design of the receiver will ultimately affect the efficiency of the heat storage by affecting the amount of solar radiation absorbed, reflected and re-emitted. Naturally, it is desirable to maximize the amount absorbed and minimize the amount reflected and re-emitted. In addition, it must have two modes; open for absorption during charging, and closed for heat retention during idle periods. The receiver consists essentially of the absorbing surface of the graphite and the window that allows the solar radiation to pass while maintaining the vacuum. A section view of the proposed design is shown in figure 8.7

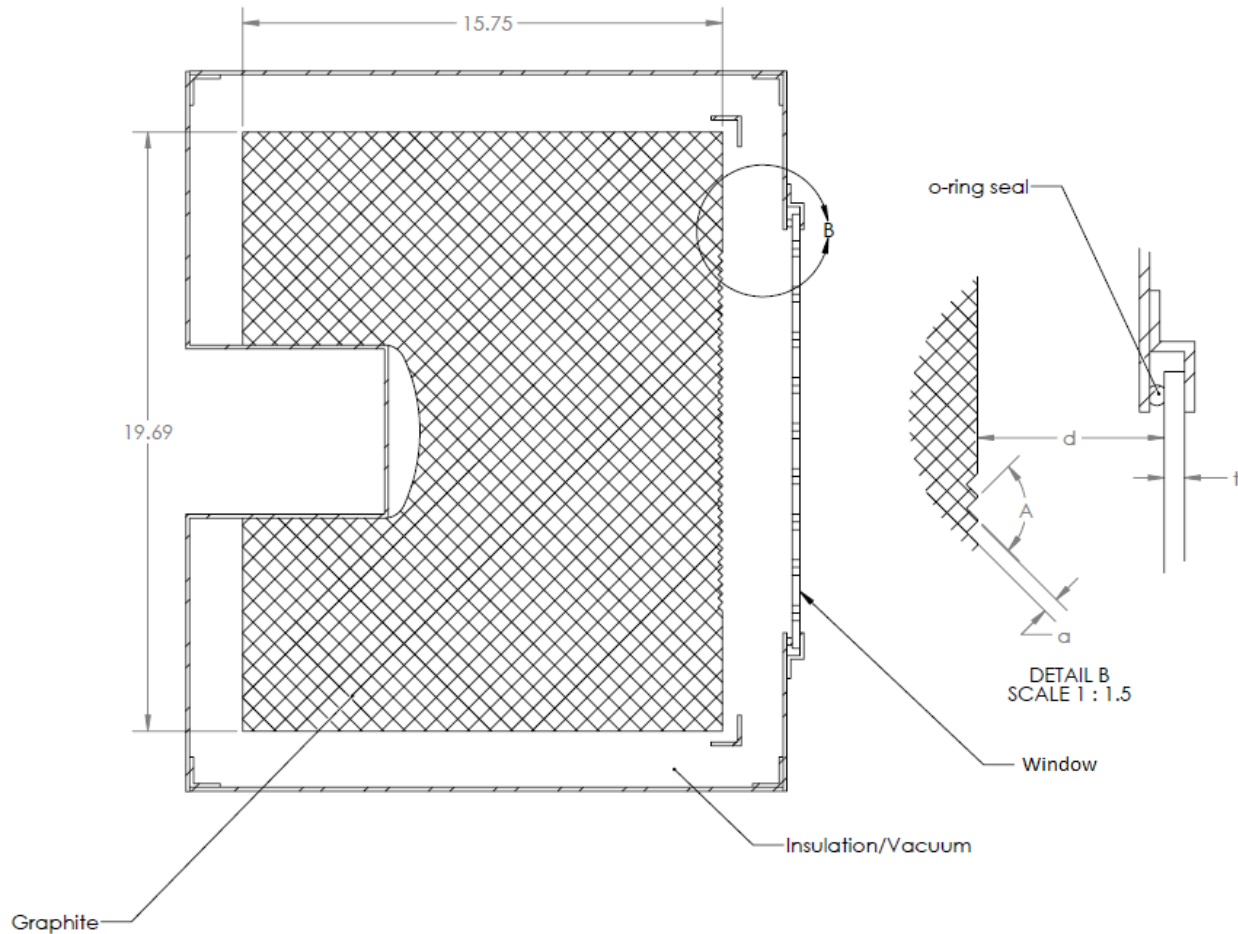


**Figure 8.7: Mid-plane section view of the heat storage**

We will begin the analysis of the receiver design with the interaction between incident solar radiation and the surface of the graphite. Unfortunately, the spectral absorptivity and emissivity as a function of wavelength and temperature of any surface are always equal.

$$\varepsilon(\lambda, T) = \alpha(\lambda, T) \quad (8.38)$$

This means that a surface cannot have high absorption of radiation of a certain wavelength while having a low emission of the same wavelength, which is exactly what is desired. However, the

incident radiation and the emitted radiation are not of the same wavelength. The incident radiation is solar radiation and thus has the solar spectrum of wavelengths. The emitted radiation depends on the graphite emission spectrum for a given temperature. Therefore, a surface can potentially be made to preferentially absorb solar radiation while minimizing re-emission in the infrared range. This can be done by having a surface that has a high emissivity over the solar spectrum and a low emissivity over all other wavelengths that are outside the solar spectrum.

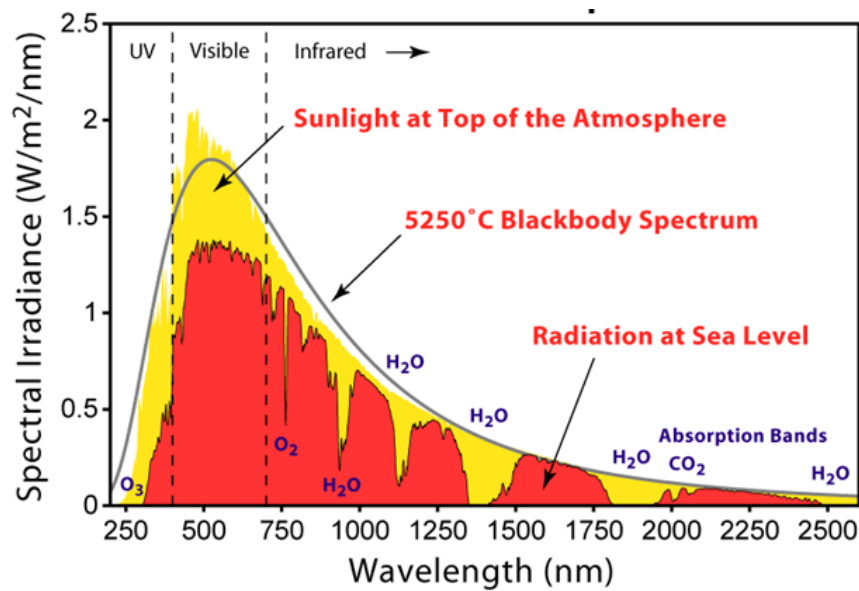


**Figure 8.8: Solar Radiation Spectrum (Wikimedia Commons, n.d.)**

As can be seen from figure 8.8, the majority of the solar irradiance is in the visible range of wavelengths. The effective radiation temperature of the solar spectrum is 5778 K (Williams, 2016). The emissivity of the graphite depends on the wavelength as well as the temperature. However, the spectral emissivity of this particular type of graphite is unknown. For this reason, its spectral emissivity will be treated as that of a blackbody. As will become apparent as the

discussion progresses, this approximation, although far from accurate, still leads to a useful result. The spectral emissivity of a blackbody is given by Planck's law.

$$I(\lambda, T) = \frac{2\pi hc^2}{\lambda^5} \frac{1}{e^{\frac{hc}{\lambda kT}} - 1} \quad (8.39)$$

The graphite is expected to vary in temperature between 300 °C and 700 °C. Using Planck's law, the spectral emissivity of a blackbody is plotted between these temperatures in figure 8.9. As can be seen, the peak emissivities at different temperatures occur at wavelengths of approximately 3000 nm, which is in the infrared range. The peak shifts towards shorter wavelengths at higher temperatures. Although the radiation intensity from the graphite will not be as high as that of a blackbody, the range of wavelengths at which the maximum intensity occurs is approximately the same. Comparing this result to the solar spectral irradiance, we can see that it has a peak in the visible range of wavelengths.

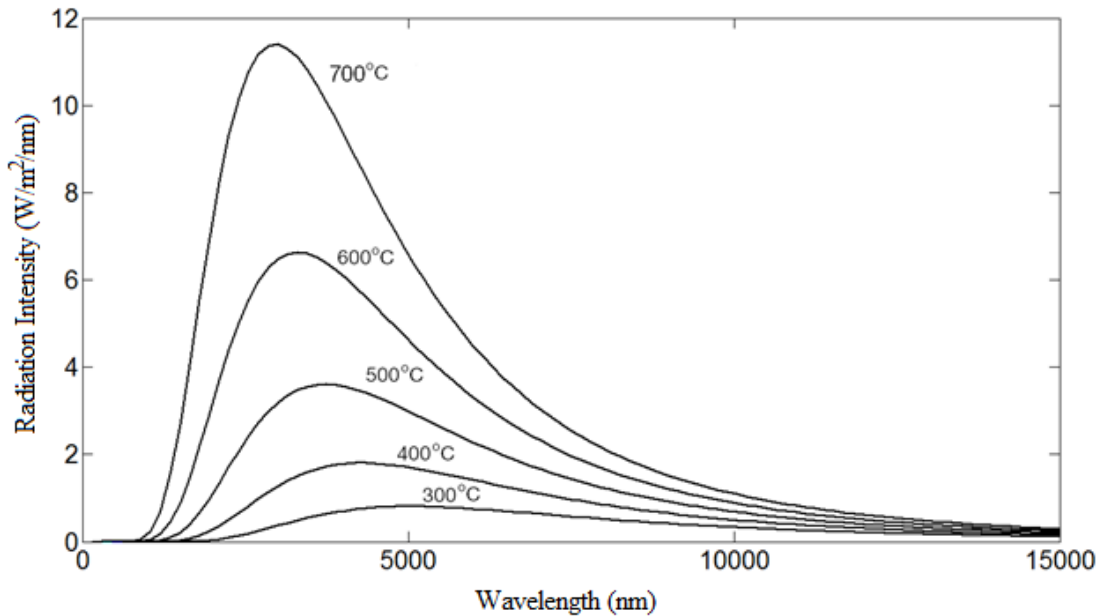


**Figure 8.9: Blackbody spectral intensity**

In the range of operating temperatures, the graphite is thus a poor absorber of visible wavelengths and a good emitter of infrared wavelengths, which is precisely the opposite of what is desired. Although, a large fraction of the total solar irradiance is in the infrared range, the intensity falls close to zero at wavelengths above 2500 nm. Lacking the spectral emissivity of graphite, to quantify this process with reasonable accuracy is not possible. Suffice to say that the graphite will preferentially emit radiation rather than absorb it due to the difference in peak wavelengths between the solar spectrum and the graphite spectrum.

Without any known method of shifting the peak radiation intensity of the graphite towards the visible range, the only way to maximize the amount of absorbed solar radiation is to make it behave as much as possible like a blackbody. This can be accomplished by having grooves on the surface of the graphite as shown in figure 8.7. These grooves increase the fraction of the radiosity from the surface of the graphite that is incident on itself. In other words, some fraction of the re-radiated and reflected radiation is incident on itself due to the concave geometry. A smaller angle  $A$  will increase this fraction but would increase the cost of manufacturing.

As for the window, it is desirable that it allows the entire solar spectrum into the heat storage while minimizing the amount of re-radiated and reflected radiation out of the heat storage. Unfortunately, there is no such surface that treats transmitted radiation in one direction differently than in another direction. There is no true “one-way” glass. Therefore, regardless of the transmissivity of the window, the ratio of radiation leaving the heat storage through the glass to that entering through the window remains constant. It is then desirable to have a window with maximum transmissivity over the infrared range in order to maximize the amount of radiation entering the heat storage. Since the graphite does not absorb visible light, the window need not necessarily transmit it. The window may in fact be visually opaque. Standard glass is not a

suitable material for the window since it is opaque to infrared radiation. A window made of silicon is probably the best choice due to its high infrared transmissivity and its ability to withstand high temperatures. Although its transmissivity is still somewhat low. A 2.2 mm thick high transmission silicon for IR optical applications produced by *Topsil* has an average transmissivity of 52% between 2500 nm and 7500 nm (Jensen, 2013). Thinner sheets will have higher transmissivity but the sheet must be thick enough to sustain the stresses caused by the vacuum.

## **Chapter 9: Results and Discussion**

To re-iterate, the goal of this research was to evaluate the feasibility of an inexpensive, residential scale, high temperature, graphite based sensible heat storage for use as part of a CSP system. More specifically, the performance and durability of such a device were tested. It should be noted that the results of these tests apply only to the design specifications of the designed proposed in appendix B. Some design changes could be made to improve the performance and durability but doing so would be in conflict with the goal of keeping it inexpensive. Of course, the feasibility of this type of heat storage depends not only on performance and durability but also on cost. Having only a very rough estimate of the cost, evaluating the feasibility is difficult. That being said, the targeted cost of the device was initially set to 500 \$USD so this value will be assumed as the actual cost even though it may be much more.

### **9.1 Durability**

One of the two aspects of durability that was tested was oxidation resistance of the graphite at high temperatures. Of the five different methods (SiC coating, Al<sub>2</sub>O<sub>3</sub> coating, CO<sub>2</sub> gas blanketing, argon gas blanketing, evacuation) that were tested, argon gas blanketing produced the best effective lifespan of 31 years. Assuming a cost of 500\$ for the device, this translates to 16 \$/year which is very inexpensive. However, as explained in section 5.3 the effective lifespan obtained from evacuation should be as good or better than argon blanketing as long as the pressure inside the casing is kept low enough, which was not the case during the test. Evacuation has two major advantages over argon blanketing. Firstly, it eliminates the need for insulation since heat cannot be conducted through a vacuum. Secondly, the pressure inside the casing would vary much less as the temperature increases. Having argon enclosed in the casing would

cause greater dynamic pressure stresses on the casing requiring a heavier, more costly casing. For these two reasons, evacuation is the preferred option.

The other aspect of durability that was tested was resistance to vibration. Although only one frequency and type of contact was tested, we can safely say that graphite is not susceptible to degradation by vibration due to contact with a reciprocating engine. Critical mechanical failure due to resonance is also not possible in the expected range of engine speeds.

## **9.2 Performance**

The discharging curves of figures 6.2 and 6.3 suggest that the heat transfer fluid flow rate in the engine will have little effect on the discharging rate. Furthermore, if the engine is a Stirling engine, then the heat transfer fluid flow rate depends on the discharging rate. The engine speed, power output and HTF flow rate are directly proportional to the discharging heat rate. Ideally, we would like the power output of the engine to match the demand of the users, but with the current design, the power output curve can only follow the discharge curve.

This means that when discharging immediately after a full charge, the power output of the engine will exceed the users demand. This will result in wasted heat. Then as the graphite cools, the power output of the engine will be less than the users demand. For the actual system, the discharging curve will not be as pronounced as the one obtained from the test due to the fact that the temperature difference between the HTF in the engine and the heat storage will be much smaller than during the test. During the test, the HTF in the heat sink was water entering at 15 °C while in the engine, it will be most likely helium at approximately 300 °C. Therefore, the slope of the curve would be smaller but the power output would still be excessive at first and lacking near the end.

To solve this problem, a control system governing an actuator that would insert or retract the engine head from the cavity in the storage is suggested. The functioning would be as follows. At the beginning of the discharge, the engine head would only be slightly inserted into the cavity such that the contact area and heat rate would be just enough to meet the demand. Then as the graphite cools, more contact area would be needed to maintain the same heat rate and so the actuator would insert the engine head deeper into the cavity. This control system would of course increase the cost of the heat storage.

The charging efficiency  $\eta_c$  was found to be 40.2% and the discharging efficiency  $\eta_d$  was found to be 85% resulting in an overall efficiency of 34.2%. These values are not entirely representative of the heat storage for a few reasons. Firstly, the charging efficiency depends not only on the heat storage but also on the solar concentrator which was not part of this research. The charging efficiency was measured by simulating the anticipated input heat flux but in doing so we determine the charging efficiency of the entire system. This heat storage could be used with any solar concentrator with any concentration factor which would lead to different charging efficiencies.

Second, the discharging efficiency was dependent on the heat sink as well, which was meant to simulate the anticipated conditions of the engine. Again, this heat storage could be used with any heat engine resulting in different discharging efficiencies. So, the overall efficiency is a measure of the heat storage but it is dependent on the entire CSP system. If we would like to know the efficiency of the entire system including the concentrator, heat storage, the engine and the generator, then the efficiencies of each of these components must be considered.

## Chapter 10: Conclusion and Recommendations

### 10.1 Conclusion

The tested aspects of the durability of the heat storage proved to be far beyond what would be considered acceptable or feasible for cost effective production. At 700 °C, the silicon carbide based coating yielded an effective lifespan of 65 hours while the best result for the aluminum oxide based coating yielded 93 hours. Inert gas blanketing with argon yielded the best effective lifespan of 34454 hours while CO<sub>2</sub> blanketing and evacuation at -12.4 psi (85.5 kPa) yielded 27562 hours and 317 hours respectively for the high grade graphite. Repeated cycles of heating and cooling had no apparent effect on the oxidation rate.

For the discharge power test, the high grade graphite operating with a dimensionless number  $II = 2.46$  discharged 606 W/kg at 500 °C and 202 W/kg at 300 °C. For the low grade graphite, it discharged 603 W/kg and 276 W/kg at 500 °C and 300 °C respectively. Varying the dimensionless number had very little effect, indicating that the limiting factor was conduction through the graphite and not convection in the heat sink.

The discharging efficiency  $\eta_d$  was 85% for the high grade and 97% for the low grade graphite. The charging efficiency  $\eta_c$  obtained by simulating charging by solar radiation was found to be 40.2% for the high grade graphite. With an overall efficiency for the heat storage alone of 34.2% for the high grade graphite and with no means of controlling the power output, the entire CSP system will provide very little useful work if we consider the efficiencies of the other components. Also the maximum temperature obtained during charging is 396 °C which does not meet the objective of 700 °C.

Having determined these quantities, the required mass of graphite for a 25 kWh storage capacity was found to be 152 kg using the same insulation as that on the test apparatus. The program that simulates radiation heat loss through two layers of shielding and an evacuated gap outputs a heat loss of 14.5 kWh over an 18 hour cooling period, corresponding to 58% of the 25kWh capacity.

Vibration testing at 1000 rpm and room temperature has shown no effect on the structural integrity of the graphite. No surface cracks were detected. No fine powder accumulated and no mass loss was measured after 6 hours of exposure to vibration. With an effective lifespan of 31 years for oxidation and virtually indefinitely for vibration, the cost of the heat storage is justified. However, resistance to vibration at high temperatures was not investigated. Doing so would be prudent.

## **10.2 Recommendations to Overcome the Limitations**

It should be noted that all measured values were obtained from scaled down models of the actual heat storage and that each of these models only consisted of the components that were critical to the quantity being investigated. While the dimensionless number approach was implemented to make the results valid for any scale, there were many factors that could not be controlled and accounted for. For this reason, it is recommended that a full-scale prototype be built and tested. The results could be very different.

The measured efficiency was obtained from a scaled down model of the heat storage that was insulated with ceramic fiber board. If the insulation had been replaced with an evacuated casing and some radiation shielding as proposed in the design, the efficiency could have been much higher. Since the insulation method has the strongest influence on the efficiency, it is highly

recommended that it be replaced with the evacuated casing and radiation shielding. This method should also be tested for feasibility on a full-scale prototype. Some foreseeable problems are air infiltrating into the casing and the inability to obtain a low enough pressure at a reasonable cost.

It is recommended that a thermochemical heat storage be considered. Sensible heat storages, such as this one, inherently require a large amount of insulation because it must be kept at high temperatures. Heat retention in thermochemical heat storages is simply a matter of keeping the reactants separate without the need for any insulation. As long as the reacting agents are kept separate from each other, the energy can be stored indefinitely without any losses.

Another major advantage of thermochemical heat storage is the high energy density. For the same capacity, a thermochemical heat storage would be much smaller and lighter than a sensible heat storage. As calculated, the mass of graphite required for a 25 kWh capacity is 152 kg which is somewhat excessive for convenience.

The vibration testing did not take into account the effects of high temperatures on vibration resistance. Performing the same vibration test at 700 °C may have different results. Doing so would be wise since the heat storage is expected to reach this temperature.

### **10.3 Future Research Work**

All the tests were conducted on two types of graphite from a single supplier. However, the results depend on the microstructure and production method of the graphite. Therefore, further research into the relationship between durability, performance and graphite microstructure should be considered.

Also, the maximum allowable pressure to prevent heat transfer by conduction of 0.035 Pa obtained analytically should be compared to empirical results. The relationship between air pressure and thermal conductivity should be established.

#### **10.4 Contributions**

The two major contributions that are the product of this work are the figures 6.2 and 6.3 and the design drawings shown in appendix B. The partnered company can make use of these figures and drawings as instructions to proceed with the production of a heat storage prototype. In addition, figures 6.2 and 6.3 can be used as a reference for any research and development project aimed at producing a graphite based TES.

This thesis has analyzed the feasibility of using graphite as a sensible heat storage material and has established the material and design requirements of such a device. Although the feasibility also depends on cost, which was not evaluated in depth, this thesis has shown that graphite is in fact effective as a heat storage material but requires a large mass and very thick insulation. Whether the material and design requirements are cost effective has yet to be determined and compared to other types of heat storage. This thesis has shown that for unelectrified regions of the world, graphite based heat storages can provide a simple and inexpensive way of storing solar heat for use as heat or as input to a heat engine.

## References

- Agrafiotis, C., Roeb, M., Schmucker, M., & Sattler, C. (2015). Exploitation of Thermochemical Cycles Based on Solid Oxide Redox Systems for Thermochemical Storage of Solar Heat. Part 2: Redox Oxide-coated Porous Ceramic Structures as Integrated Thermochemical Reactors/Heat Exchangers. *Solar Energy*, *114*, 440-458.
- Anastasovski, A. (2017). Design of Heat Storage Units for use in repeatable Time Slices. *Applied Thermal Engineering*, *112*, 1590-1600.
- Bartl, J., & Baranek, M. (2004). Emissivity of Aluminum and its Importance for Radiometric Measurement. *Measurements of Physical Quantities*, *4*, 31-36
- Beltran, J. I., Wang, J., Montero-Chacon, F., & Cui, Y. (2017). Thermodynamic Modelling of Nitrate Materials for Hybrid Thermal Energy Storage: Using Latent and Sensible Mechanisms. *Solar Energy*, *155*, 154-166.
- Cengel, Y., & Boles, M. (2004). *Thermodynamics, An Engineering Approach, 5th Edition*. McGraw-Hill.
- Cengel, Y., & Boles, M. (2009). *Heat and Mass Transfer A Practical Approach*. McGraw-Hill.
- CERAM Research. (2016). <http://www.azom.com/article.aspx?ArticleID=1630>. Retrieved from azom.com: <http://www.azom.com/article.aspx?ArticleID=1630>
- Colbert, M., Ribeiro, F., & Treglia, G. (2014). Atomistic Study of Porosity Impact on Phonon Driven Thermal Conductivity. *Journal of Applied Physics*, *115*, 034902 - 034902.10

- Criado, Y., Alonso, M., & Anxionnaz-Minvielle, Z. (2014). Conceptual Process Design of a CaO/Ca(OH)<sub>2</sub> Thermochemical Energy Storage System Using Fluidized Bed Reactors. *Applied Thermal Engineering*, 73 (1), 1087 - 1094
- Dayan, J., Lynn, S., & Foss, A. (1979). Evaluation of a Sulfur Oxide Chemical Heat Storage Process for a Steam Solar Electric Plant. *U.S. Department of Energy*.
- De Luca, F., Ferraro, V., & Marinelli, V. (2015). On the Performance of CSP Oil-Cooled Plants, With and Without Heat Storage in Tanks of Molten Salts. *Energy*, 230-239.
- Dincer, I., & Rosen, M. A. (2011). *Thermal Energy Storage Systems and Applications*. Chichester: Wiley.
- energyplus.net*. (2016). (World Meteorological Organization) Retrieved 2016, from <https://energyplus.net/weather>
- Entegris Inc. (2013). *Properties and Characteristics of Graphite*. Billerica: Entegris, Inc.
- Frazzica, A., Manzan, M., Sapienza, A., Freni, A., Toniato, G., & Restuccia, G. (2016). Experimental Testing of a Hybrid Sensible-Latent Heat System for Domestic Hot Water Applications. *Applied Energy*, 183, 1157-1167.
- Halikia, I., Zoumpoulakis, L., Christodoulou, E., & Prattis, D. (2001). Kinetic Study of the Thermal Decomposition of Calcium Carbonate by Isothermal Methods of Analysis. *The European Journal of Mineral Processing and Environmental Protection*, 1, 89 - 102
- Hawes, D. W. (1991). *Latent Heat Storage in Concrete*. Thesis (M.A.Sc.), Montreal: Concordia University.

Herrmann, U., Kelly, B., & Price, H. (2004). Two-Tank Molten Salt Storage for Parabolic Trough Solar Power Plants. *Energy*, 29 (5/6), 883 - 893

<http://graphiteenergy.com/graphite.php>. (n.d.). Retrieved from graphiteenergy.com:

<http://graphiteenergy.com/graphite.php>

IEA-ETSAP and IRENA. (2013). *Thermal Energy Storage Technology Brief*. IEA-ETSAP and IRENA.

*International Energy Agency*. (2017, 06 15). Retrieved from International Energy Agency:

<https://www.iea.org/statistics/monthlystatistics/monthlyelectricitystatistics/>

Jensen, L. (2013). *topsil.com*. Retrieved 02 07, 2017, from

[http://www.topsil.com/media/123122/hitran\\_application\\_note\\_october2013.pdf](http://www.topsil.com/media/123122/hitran_application_note_october2013.pdf)

Jessup, R. S. (1938). *Heats of Combustion of Diamond and Graphite*. US National Bureau of Standards.

Johansen, J. B., Englmaier, G., Dannemand, M., Kong, W., Fan, J., Dragsted, J., . . . Furbo, S.

(2016). Laboratory testing of Solar Combi System with Compact Long Term PCM Heat Storage. *Energy Procedia*, 91, 330-337.

Kalaiselvam, S. (2014). *Thermal Energy Storage Technologies for Sustainability*. Oxford: Elsevier.

Karim Lee, A. (2014). *Application of PCM to Shift and Shave Peak Demand: Parametric Studies*. Thesis (M.A.Sc.), Montreal: Concordia University.

- Khalifa, A., Tan, L., Mahoney, D., Date, A., & Akbarzadeh, A. (2016). Numerical Analysis of Latent Heat Thermal Energy Storage Using Miniature Heat Pipes: A Potential Enhancement for CSP Plant Development. *Applied Thermal Engineering*, 108, 93-103.
- Liu, F., Wang, J., & Qian, X. (2017). Integrating Phase Change Materials Into Concrete Through Microencapsulation Using Cenospheres. *Cement and Concrete Composites*, 80, 317-325.
- Lovegrove, K., & Luzzi, A. (1996). Endothermic Reactors for an Ammonia Based Thermo-Chemical Solar Energy Storage and Transport System. *Solar Energy*, 76, 361-371.
- Ma, Z., Yang, W.-W., Yuan, F., Jin, B., & He, Y.-L. (2017). Investigation on the Thermal Performance of a High-Temperature Latent Heat Storage System. *Applied Thermal Engineering*, 122, 579-592.
- Merriam-Webster Dictionary. (2016). <http://www.merriam-webster.com/dictionary/sensible%20heat>. Retrieved from [www.merriam-webster.com](http://www.merriam-webster.com).
- Mikron Instrument Company. (2016). Retrieved from [http://www-eng.lbl.gov/~dw/projects/DW4229\\_LHC\\_detector\\_analysis/calculations/emissivity2.pdf](http://www-eng.lbl.gov/~dw/projects/DW4229_LHC_detector_analysis/calculations/emissivity2.pdf)
- Miliozzi, A., Liberatore, R., Creszenzi, T., & Veca, E. (2015). Experimental Analysis of Heat Transfer in Passive Latent Heat Thermal Energy Storage Systems for CSP Plants. *Energy Procedia*, 82, 730-736.
- Mira-Hernandez, C. F., & Garimella, S. (2014). Numerical Simulation of Single and Dual Media Thermocline Tanks for Energy Storage in Concentrating Solar Power Plants. *Energy Procedia*, 49, 916-926.

- Mostafavi, S. S., Taylor, R. A., Nithyanandam, K., & Shafiei Ghazani, A. (2017). Annual Comparative Performance and Cost Analysis of High Temperature, Sensible Thermal Energy Storage Systems Integrated with a Concentrated Solar Power Plant. *Solar Energy*, *153*, 153-172.
- Nepustil, U., Laing-Nepustil, D., Lodemann, D., Sivabalan, R., & Hausmann, V. (2016). High Temperature Latent Heat Storage with Direct Electrical Charging - Second Generation Design. *Energy Procedia*, *99*, 314-320.
- N'Tsoukpoe, K. E., Osterland, T., Opel, O., & Ruck, W. K. (2016). Cascade Thermochemical Storage with Internal Condensation Heat Recovery for Better Energy and Exergy Efficiencies. *Applied Energy*, *181*, 562-574.
- Obermeier, J., Sakellariou, K., Tsongidis, N., Baciú, D., Charalambopoulou, G., Steriotis, T., . . . Arlt, W. (2017). Material Development and Assessment of an Energy Storage Concept Based on the CaO-looping Process. *Solar Energy*, *150*, 298-309.
- Page, D. (1991). *The Industrial Graphite Engineering Handbook*. Cornell University: UCAR Carbon Co.
- Paksoy, H. O. (2007). *Thermal Energy Storage for Sustainable Energy Consumption: Fundamentals, Case Studies and Design*. Adana: NATA Science Series.
- Pan, Z., & Zhao, C. (2017). Gas-Solid Thermochemical Heat Storage Reactors for High-Temperature Applications. *Energy*, *130*, 155-173.
- Parker, R., & Jenkins, C. (1961). A Flash Method of Determining Thermal Diffusivity, Heat Capacity, and Thermal Conductivity. *Journal of Applied Physics*, *32* (9), 1679-1684.

- Paskevicius, M., Sheppard, K., Williamson, C., & Buckley, C. (2015). Metal Hydride Thermal Heat Storage Prototype for Concentrating Solar Thermal Power. *Energy*, 88, 469-477.
- Renewable Energy and Climate Change Program, SAIC Canada. (2013). *Compact Thermal Energy Technology Assessment Report*. Ottawa.
- Sakellariou, K. G., Karagiannakis, G., Criado, Y. A., & Konstandopoulos, A. G. (2015). Calcium Oxide Based Materials for Thermochemical Heat Storage in Concentrated Solar Power Plants. *Solar Energy*, 122, 215-230.
- Scalat, S. G. (1996). *Full Scale Thermal Performance of Latent Heat Storage in PCM Wallboard*. Thesis (M.A.Sc), Montreal: Concordia University.
- Schmidt, M., Robkopf, C., Afflerbach, S., Gortz, B., Kowald, T., Linder, M., & Trettin, R. (2015). Investigations of Nano-Coated Calcium Hydroxide Cycled in a Thermochemical Heat Storage. *Energy Conservation and Management*, 97, 94-102.
- Schroeder, D. (2000). *An Introduction to Thermal Physics* (p. 28). San Francisco: Addison Wesley Longman.
- Strohle, S., Haselbacher, A., Jovanovic, Z., & Steinfeld, A. (2017). Upgrading Sensible-Heat Storage with a Thermochemical Storage Section Operated at Variable Pressure: An Effective Way Toward Active Control of the Heat-Transfer Fluid Outflow Temperature. *Applied Energy*, 196, 51-61.
- Tao, Y., Lin, C., & He, Y. (2015). Preparation and Thermal Properties Characterization of Carbonate Salt/Carbon Nanomaterial Composite Phase Change Material. *Energy Conversion and Management*, 97, 103-110.

- Tescari, S., Agrafiotis, C., Breuer, S., de Oliviera, L., Puttkamer, M., Roeb, M., & Sattler, C. (2014). Thermochemical Solar Energy Storage Via Redox Oxides: Materials and Reactor/Heat Exchanger Concepts. *Proceedings of the SolarPACES 2013 International Conference, 49*, 1034-1043.
- Tiskatine, R., Oaddi, R., Ait El Cadi, R., Bazgaou, A., Bouirden, L., Aharoune, A., & Ihlal, A. (2017). Suitability and Characteristics of Rocks for Sensible Heat Storage in CSP Plants. *Solar Energy Materials and Solar Cells, 169*, 245-257.
- UCAR Carbon Company Inc. (1991). Typical Room-Temperature Properties of Graphite. In *The Industrial Graphite Engineering Handbook* (p. 4.06).
- Vincenti, W., & Kruger, C. (1967). *Introduction to Physical Gas Dynamics*. Malabar, Krieger Publishing Company.
- Wikimedia Commons*. (2017). Retrieved January 30, 2017, from [https://commons.wikimedia.org/wiki/File:Solar\\_Spectrum.png](https://commons.wikimedia.org/wiki/File:Solar_Spectrum.png)
- Williams, D. R. (2016). *Sun Fact Sheet*. Retrieved from NASA Goddard Space Flight Center: <https://nssdc.gsfc.nasa.gov/planetary/factsheet/sunfact.html>
- World Energy Outlook. (2016). *International Energy Agency*. Retrieved 02 11, 2017, from <http://www.worldenergyoutlook.org/resources/energydevelopment/energyaccessdatabase/>
- Yan, J., Zhao, C., & Pan, Z. (2017). The Effect of CO<sub>2</sub> on Ca(OH)<sub>2</sub> and Mg(OH)<sub>2</sub> Thermochemical Heat Storage Systems. *Energy, 124*, 114-123.

Yan, T., Wang, R. Z., Li, T. X., Wang, L., & Ishugah, F. (2015). A Review of Promising Candidate Reactions for Chemical Heat Storage. *Renewable and Sustainable Energy Reviews, 43*, 13-31.

Zauner, C., Hengstberger, F., Morzinger, B., Hofmann, R., & Walter, H. (2017). Experimental Characterization and Simulation of a Hybrid Sensible-Latent Heat Storage. *In Applied Energy, 189*, 506-519.

## Appendix A: Matlab program for radiation shield simulation

```

function [ output_args ] = radshield( input_args )

A1 = 1.3;           %graphite surface area (m2)
A2 = 1.86;         %inner aluminum shield surface area (m2)
A3 = 1.92;         %outer aluminum shield area (m2)
F12 = 1;           % view factor from graphite to inner shield
F23 = 1;           %view factor from inner shield to outer shield
F21 = A1/A2*F12;   %view factor from inner shield to graphite
F32 = A2/A3*F23;   %view factor from outer shield to inner shield
m = 152;           %mass of graphite (kg)
c = 1445;          % specific heat capacity of graphite at average temperature (J/kgK)
sig = 5.67E-8;     % Boltzmann constant

U12 = A1*F12;      %space conductance between graphite and inner shield
U23 = A2*F23;      %space conductance between inner and outer shield

Ucond = 16582;     %conduction conductance through steel casing
Uconv = 9.75;      %convective conductance of ambient air
Urad = 0.176;      %radiative conductance between casing and surroundings
Ueq = ((Ucond^-1+Uconv^-1)^-1 + Urad); %convection/conduction/radiation
equivalent conductance

Tinf = 25+273;     %ambient temperature(K)

dt = 60;           %time step of one minute (seconds)

J1(1) = 50000;     %initial radiosity assumptions (W/m2)
J2(1) = 40000;
Eb2(1) = 35000;
J3(1) = 30000;
J4(1) = 20000;
T1(1) = 710+273;   %initial temperature assumptions (K)
T2(1) = 30+273;
T3(1) = 30+273;
Ts(1) = 25+273;
Ta(1) = 40+273;

for i = 1:1440     %1440 minutes equals 24 hours

    eps1 = 2.77E-5*T1(i) + 0.692; %graphite emissivity
    eps2 = 7.2E-5*Ta(i) + 0.0032; %aluminum emissivity
    eps3 = 7.2E-5*T3(i) + 0.0032;

    U1 = A1*eps1/(1-eps1); %surface conductance of graphite
    U2 = A2*eps2/(1-eps2); %surface conductance of inner shield
    U3 = A3*eps3/(1-eps3); %surface conductance of outer shield

    U_matrix = [-(U1+U12) U12 0 0 0; U12 -(U12+U2) 0 0 U2; 0 U2 U2 0 -2*U2; 0 0 -(U2+U23) U23 U2;
    0 0 U23 -(U23+U3) 0];

    Eb1(i) = sig*(T1(i))^4;
    Eb3(i) = sig*(T3(i))^4;

    Q_vector = [-U1*Eb1(i);0;0;0;-U3*Eb3(i)];
    JE_vector = U_matrix\Q_vector;

    J1(i+1) = JE_vector(1);
    J2(i+1) = JE_vector(2);
    J3(i+1) = JE_vector(3);
    J4(i+1) = JE_vector(4);
    Eb2(i+1) = JE_vector(5);

```

```

Eb1(i+1) = (-(U1+U12)*J1(i+1) + U12*J2(i+1))/-U1;
Eb3(i+1) = (U23*J3(i+1) - (U23+U3)*J4(i+1))/-U3;

T1(i+1) = U1*(J1(i+1)-Eb1(i+1))*dt/m/c + T1(i);
T3(i+1) = U3/Ueq*(J4(i+1)-Eb3(i+1)) + Tinf;
Ta(i+1) = (Eb2(i+1)/sig)^0.25;

timeQ(i) = i/60;
Qdot_loss(i) = U1*(Eb1(i+1) - J1(i+1));           %power loss (W)
Q_loss(i) = sum(Qdot_loss)*dt/1000/3600;          %energy loss (kWh)
time(1) = 0;
time(i+1) = i/60;                                %time in hours for plotting purposes

%Tsurf = (Eb3(i)/sig)^0.25

end

plot(timeQ,Qdot_loss,'LineWidth',3)
xlabel('time (hours)','fontsize',16)
ylabel('heat loss (W)','fontsize',16)
figure

plotyy(timeQ,Q_loss,time,T1-273)

xlabel('time (hours)','fontsize',16)
ylabel('heat loss (kWh)','fontsize',16)

%ylabel('Graphite Temperature (degC)', 'fontsize', 16)

% plot(time,T1,'--','LineWidth',3)
% xlabel('time (hours)','fontsize',16)
% ylabel('graphite temperature (K)','fontsize',16)

```

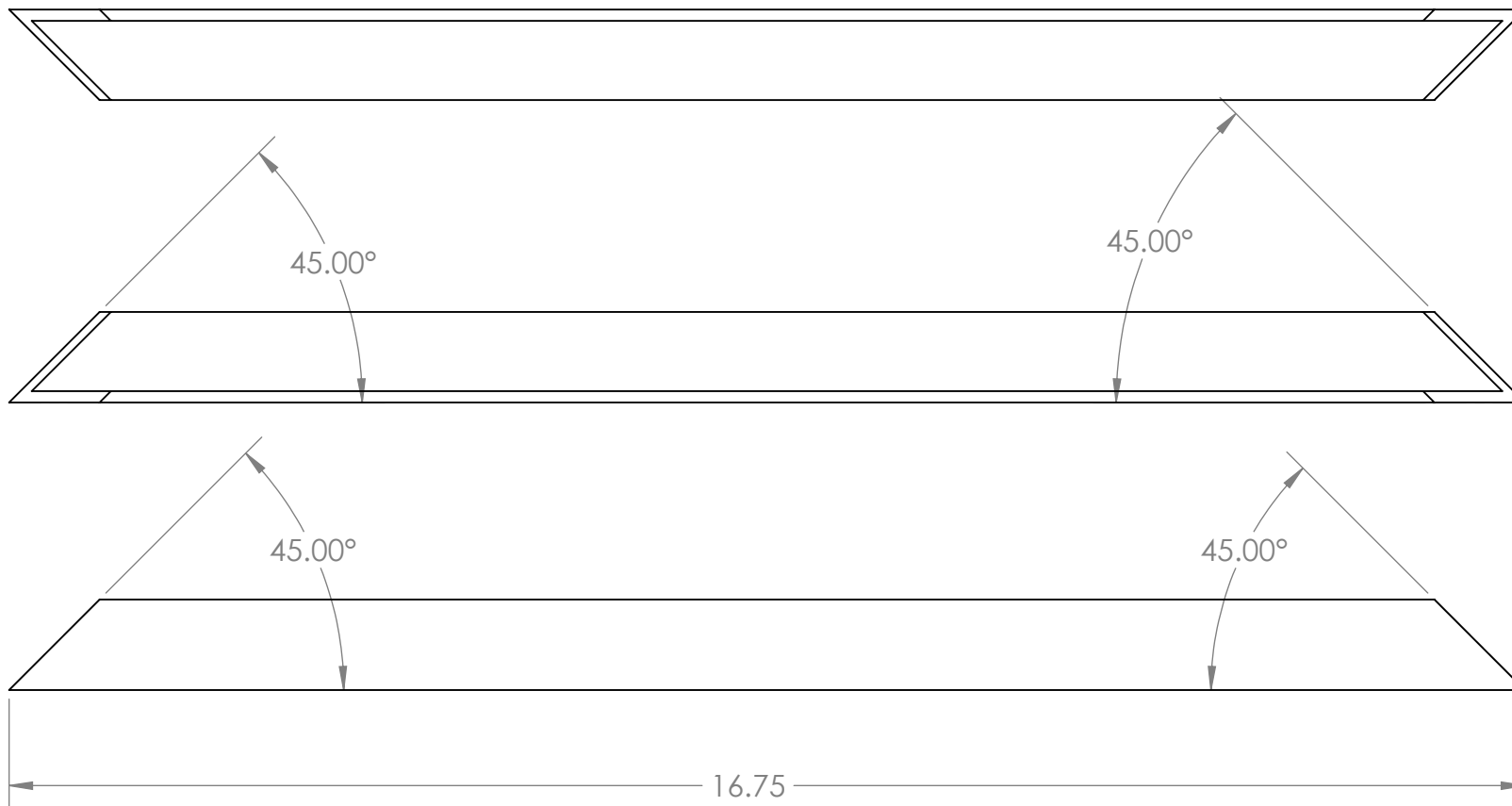
## **Appendix B: Prototype Drawings**

2

1

B

B



A

A

**PROPRIETARY AND CONFIDENTIAL**  
 THE INFORMATION CONTAINED IN THIS DRAWING IS THE SOLE PROPERTY OF <INSERT COMPANY NAME HERE>. ANY REPRODUCTION IN PART OR AS A WHOLE WITHOUT THE WRITTEN PERMISSION OF <INSERT COMPANY NAME HERE> IS PROHIBITED.

		UNLESS OTHERWISE SPECIFIED:		NAME	DATE
		DIMENSIONS ARE IN INCHES	DRAWN	CD	
		TOLERANCES:	CHECKED		
		FRACTIONAL ±	ENG APPR.		
		ANGULAR: MACH ± BEND ±	MFG APPR.		
		TWO PLACE DECIMAL ±	Q.A.		
		THREE PLACE DECIMAL ±	COMMENTS:		
		INTERPRET GEOMETRIC TOLERANCING PER:			
		MATERIAL			
		AISI 1020 steel			
		FINISH			
		as extruded			
NEXT ASSY	USED ON	DO NOT SCALE DRAWING			
APPLICATION					

TITLE:

block support A

SIZE

**A**

DWG. NO.

1

REV

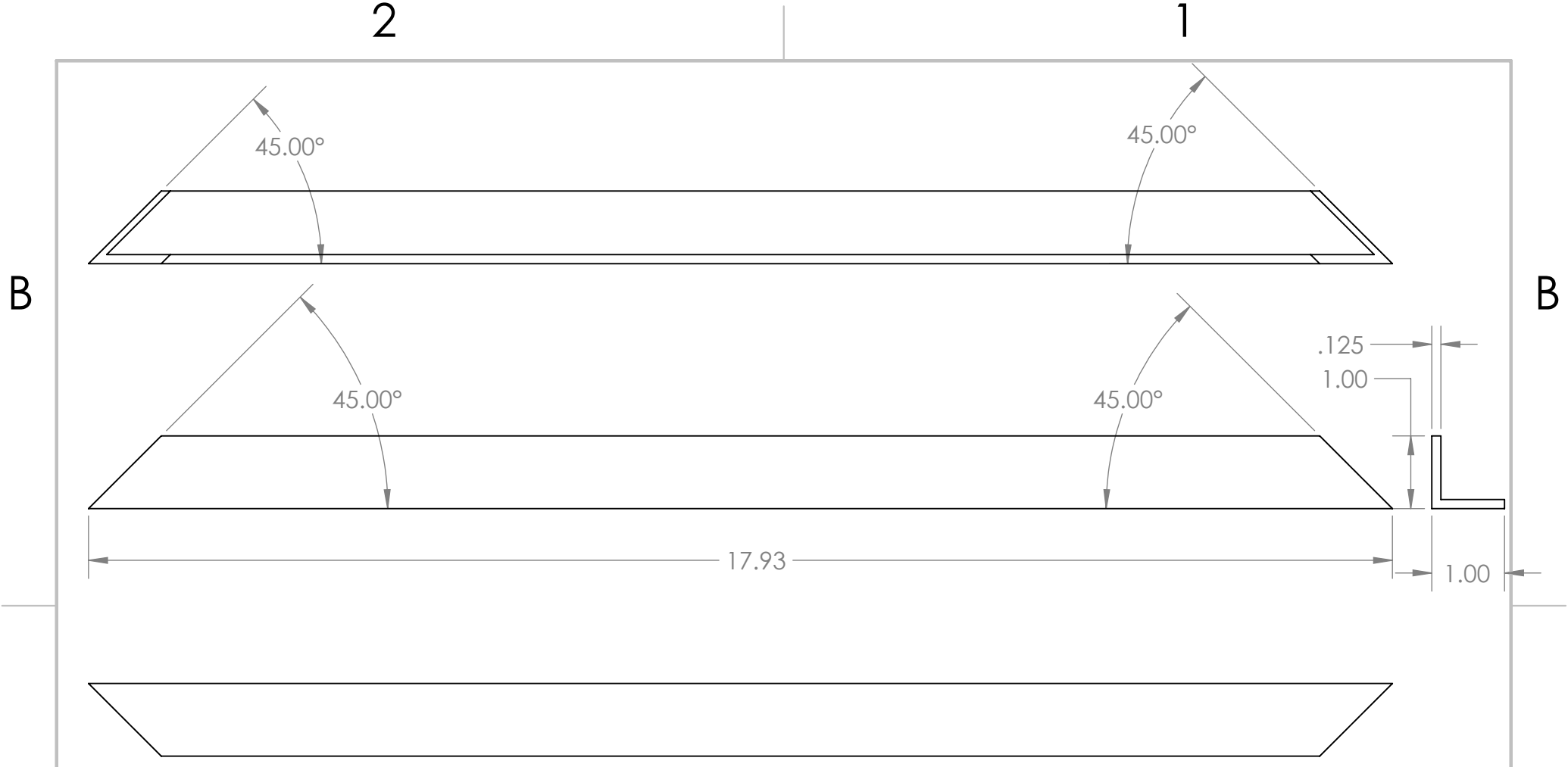
1:2

WEIGHT:

SHEET 1 OF 1

2

1



A

A

**PROPRIETARY AND CONFIDENTIAL**  
 THE INFORMATION CONTAINED IN THIS DRAWING IS THE SOLE PROPERTY OF <INSERT COMPANY NAME HERE>. ANY REPRODUCTION IN PART OR AS A WHOLE WITHOUT THE WRITTEN PERMISSION OF <INSERT COMPANY NAME HERE> IS PROHIBITED.

		UNLESS OTHERWISE SPECIFIED:		NAME	DATE
		DIMENSIONS ARE IN INCHES	DRAWN	CD	
		TOLERANCES:	CHECKED		
		FRACTIONAL ±	ENG APPR.		
		ANGULAR: MACH ± BEND ±	MFG APPR.		
		TWO PLACE DECIMAL ±	Q.A.		
		THREE PLACE DECIMAL ±	COMMENTS:		
		INTERPRET GEOMETRIC TOLERANCING PER:			
		MATERIAL			
		AISI 1020 steel			
		FINISH			
		as extruded			
NEXT ASSY	USED ON	APPLICATION			
		DO NOT SCALE DRAWING			

TITLE:  
**block support B**

SIZE	DWG. NO.	REV
<b>A</b>	<b>2</b>	
SCALE: 1:2	WEIGHT:	SHEET 1 OF 1

2

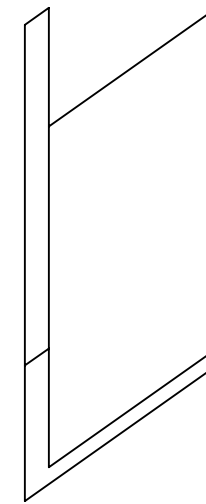
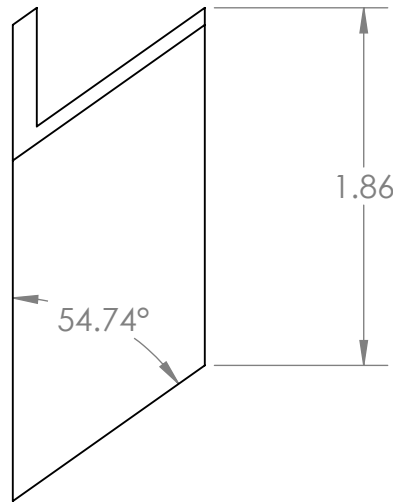
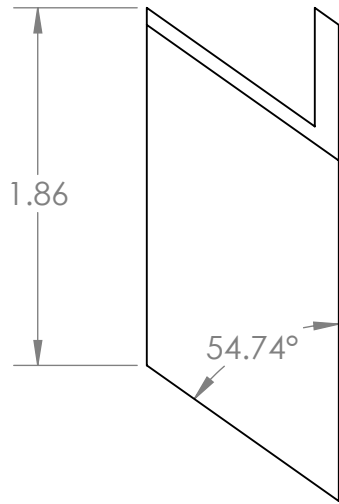
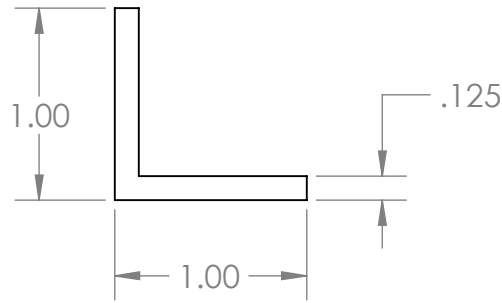
1

2

1

B

B



A

A

**PROPRIETARY AND CONFIDENTIAL**  
 THE INFORMATION CONTAINED IN THIS DRAWING IS THE SOLE PROPERTY OF <INSERT COMPANY NAME HERE>. ANY REPRODUCTION IN PART OR AS A WHOLE WITHOUT THE WRITTEN PERMISSION OF <INSERT COMPANY NAME HERE> IS PROHIBITED.

		UNLESS OTHERWISE SPECIFIED:		NAME	DATE
		DIMENSIONS ARE IN INCHES	DRAWN	C.D.	
		TOLERANCES:	CHECKED		
		FRACTIONAL ±	ENG APPR.		
		ANGULAR: MACH ± BEND ±	MFG APPR.		
		TWO PLACE DECIMAL ±	Q.A.		
		THREE PLACE DECIMAL ±	COMMENTS:		
		INTERPRET GEOMETRIC TOLERANCING PER:			
		MATERIAL			
		AISI 1020 steel			
		FINISH			
		as extruded			
NEXT ASSY	USED ON				
APPLICATION		DO NOT SCALE DRAWING			

TITLE:  
**block support C**

SIZE	DWG. NO.	REV
<b>A</b>	<b>3</b>	
SCALE: 1:1	WEIGHT:	SHEET 1 OF 1

2

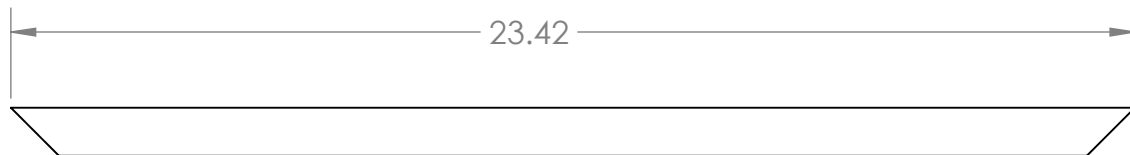
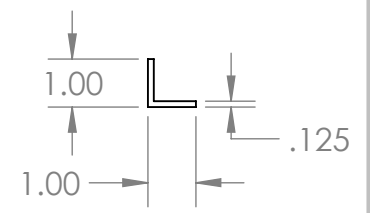
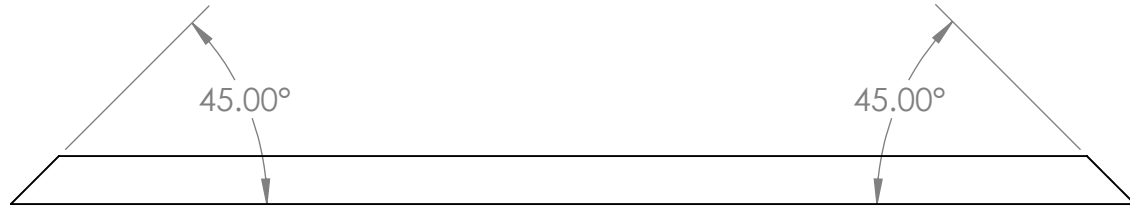
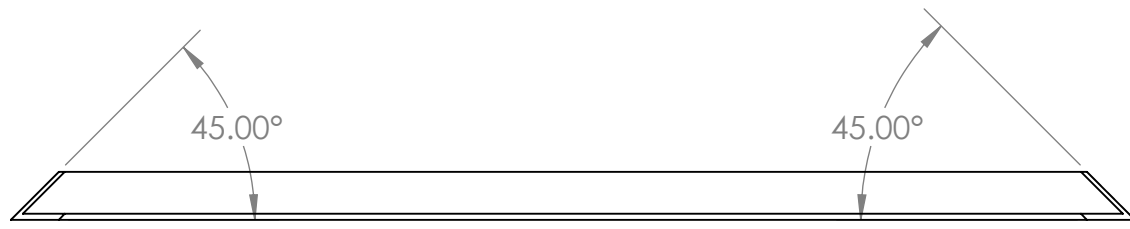
1

2

1

B

B



A

A

**PROPRIETARY AND CONFIDENTIAL**  
 THE INFORMATION CONTAINED IN THIS DRAWING IS THE SOLE PROPERTY OF <INSERT COMPANY NAME HERE>. ANY REPRODUCTION IN PART OR AS A WHOLE WITHOUT THE WRITTEN PERMISSION OF <INSERT COMPANY NAME HERE> IS PROHIBITED.

		UNLESS OTHERWISE SPECIFIED:		NAME	DATE
		DIMENSIONS ARE IN INCHES	DRAWN	C.D.	
		TOLERANCES:	CHECKED		
		FRACTIONAL ±	ENG APPR.		
		ANGULAR: MACH ± BEND ±	MFG APPR.		
		TWO PLACE DECIMAL ±	Q.A.		
		THREE PLACE DECIMAL ±	COMMENTS:		
		INTERPRET GEOMETRIC TOLERANCING PER:			
		MATERIAL			
		AISI 1020 steel			
		FINISH			
		as extruded			
NEXT ASSY	USED ON	DO NOT SCALE DRAWING			
	APPLICATION				

TITLE:  
**long edge bar**

SIZE	DWG. NO.	REV
<b>A</b>	<b>4</b>	
SCALE: 1:4	WEIGHT:	SHEET 1 OF 1

2

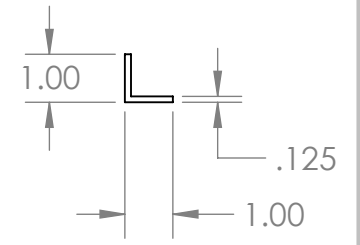
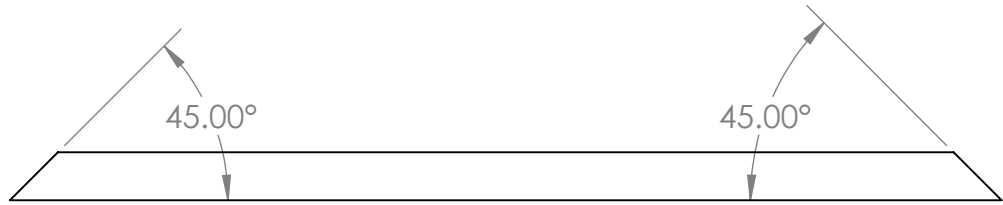
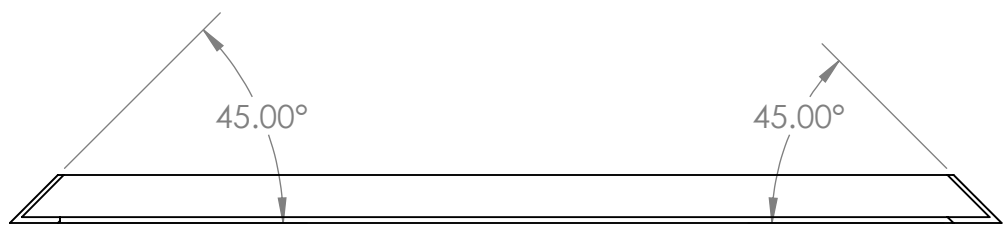
1

2

1

B

B



A

A

**PROPRIETARY AND CONFIDENTIAL**  
 THE INFORMATION CONTAINED IN THIS DRAWING IS THE SOLE PROPERTY OF <INSERT COMPANY NAME HERE>. ANY REPRODUCTION IN PART OR AS A WHOLE WITHOUT THE WRITTEN PERMISSION OF <INSERT COMPANY NAME HERE> IS PROHIBITED.

		UNLESS OTHERWISE SPECIFIED:		NAME	DATE
		DIMENSIONS ARE IN INCHES	DRAWN	C.D.	
		TOLERANCES:	CHECKED		
		FRACTIONAL ±	ENG APPR.		
		ANGULAR: MACH ± BEND ±	MFG APPR.		
		TWO PLACE DECIMAL ±	Q.A.		
		THREE PLACE DECIMAL ±	COMMENTS:		
		INTERPRET GEOMETRIC TOLERANCING PER:			
		MATERIAL			
		AISI 1020 steel			
		FINISH			
		as extruded			
NEXT ASSY	USED ON	APPLICATION			
		DO NOT SCALE DRAWING			

TITLE:		
medium edge bar		
SIZE	DWG. NO.	REV
<b>A</b>	<b>5</b>	
SCALE: 1:4	WEIGHT:	SHEET 1 OF 1

2

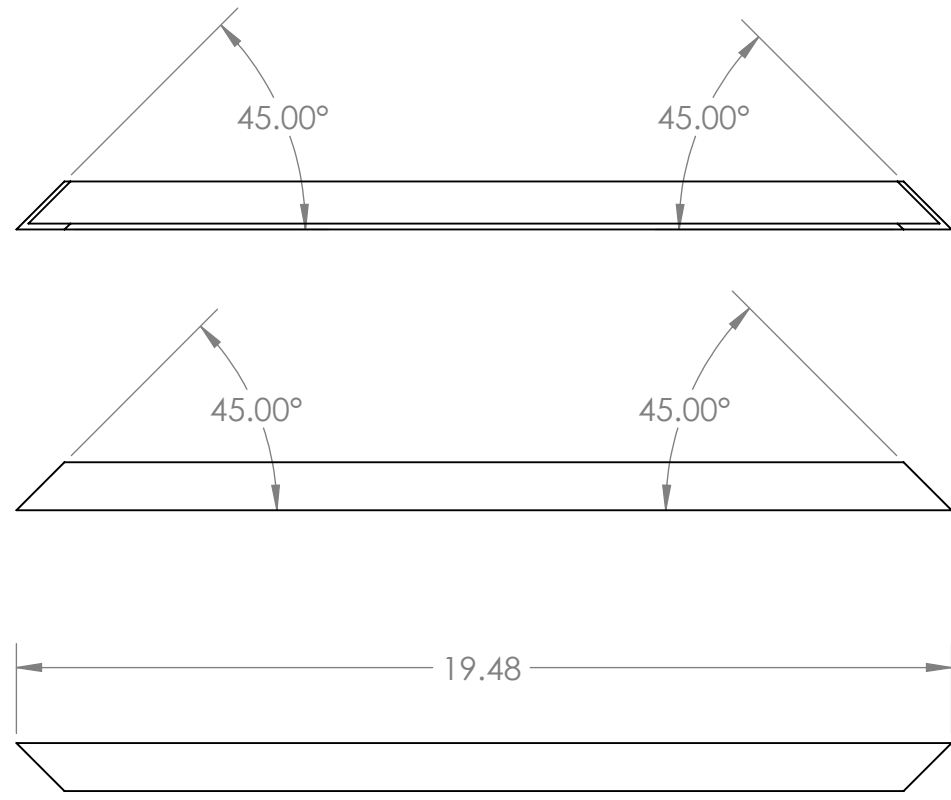
1

2

1

B

B



A

A

**PROPRIETARY AND CONFIDENTIAL**  
 THE INFORMATION CONTAINED IN THIS DRAWING IS THE SOLE PROPERTY OF <INSERT COMPANY NAME HERE>. ANY REPRODUCTION IN PART OR AS A WHOLE WITHOUT THE WRITTEN PERMISSION OF <INSERT COMPANY NAME HERE> IS PROHIBITED.

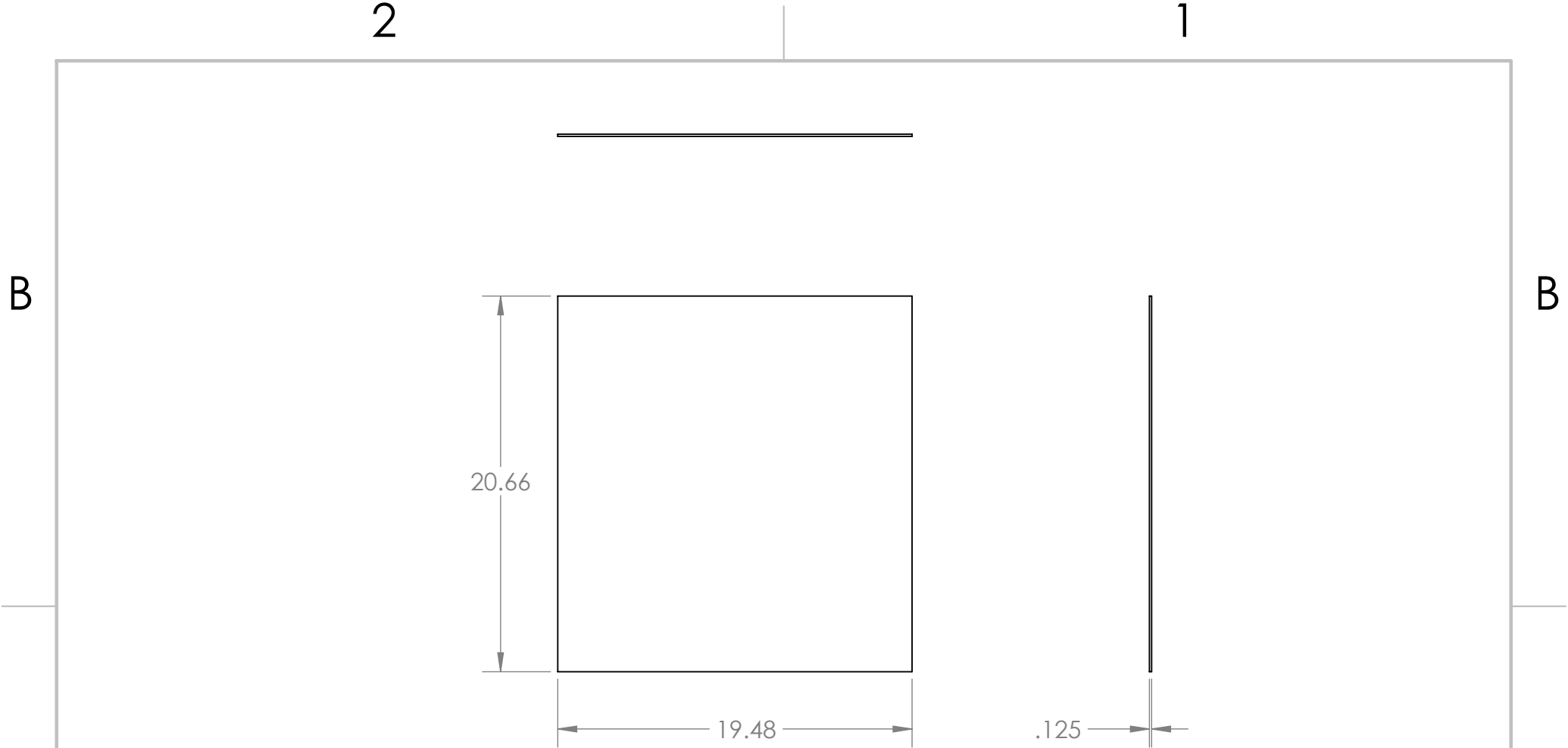
		UNLESS OTHERWISE SPECIFIED:		NAME	DATE
		DIMENSIONS ARE IN INCHES	DRAWN	C.D.	
		TOLERANCES:	CHECKED		
		FRACTIONAL ±	ENG APPR.		
		ANGULAR: MACH ± BEND ±	MFG APPR.		
		TWO PLACE DECIMAL ±	Q.A.		
		THREE PLACE DECIMAL ±	COMMENTS:		
		INTERPRET GEOMETRIC TOLERANCING PER:			
		MATERIAL			
		AISI 1020 steel			
		FINISH			
		as extruded			
NEXT ASSY	USED ON				
APPLICATION		DO NOT SCALE DRAWING			

TITLE:  
**short edge bar**

SIZE	DWG. NO.	REV
<b>A</b>	<b>6</b>	
SCALE: 1:4	WEIGHT:	SHEET 1 OF 1

2

1



**PROPRIETARY AND CONFIDENTIAL**  
 THE INFORMATION CONTAINED IN THIS DRAWING IS THE SOLE PROPERTY OF <INSERT COMPANY NAME HERE>. ANY REPRODUCTION IN PART OR AS A WHOLE WITHOUT THE WRITTEN PERMISSION OF <INSERT COMPANY NAME HERE> IS PROHIBITED.

		UNLESS OTHERWISE SPECIFIED:		NAME	DATE
		DIMENSIONS ARE IN INCHES	DRAWN	C.D.	
		TOLERANCES:	CHECKED		
		FRACTIONAL ±	ENG APPR.		
		ANGULAR: MACH ± BEND ±	MFG APPR.		
		TWO PLACE DECIMAL ±	Q.A.		
		THREE PLACE DECIMAL ±	COMMENTS:		
		INTERPRET GEOMETRIC TOLERANCING PER:			
		MATERIAL			
		AISI 1020 steel			
		FINISH			
		Aluminized			
NEXT ASSY	USED ON				
APPLICATION		DO NOT SCALE DRAWING			

TITLE:		
casing panel A		
SIZE	DWG. NO.	REV
<b>A</b>	<b>7</b>	
SCALE: 1:8	WEIGHT:	SHEET 1 OF 1

A

A

2

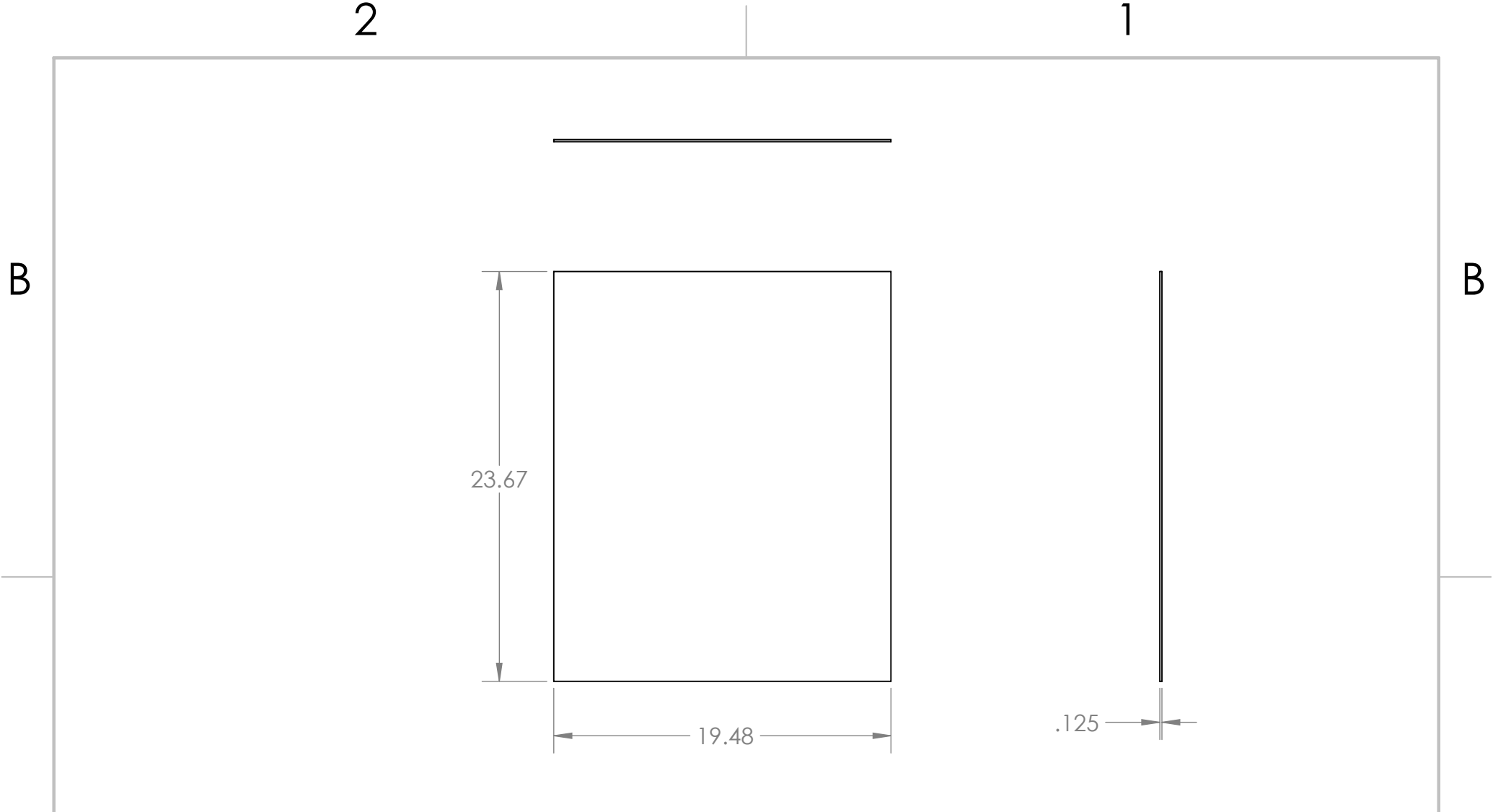
1

B

B

2

1



A

A

**PROPRIETARY AND CONFIDENTIAL**  
 THE INFORMATION CONTAINED IN THIS DRAWING IS THE SOLE PROPERTY OF <INSERT COMPANY NAME HERE>. ANY REPRODUCTION IN PART OR AS A WHOLE WITHOUT THE WRITTEN PERMISSION OF <INSERT COMPANY NAME HERE> IS PROHIBITED.

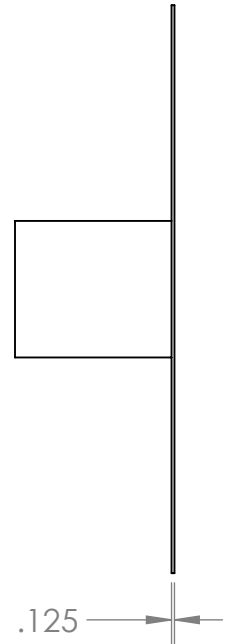
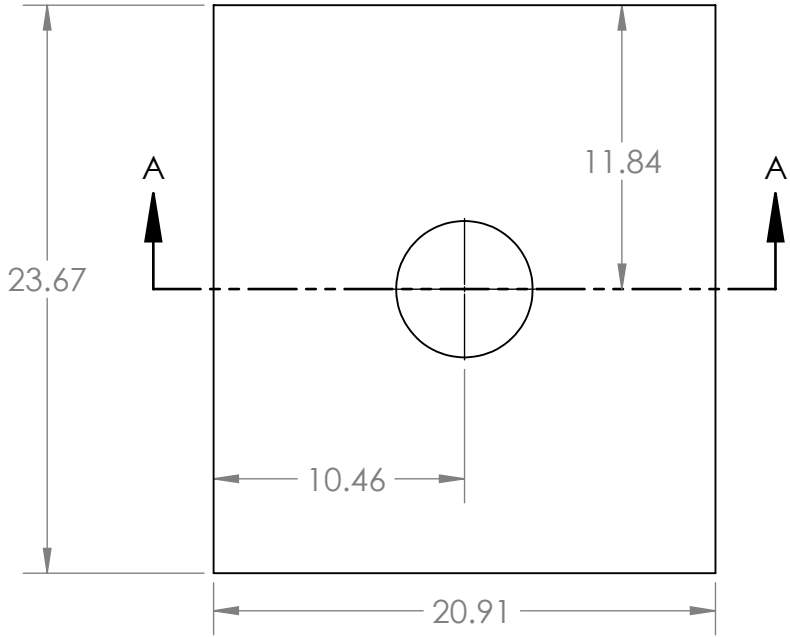
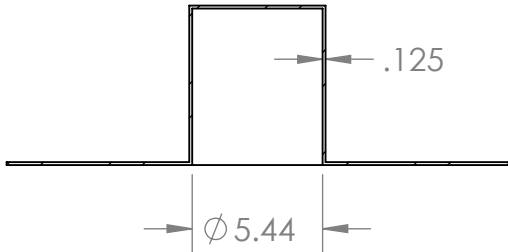
		UNLESS OTHERWISE SPECIFIED:		NAME	DATE
		DIMENSIONS ARE IN INCHES	DRAWN	C.D.	
		TOLERANCES:	CHECKED		
		FRACTIONAL ±	ENG APPR.		
		ANGULAR: MACH ± BEND ±	MFG APPR.		
		TWO PLACE DECIMAL ±	Q.A.		
		THREE PLACE DECIMAL ±	COMMENTS:		
		INTERPRET GEOMETRIC TOLERANCING PER:			
		MATERIAL			
		AISI 1020 steel			
		FINISH			
		Aluminized			
NEXT ASSY	USED ON				
	APPLICATION	DO NOT SCALE DRAWING			

TITLE:		
casing panel B		
SIZE	DWG. NO.	REV
<b>A</b>	<b>8</b>	
SCALE: 1:8	WEIGHT:	SHEET 1 OF 1

2

1

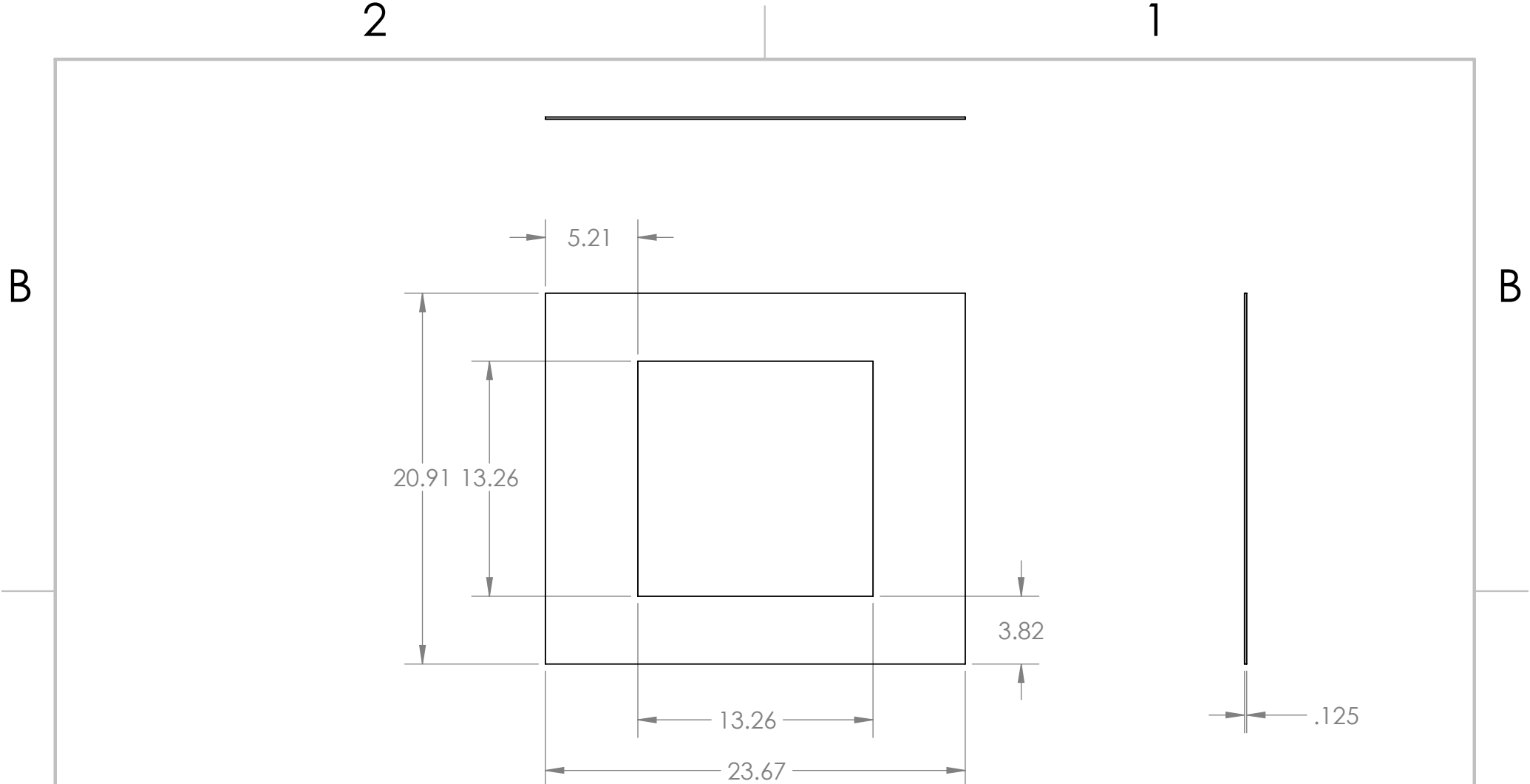
SECTION A-A  
SCALE 1 : 8



**PROPRIETARY AND CONFIDENTIAL**  
THE INFORMATION CONTAINED IN THIS DRAWING IS THE SOLE PROPERTY OF <INSERT COMPANY NAME HERE>. ANY REPRODUCTION IN PART OR AS A WHOLE WITHOUT THE WRITTEN PERMISSION OF <INSERT COMPANY NAME HERE> IS PROHIBITED.

		UNLESS OTHERWISE SPECIFIED:		NAME	DATE
		DIMENSIONS ARE IN INCHES	DRAWN	C.D.	
		TOLERANCES:	CHECKED		
		FRACTIONAL ±	ENG APPR.		
		ANGULAR: MACH ± BEND ±	MFG APPR.		
		TWO PLACE DECIMAL ±	Q.A.		
		THREE PLACE DECIMAL ±	COMMENTS:		
		INTERPRET GEOMETRIC TOLERANCING PER:			
		MATERIAL			
		AISI 1020 steel			
		FINISH			
		Aluminized			
NEXT ASSY	USED ON	DO NOT SCALE DRAWING			
APPLICATION					

TITLE:		
casing panel with cylider		
SIZE	DWG. NO.	REV
<b>A</b>	9	
SCALE: 1:8	WEIGHT:	SHEET 1 OF 1



**PROPRIETARY AND CONFIDENTIAL**  
 THE INFORMATION CONTAINED IN THIS DRAWING IS THE SOLE PROPERTY OF <INSERT COMPANY NAME HERE>. ANY REPRODUCTION IN PART OR AS A WHOLE WITHOUT THE WRITTEN PERMISSION OF <INSERT COMPANY NAME HERE> IS PROHIBITED.

		UNLESS OTHERWISE SPECIFIED:		NAME	DATE
		DIMENSIONS ARE IN INCHES	DRAWN	C.D.	
		TOLERANCES:	CHECKED		
		FRACTIONAL ±	ENG APPR.		
		ANGULAR: MACH ± BEND ±	MFG APPR.		
		TWO PLACE DECIMAL ±	Q.A.		
		THREE PLACE DECIMAL ±	COMMENTS:		
		INTERPRET GEOMETRIC TOLERANCING PER:			
		MATERIAL			
		AISI 1020 steel			
		FINISH			
		Aluminized			
NEXT ASSY	USED ON				
	APPLICATION	DO NOT SCALE DRAWING			

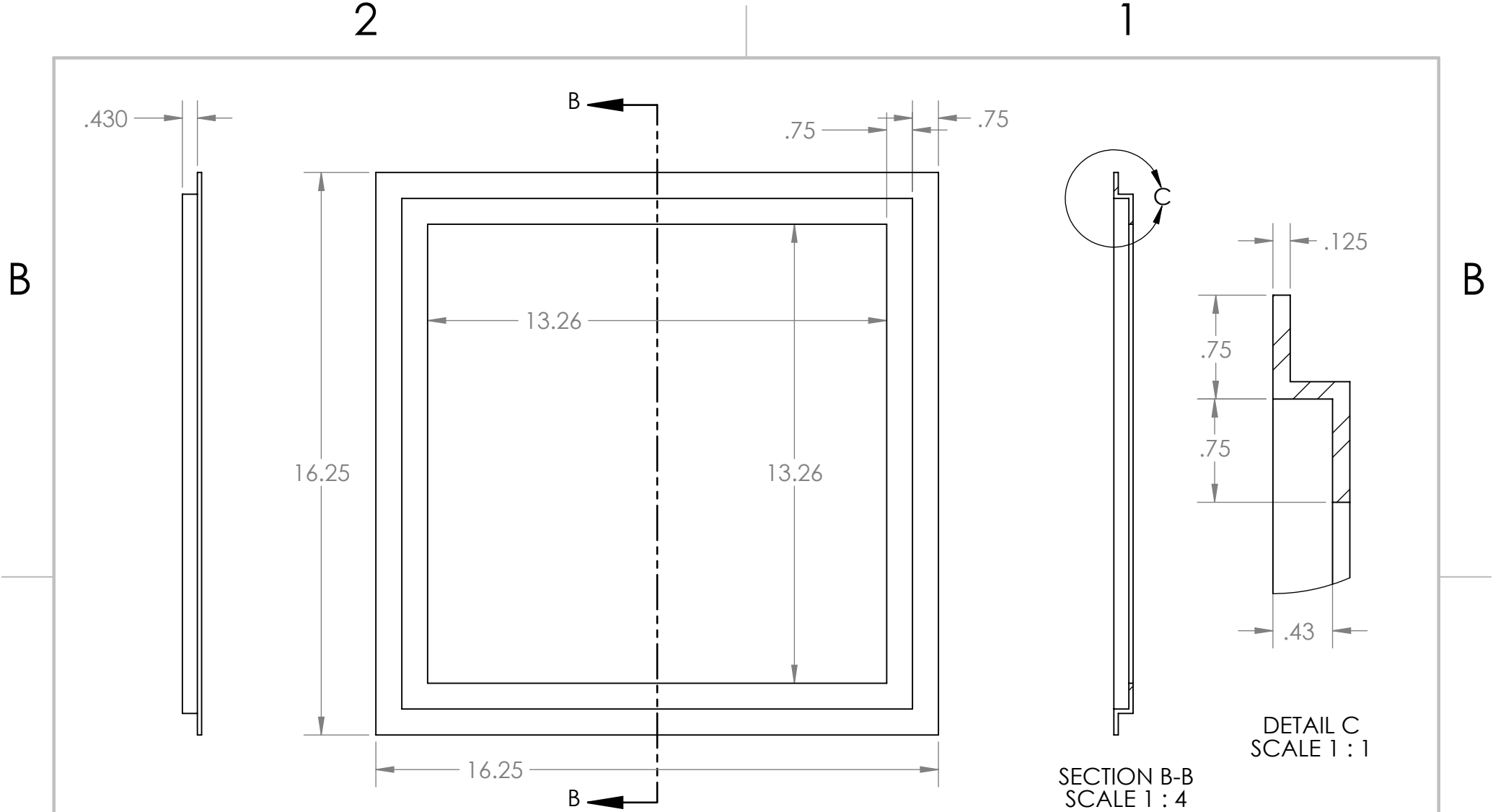
TITLE:		
box panel with glass		
SIZE	DWG. NO.	REV
<b>A</b>	10	
SCALE: 1:8	WEIGHT:	SHEET 1 OF 1

A

A

2

1



A

A

**PROPRIETARY AND CONFIDENTIAL**  
 THE INFORMATION CONTAINED IN THIS DRAWING IS THE SOLE PROPERTY OF <INSERT COMPANY NAME HERE>. ANY REPRODUCTION IN PART OR AS A WHOLE WITHOUT THE WRITTEN PERMISSION OF <INSERT COMPANY NAME HERE> IS PROHIBITED.

		UNLESS OTHERWISE SPECIFIED:		NAME	DATE
		DIMENSIONS ARE IN INCHES	DRAWN	C.D.	
		TOLERANCES:	CHECKED		
		FRACTIONAL ±	ENG APPR.		
		ANGULAR: MACH ± BEND ±	MFG APPR.		
		TWO PLACE DECIMAL ±	Q.A.		
		THREE PLACE DECIMAL ±	COMMENTS:		
		INTERPRET GEOMETRIC TOLERANCING PER:			
		MATERIAL			
		AISI 1020 steel			
		FINISH			
NEXT ASSY	USED ON				
	APPLICATION	DO NOT SCALE DRAWING			

SECTION B-B  
SCALE 1 : 4

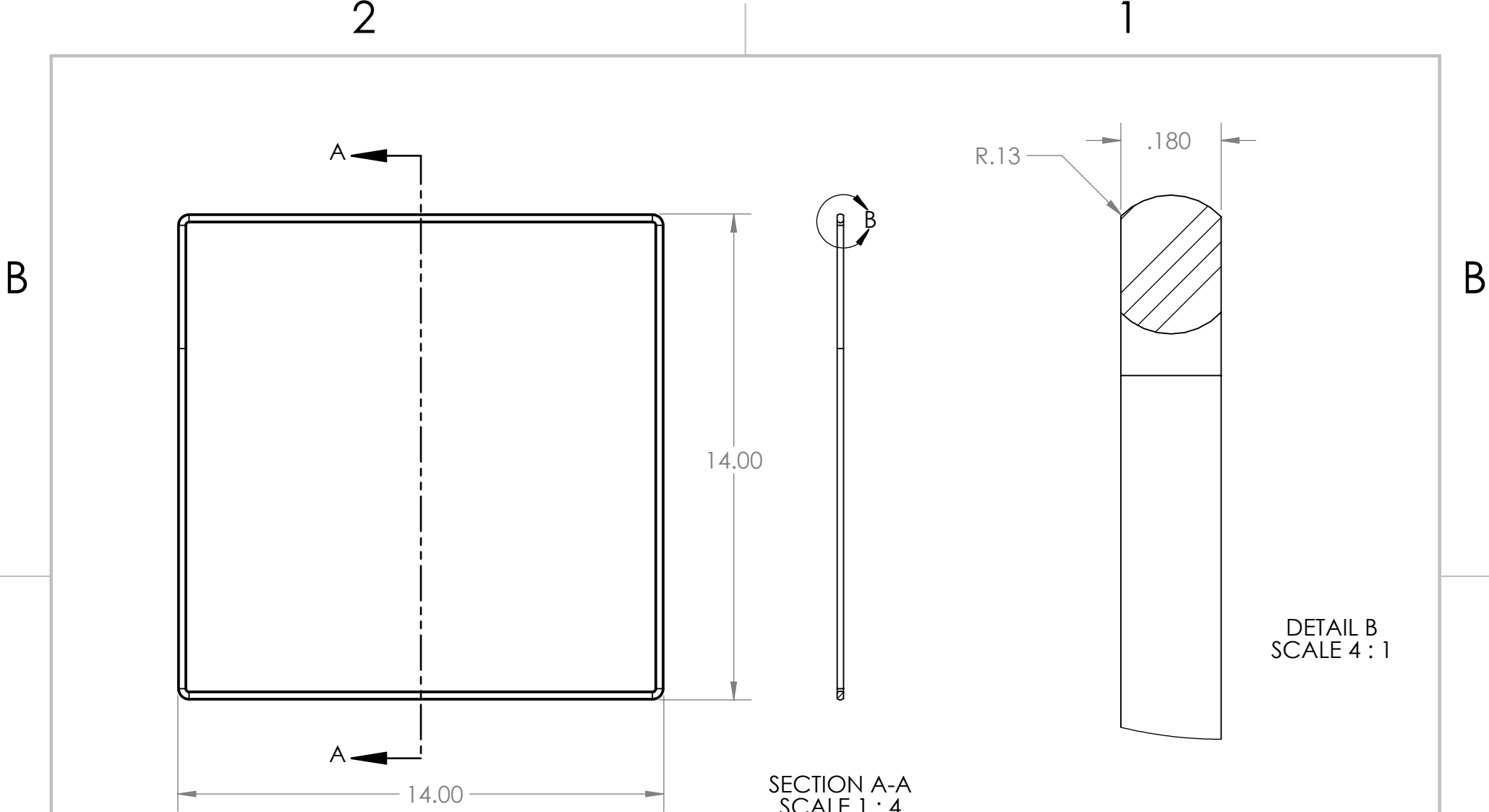
DETAIL C  
SCALE 1 : 1

TITLE:  
**window bracket**

SIZE	DWG. NO.	REV
<b>A</b>	<b>11</b>	
SCALE: 1:4	WEIGHT:	SHEET 1 OF 1

2

1



**PROPRIETARY AND CONFIDENTIAL**  
 THE INFORMATION CONTAINED IN THIS DRAWING IS THE SOLE PROPERTY OF <INSERT COMPANY NAME HERE>. ANY REPRODUCTION IN PART OR AS A WHOLE WITHOUT THE WRITTEN PERMISSION OF <INSERT COMPANY NAME HERE> IS PROHIBITED.

		UNLESS OTHERWISE SPECIFIED:		NAME	DATE
		DIMENSIONS ARE IN INCHES	DRAWN	C.D.	
		TOLERANCES:	CHECKED		
		FRACTIONAL ±	ENG APPR.		
		ANGULAR: MACH ± BEND ±	MFG APPR.		
		TWO PLACE DECIMAL ±	Q.A.		
		THREE PLACE DECIMAL ±	COMMENTS:		
		INTERPRET GEOMETRIC TOLERANCING PER:	Dimensions shown are for o-ring compressed under window bracket		
		MATERIAL	silicone	SIZE	DWG. NO.
		FINISH		<b>A</b>	12
NEXT ASSY	USED ON	DO NOT SCALE DRAWING		SCALE: 1:4	WEIGHT:
					SHEET 1 OF 1

TITLE:		
o-ring		
SIZE	DWG. NO.	REV
<b>A</b>	12	
SCALE: 1:4	WEIGHT:	SHEET 1 OF 1

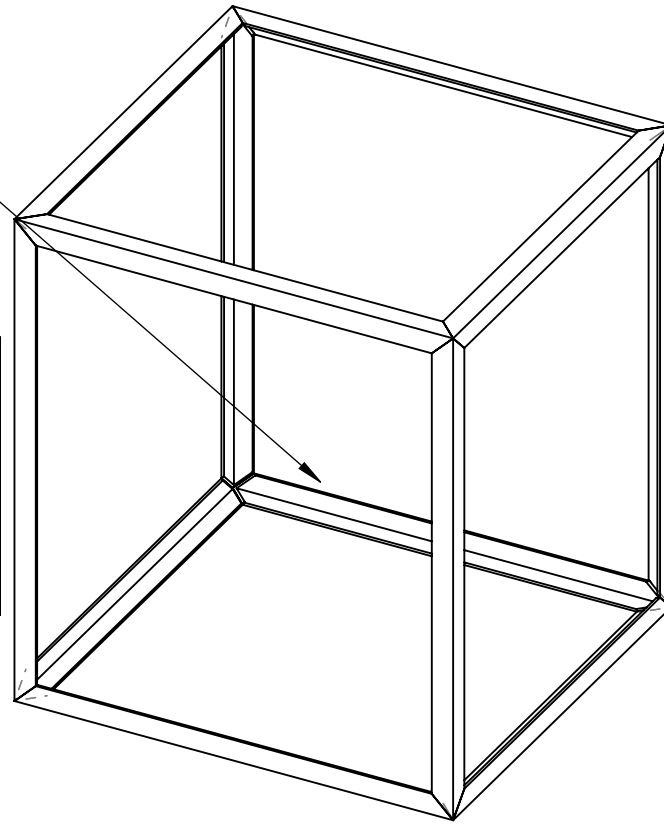
2

1

B

B

weld all 8 corners



ITEM NO.	PART NUMBER	DESCRIPTION	QTY.
1	4	long edge bar	4
2	5	medium edge bar	4
3	6	short edge bar	4

A

A

		UNLESS OTHERWISE SPECIFIED:		NAME	DATE	TITLE: <b>casing frame</b>		
		DIMENSIONS ARE IN INCHES	DRAWN	C.D.				
		TOLERANCES:	CHECKED					
		FRACTIONAL ±	ENG APPR.					
		ANGULAR: MACH ± BEND ±	MFG APPR.					
		TWO PLACE DECIMAL ±	Q.A.			SIZE	DWG. NO.	REV
		THREE PLACE DECIMAL ±	COMMENTS:			<b>A</b>	<b>13</b>	
		INTERPRET GEOMETRIC TOLERANCING PER:				SCALE: 1:8	WEIGHT:	SHEET 1 OF 1
		MATERIAL						
		FINISH						
	NEXT ASSY	USED ON						
	APPLICATION		DO NOT SCALE DRAWING					

**PROPRIETARY AND CONFIDENTIAL**  
 THE INFORMATION CONTAINED IN THIS DRAWING IS THE SOLE PROPERTY OF <INSERT COMPANY NAME HERE>. ANY REPRODUCTION IN PART OR AS A WHOLE WITHOUT THE WRITTEN PERMISSION OF <INSERT COMPANY NAME HERE> IS PROHIBITED.

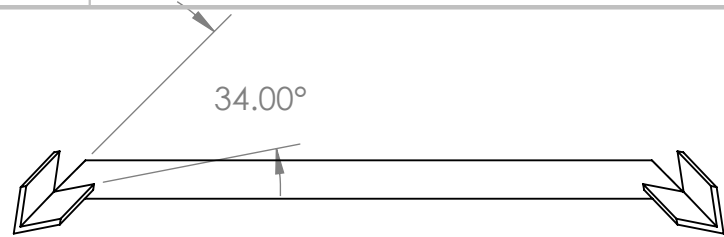
2

1

2

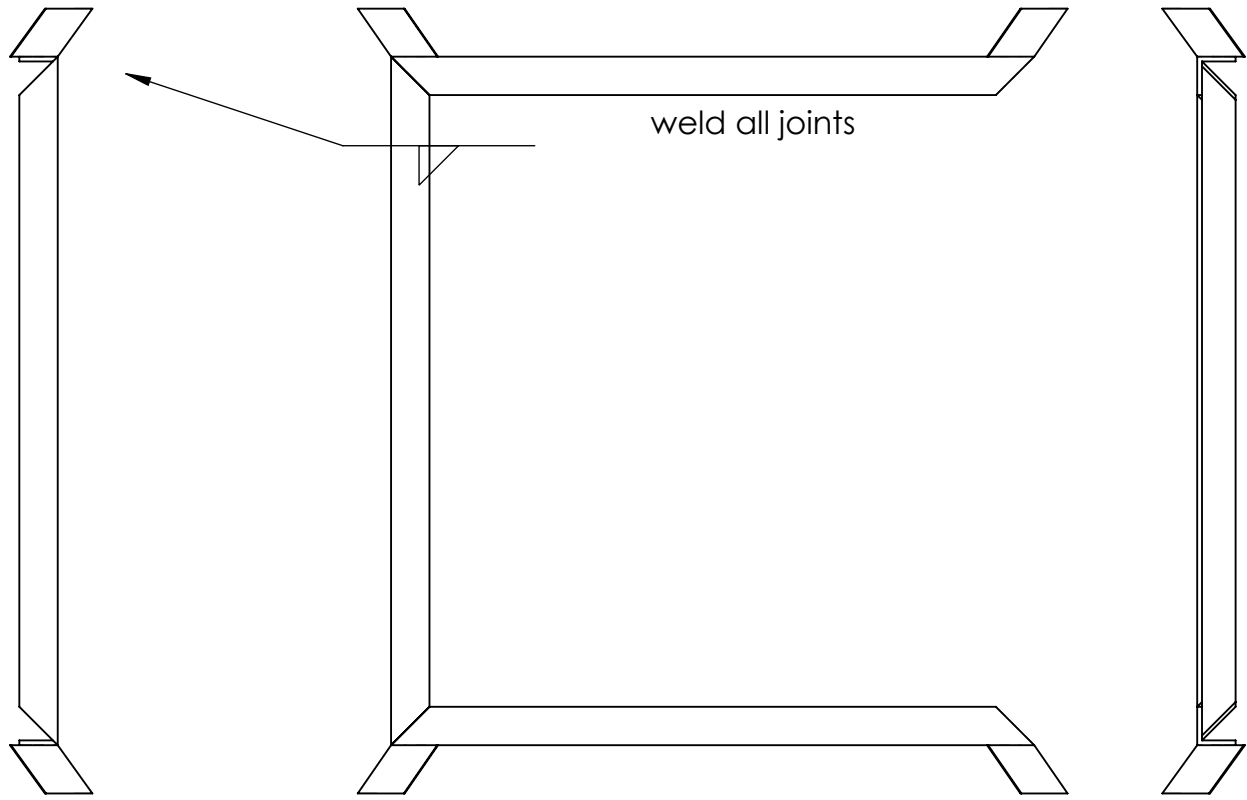
1

ITEM NO.	PART NUMBER	DESCRIPTION	QTY.
1	1	block support A	2
2	2	block support B	1
3	3	block support C	4



B

B



A

A

**PROPRIETARY AND CONFIDENTIAL**  
 THE INFORMATION CONTAINED IN THIS DRAWING IS THE SOLE PROPERTY OF <INSERT COMPANY NAME HERE>. ANY REPRODUCTION IN PART OR AS A WHOLE WITHOUT THE WRITTEN PERMISSION OF <INSERT COMPANY NAME HERE> IS PROHIBITED.

		UNLESS OTHERWISE SPECIFIED:		NAME	DATE
		DIMENSIONS ARE IN INCHES	DRAWN		
		TOLERANCES:	CHECKED		
		FRACTIONAL ±	ENG APPR.		
		ANGULAR: MACH ± BEND ±	MFG APPR.		
		TWO PLACE DECIMAL ±	Q.A.		
		THREE PLACE DECIMAL ±	COMMENTS:		
		INTERPRET GEOMETRIC TOLERANCING PER:			
		MATERIAL			
		FINISH			
NEXT ASSY	USED ON				
APPLICATION		DO NOT SCALE DRAWING			

TITLE:		
<b>block support assembly</b>		
SIZE	DWG. NO.	REV
<b>A</b>	<b>14</b>	
SCALE: 1:5	WEIGHT:	SHEET 1 OF 1

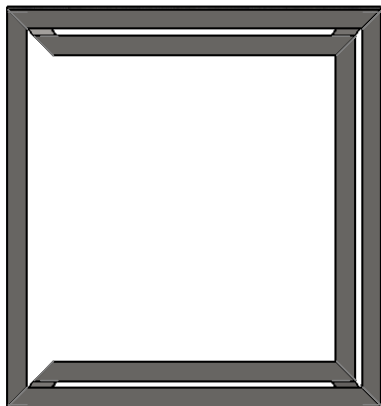
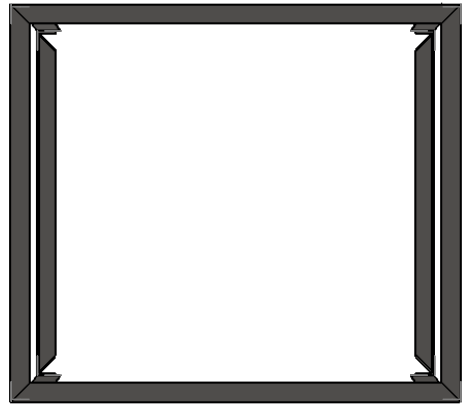
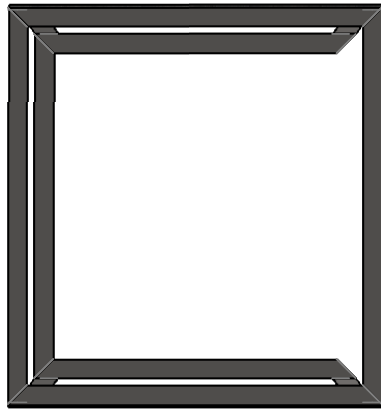
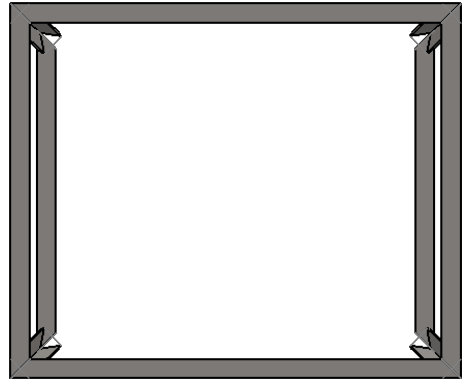
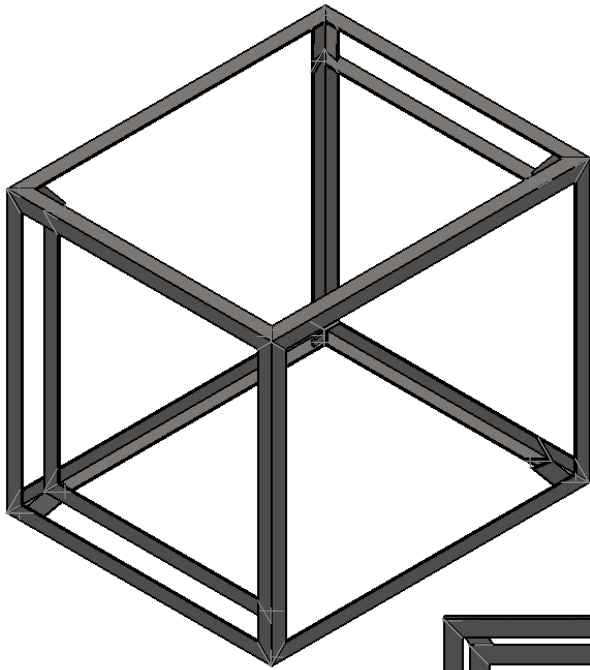
2

1

2

1

PART NUMBER	DESCRIPTION	QTY.
14	block support assembly	2
13	casing frame	1



B

B

A

A

**PROPRIETARY AND CONFIDENTIAL**  
 THE INFORMATION CONTAINED IN THIS DRAWING IS THE SOLE PROPERTY OF <INSERT COMPANY NAME HERE>. ANY REPRODUCTION IN PART OR AS A WHOLE WITHOUT THE WRITTEN PERMISSION OF <INSERT COMPANY NAME HERE> IS PROHIBITED.

		UNLESS OTHERWISE SPECIFIED:		NAME	DATE
		DIMENSIONS ARE IN INCHES	DRAWN	C.D.	
		TOLERANCES:	CHECKED		
		FRACTIONAL ±	ENG APPR.		
		ANGULAR: MACH ± BEND ±	MFG APPR.		
		TWO PLACE DECIMAL ±	Q.A.		
		THREE PLACE DECIMAL ±	COMMENTS:		
		INTERPRET GEOMETRIC TOLERANCING PER:	weld block supports to casing frame		
		MATERIAL			
NEXT ASSY	USED ON	FINISH	SIZE	DWG. NO.	REV
			<b>A</b>	<b>15</b>	
APPLICATION		DO NOT SCALE DRAWING	SCALE: 1:10 WEIGHT:		SHEET 1 OF 1

TITLE: **full frame**

2

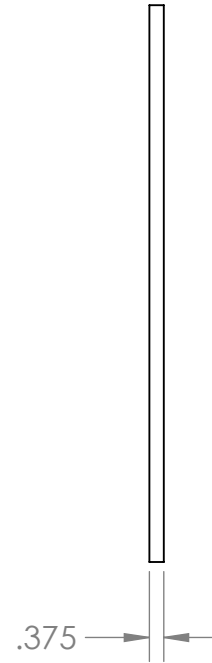
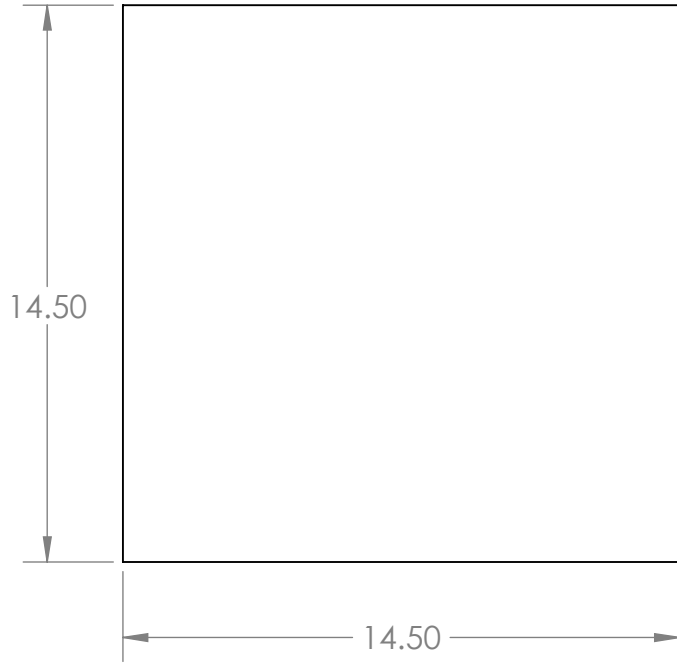
1

2

1

B

B



A

A

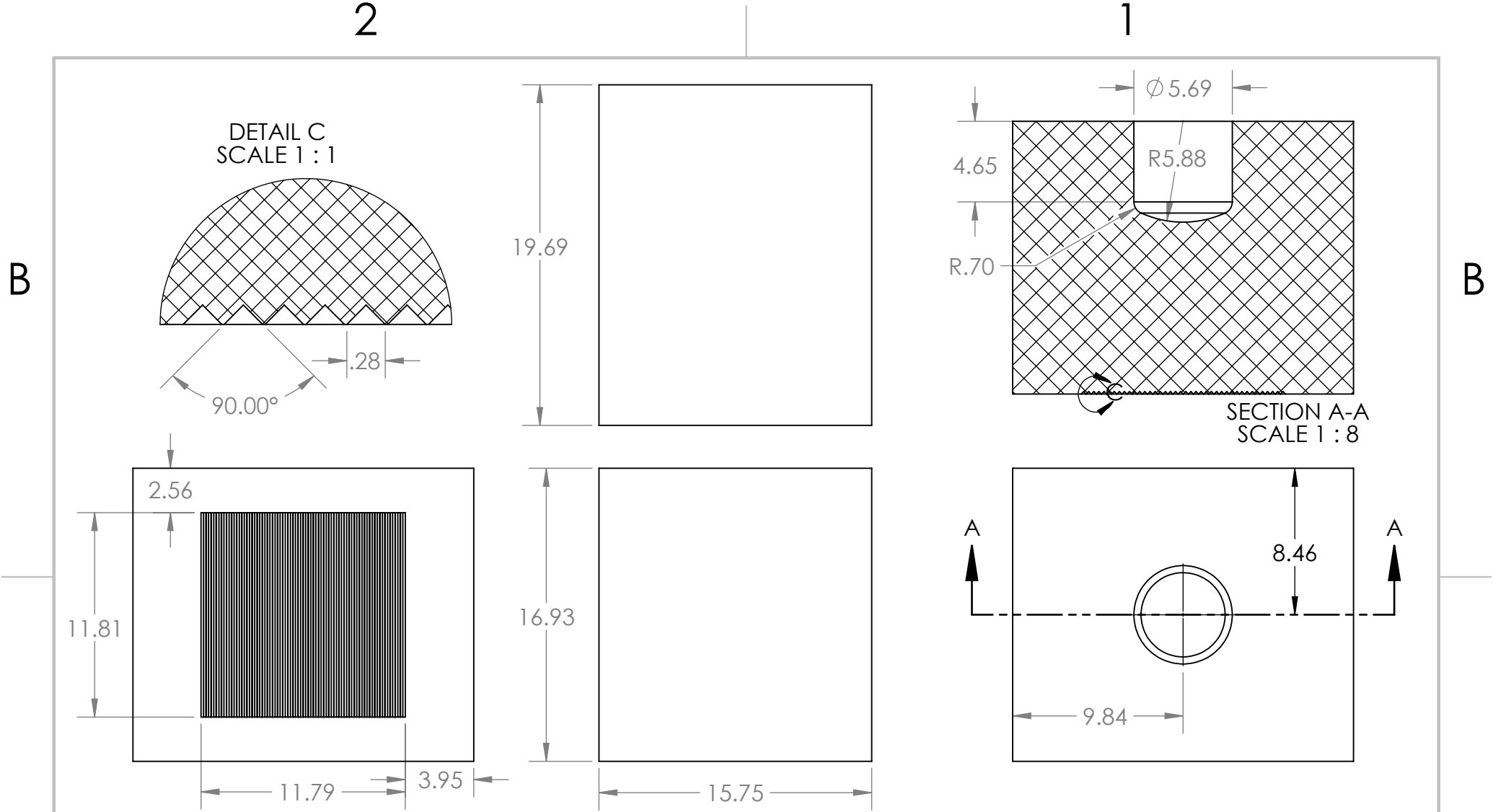
**PROPRIETARY AND CONFIDENTIAL**  
 THE INFORMATION CONTAINED IN THIS DRAWING IS THE SOLE PROPERTY OF <INSERT COMPANY NAME HERE>. ANY REPRODUCTION IN PART OR AS A WHOLE WITHOUT THE WRITTEN PERMISSION OF <INSERT COMPANY NAME HERE> IS PROHIBITED.

		UNLESS OTHERWISE SPECIFIED:		NAME	DATE
		DIMENSIONS ARE IN INCHES	DRAWN	C.D.	
		TOLERANCES:	CHECKED		
		FRACTIONAL ±	ENG APPR.		
		ANGULAR: MACH ± BEND ±	MFG APPR.		
		TWO PLACE DECIMAL ±	Q.A.		
		THREE PLACE DECIMAL ±	COMMENTS:		
		INTERPRET GEOMETRIC TOLERANCING PER:			
		MATERIAL	Silicon sheet		
NEXT ASSY	USED ON	FINISH			
APPLICATION		DO NOT SCALE DRAWING			

TITLE:		
window		
SIZE	DWG. NO.	REV
<b>A</b>	16	
SCALE: 1:4	WEIGHT:	SHEET 1 OF 1

2

1



A

A

**PROPRIETARY AND CONFIDENTIAL**  
 THE INFORMATION CONTAINED IN THIS DRAWING IS THE SOLE PROPERTY OF <INSERT COMPANY NAME HERE>. ANY REPRODUCTION IN PART OR AS A WHOLE WITHOUT THE WRITTEN PERMISSION OF <INSERT COMPANY NAME HERE> IS PROHIBITED.

		UNLESS OTHERWISE SPECIFIED:	NAME	DATE
		DIMENSIONS ARE IN INCHES	DRAWN	C.D.
		TOLERANCES:	CHECKED	
		FRACTIONAL $\pm$	ENG APPR.	
		ANGULAR: MACH $\pm$ BEND $\pm$	MFG APPR.	
		TWO PLACE DECIMAL $\pm$	Q.A.	
		THREE PLACE DECIMAL $\pm$	COMMENTS:	
		INTERPRET GEOMETRIC TOLERANCING PER:		
		MATERIAL		
		high grade graphite		
		FINISH		
NEXT ASSY	USED ON			
APPLICATION		DO NOT SCALE DRAWING		

TITLE:  
**graphite block**

SIZE **A** DWG. NO. **17** REV

SCALE: 1:8 WEIGHT: SHEET 1 OF 1

2

1